

TABLE OF CONTENTS

ABSTRACT.....	iii
RÉSUMÉ.....	v
ACKNOWLEDGEMENTS.....	vii
TABLE OF CONTENTS.....	ix
LIST OF FIGURES.....	xii
LIST OF ACRONYMS.....	xiv
LIST OF SYMBOLS.....	xv
INTRODUCTION.....	1
In-cloud icing.....	3
Cloud physics and ice accretion.....	3
Topography and icing events.....	3
Challenges and motivations.....	5
Hazard assessment of icing events.....	5
Mesoscale Modeling of Atmospheric icing.....	6
Objective.....	8
Structure of the thesis.....	9
References.....	11
CHAPTER 1.....	15
1. ATMOSPHERIC ICING SEVERITY: QUANTIFICATION AND MAPPING.....	16
Abstract.....	16
1.1 Introduction.....	17
1.2 Methodology.....	22
1.2.1 Reanalysis Data.....	24
1.2.2 Icing calculations.....	25
1.2.3 Icing events.....	28
1.2.4 Freezing rain storm of 1998.....	28
1.2.5 Icing severity index.....	31
1.3 Results.....	33
1.3.1 Case studies.....	34
1.3.2 Ice storm of January 1998.....	44
1.3.3 Icing severity index.....	48
1.4 Discussion of the results.....	55
1.5 Conclusion.....	58
1.6 References.....	60
CHAPTER 2.....	65
2. HYBRID FINE SCALE CLIMATOLOGY AND MICROPHYSICS OF IN-CLOUD ICING: FROM 32KM REANALYSIS TO 5KM MESOSCALE MODELING.....	66

Abstract.....	66
2.1 Introduction.....	67
2.2 Method.....	70
2.3 Results.....	73
2.3.1 Climatology of atmospheric icing.....	73
2.3.2 Transition from 32-year to 15-year.....	75
2.3.3 GEM-LAM and NARR performances.....	78
2.3.4 Selection of significant days.....	81
2.3.5 Mesoscale modeling and simulation setup.....	83
2.3.6 Statistics and cloud microphysics properties.....	87
2.3.7 Vertical profile of icing events climatology.....	89
2.3.8 Icing severity index at fine scale resolution.....	93
2.4 Conclusion.....	100
2.5 References.....	102
CHAPTER 3.....	106
3. ATMOSPHERIC ICING IMPACT ON WIND TURBINE PRODUCTION.....	107
Abstract.....	107
3.1 Introduction.....	108
3.2 Methodology.....	112
3.2.1 Generic wind turbine.....	113
3.2.2 Blade.....	113
3.2.3 Chord.....	113
3.2.4 Airfoil.....	114
3.2.5 Speed.....	115
3.3 Ice accretion model.....	116
3.4 Power distribution model.....	117
3.5 Results.....	119
3.5.1 Power along the blade.....	119
3.5.2 Water collection efficiency.....	120
3.5.3 Ice mass rate.....	121
3.5.4 Aerodynamic effect.....	122
3.5.5 Freezing fraction.....	125
3.5.6 Power loss.....	128
3.6 Analysis.....	138
3.7 Conclusion.....	142
3.8 References.....	144
GENERAL CONCLUSION.....	147

LIST OF TABLES

TABLE 1.1 : SEVERITY CLASSES	32
TABLE 1.2 : MONTHLY KEY VARIABLE IN THE TWO SITES.....	35
TABLE 2.1 : SELECTED SIGNIFICANT DAYS FOR GEM-LAM	82
TABLE 2.2 : GRID SETUP FOR THE NUMERICAL EXPERIMENT	84
TABLE 2.3 : THE LOWEST 17 VERTICAL LEVELS USED IN GEM-LAM THAT CORRESPOND TO ABL.....	84
TABLE 3.1 : DURATION OF ICING EVENTS FROM REANALYSIS: 32-YEAR ICING CLIMATE.....	135

LIST OF FIGURES

FIGURE 1.1. A HYDRO-QUEBEC ICING-RATE METER (AMIL-UQAC).	24
FIGURE 1.2. LIQUID WATER CONTENT CALCULATED USING PRECIPITATION RATE FROM REANALYSIS THAT COVERS THE PERIOD JANUARY 04TH UNTIL JANUARY 10TH.	30
FIGURE 1.3. MEDIAN VOLUME DIAMETER CALCULATED USING PRECIPITATION RATE FROM REANALYSIS THAT COVERS THE PERIOD JANUARY 04TH UNTIL JANUARY 10TH.	30
FIGURE 1.4. CROSS-SECTION OF NARR TOPOGRAPHY.	34
FIGURE 1.5. MONTHLY MODEL-BASED CALCULATION AND MEASUREMENTS ON BAGOTVILLE;	37
FIGURE 1.6. MONTHLY MODEL-BASED CALCULATION AND MEASUREMENTS ON MT BÉLAIR; (A) DURATION OF ICING EVENTS (B) ACCUMULATION OF ICE.	39
FIGURE 1.7. CLIMATOLOGY OF MODEL-BASED IN-CLOUD ICING EVENTS, DURATION AND ACCUMULATION OVER BAGOTVILLE IN JANUARY FOR 32 YEARS.	40
FIGURE 1.8. MODEL-BASED MONTHLY DURATION OF ICING EVENTS IN JANUARY FOR 32 YEARS AT MOUNT BÉLAIR (QUEBEC, CANADA).	41
FIGURE 1.9. MONTHLY MODEL-BASED SEVERITY AND ICE ACCUMULATION ON BAGOTVILLE DURING JANUARY OF EACH YEAR - 32 YEARS.....	43
FIGURE 1.10. MONTHLY MODEL-BASED SEVERITY AND ICE ACCUMULATION ON MT BÉLAIR DURING JANUARY OF EACH YEAR - 32 YEARS.....	43
FIGURE 1.11. ICING ACCUMULATION FROM JANUARY 4 TO 10, 1998 OVER THE SOUTHWESTERN REGION OF QUEBEC (CANADA) (A) ICE ACCUMULATION CALCULATED USING NARR REANALYSIS	47
FIGURE 1.12 : ICING SEVERITY INDEX MAP - JANUARY 1979–2010.	49
FIGURE 1.13. ICING SEVERITY INDEX MAP - FEBRUARY 1979–2010.	50
FIGURE 1.14. ICING SEVERITY INDEX MAP - DECEMBER 1979–2010.	51
FIGURE 1.15. ICING SEVERITY INDEX MAP — 3 MONTH'S AVERAGE 1979–2010.....	54
FIGURE 2.1. HYBRID APPROACH USING NARR 32KM AND GEM-LAM 5KM COMBINATION.	71
FIGURE 2.2. MEAN VALUES OF THE ICE ACCUMULATION AND THE DURATION OF ICING EVENTS (JANUARY: 1980-2009)	74
FIGURE 2.3. COMPARISON BETWEEN THE ICING SEVERITY INDEX DURING 32 YEARS AND 15 YEARS OVER 17 X 20 NARR CELLS CENTRED AT RIVIERE-DU-LOUP	76
FIGURE 2.4. COMPARISON BETWEEN 32 YEARS AND 15 YEARS: DURATION OF ICING EVENTS (A,B), ICE ACCUMULATION (C,D) AND ICING SEVERITY INDEX (E,F). COLOUR SCALES ARE CLIPPED FOR THE 15 YEAR PERIOD.	77
FIGURE 2.5. TOPOGRAPHY CROSS SECTION VIEWED BY NARR 32KM, GEM-LAM 5KM AND GEM-LAM 1KM	79
FIGURE 2.6. COMPARISON OF TEMPERATURES FROM NARR 32 KM, GEM-LAM 5KM AND OBSERVATION.....	80
FIGURE 2.7. COMPARISON OF ISI OVER MOUNT-BELAIR (15 YEARS) WITH ALL DAYS VERSUS SELECTED DAYS.	82
FIGURE 2.8. SIMULATION DOMAINS AND TARGET ZONE.....	86
FIGURE 2.9. STATISTICS OF METEOROLOGICAL ICING PARAMETERS	88
FIGURE 2.10. VERTICAL PROFILES OF HIGH RESOLUTION 15-YEAR CLIMATOLOGY OF ICING EVENTS: (A) SEVERITY CLASSES (B) DURATION OF ICING EVENTS (C) ICE ACCUMULATION (D) TOPOGRAPHY FROM GEM-LAM5KM.....	91
FIGURE 2.11. 15-YEAR CLIMATOLOGY OF ICING SEVERITY INDEX AT 1000 MB: (A) NARR 32 KM, (B) GEM-LAM 5KM.....	94
FIGURE 2.12. 15-YEAR CLIMATOLOGY OF ICE ACCUMULATION AND DURATION OF ICING EVENTS AT 40M, 80M AND 120.....	96
FIGURE 2.13. VERTICAL PROFILES OF ICE ACCUMULATION AND DURATION OF ICING EVENTS BETWEEN 10 AND 200 M.....	98

FIGURE 2.14. 15-YEAR CLIMATOLOGY OF ICING SEVERITY INDEX AT 80 M.	99
FIGURE 3.1. CHORD VARIATION ALONG THE SPAN	114
FIGURE 3.2. NACA 63-415 AIRFOIL.....	115
FIGURE 3.3. ELEMENTARY SPAN OF WIND TURBINE.....	117
FIGURE 3.4. ELEMENTARY POWER COEFFICIENT ALONG THE SPAN	119
FIGURE 3.5. COLLECTION EFFICIENCY ALONG THE BLADE FOR DIFFERENT DROPLET DIAMETERS (FOG, DRIZZLE, RAIN)	121
FIGURE 3.6. ICE MASS RATE ALONG THE SPAN FOR DIFFERENT LIQUID WATER CONTENTS.	122
FIGURE 3.7. MAXIMUM ICE THICKNESS RATE ALONG THE SPAN FOR DIFFERENT LIQUID WATER CONTENT	123
FIGURE 3.8. AERODYNAMIC EFFECT ALONG THE BLADE FOR $LWC = 0.2 \text{ G} \cdot \text{M}^{-3}$	124
FIGURE 3.9. LUDLAM LIMIT FOR DIFFERENT LIQUID WATER CONTENT.....	126
FIGURE 3.10. FREEZING FRACTION ALONG THE SPAN FOR DIFFERENT TEMPERATURES (LWC $= 0.2 \text{ G} \cdot \text{M}^{-3}$).....	127
FIGURE 3.11. AERODYNAMIC REDUCTION FACTOR (A) POWER LOSS VS FREEZING FRACTION (B) POWER LOSS VS TEMPERATURE FOR DIFFERENT LIQUID WATER CONTENTS.	130
FIGURE 3.12. POWER LOSS AT $R/R \sim [0.93 \text{ } 0.96]$ FOR DIFFERENT LIQUID WATER CONTENTS.	132
FIGURE 3.13. REQUIRED DURATION FOR ICE ACCRETION ON WIND TURBINES TO MATCH THE SAME HIGHEST POWER LOSS UNDER ICING CONDITIONS ON HELICOPTER'S BLADES (FREEZING FRACTION 0.88, $R/R = [0.93 \text{ } 0.96]$) FOR DIFFERENT LIQUID WATER CONTENTS.....	134
FIGURE 3.14. MONTHLY DURATION OF ICING EVENTS FROM REANALYSIS OVER MOUNT- BÉLAIR SITE DURING JANUARY (FROM 1979 TO 2010).....	135
FIGURE 3.15. POWER UNDER ICING EFFECTS FOR $LWC = 0.2 \text{ G} \cdot \text{M}^{-3}$ AT $T = -12 \text{ } ^\circ\text{C}$ AND $T =$ $-13.5 \text{ } ^\circ\text{C}$, (A) POWER CURVE WITH AND WITHOUT ICING (B) ELECTRICAL POWER LOSS.	137

LIST OF ACRONYMS

AGL	Above Ground Level
AMIL	Anti-icing Material International Laboratory
CCN	Cloud condensation nuclei
CMC	Canadian Meteorological Center
DM	Double Moment
DJF	December January February
FAA	Federal Aviation Administration
FST	CMC/RPN standard file
GEM-LAM	Global Environment Multiscale Limited Area Model
GRIB	GRIdded Binary
IRM	Icing Rate Meter
M&Y	Milbrandt and Yau
NACA	National Advisory Committee for Aeronautics
NARR	North American Regional Reanalysis
NCAR	National Center for Atmospheric Research
NCEP	National Center for Environmental Prediction
NOAA	National Oceanic and Atmospheric Administration
NWP	Numerical Weather Prediction
PGSM	Programme Général de Sortie des Modèles de RPN
RPN	Recherche en Prévision Numérique
RTD	Resistance Temperature Detector
SGE	Sun Grid Engine
SLD	Supercooled Large Droplets
3DVAR	Three-dimensional Variational Data Assimilation

LIST OF SYMBOLS

A	Accumulation parameter
c	Chord [m]
CLWMR	Cloud liquid water mixing ratio [$\text{kg}\cdot\text{kg}^{-1}$]
C_p	Power Coefficient for clean blade
C'_p	Power Coefficient for iced blade
d_c	Cylinder diameter [m]
dx	grid spacing [m]
\dot{e}	Ice thickness rate [$\text{mm}\cdot\text{hr}^{-1}$]
E	Total collection efficiency
F	Freezing fraction
f	Power loss factor
h	Ice accumulation [mm]
h	Ice accumulation [mm]
\dot{h}	Ice thickness rate [$\text{mm}\cdot\text{hr}^{-1}$]
ISI	Icing severity index [mm]
IWC	Ice water content [$\text{g}\cdot\text{m}^{-3}$]
LWC	Liquid water content [$\text{g}\cdot\text{m}^{-3}$]
λ	Tip speed ratio
\dot{M}''	Mass rate of liquid water per unit surface [$\text{g}\cdot\text{m}^{-2}\cdot\text{s}^{-1}$]
MVD	Median volume diameter [μm]
μ_a	Dynamic viscosity of air [$\text{Pa}\cdot\text{s}$]
Ω	Rotational speed [RPM]
R	Length of the blade [m]
r	Radial position [m]
ρ_{ice}	Ice density [$\text{kg}\cdot\text{m}^{-3}$]
ρ_w	Water density [$\text{kg}\cdot\text{m}^{-3}$]
SLWC	Supercooled liquid water content [$\text{g}\cdot\text{m}^{-3}$]

St	Stokes number
SW	Monthly icing index [mm]
T	Temperature [$^{\circ}K$]
t_0	Time for starting simulation [hr]
$TCWC$	Total cloud water content [$g \cdot m^{-3}$]
t_h	The duration for ice accretion on helicopter [hr]
TMP	Temperature [$^{\circ}K$]
t_{wt}	The duration for ice accretion on wind turbine [hr]
U	Wind speed [$m \cdot s^{-1}$]
$UGRD$	Zonal wind speed [$m \cdot s^{-1}$]
$VGRD$	Meridional wind speed [$m \cdot s^{-1}$]
W_L	Weighting for liquid water content
W_t	Weighting for icing event duration
x	Position along the span [m]

INTRODUCTION

The increasing awareness with respect to preserving the environment has emerged after realizing the substantial level of damages caused by mishandling of nature. Over the last several decades research continues for safer ways to provide cleaner energy. The renewable energy market in Canada is expanding rapidly, due in large part to increased demand for energy sources that are environmentally preferable to, and more secure than, fossil fuels. In addition to the conscious effort, the increasing cost and the continuous depletion of fossil fuels have prompted the transition to clean energies that are abundant. Canadian utility companies have begun to diversify their energy portfolio by investing in the development of wind energy and other renewable energy sources. Despite a great potential of wind energy, the considerable technical barriers that affect wind energy systems operating in the Canadian climate and geography have so far hindered their widespread deployment in Canada. Weather related energy sources are subject to the variability of atmospheric conditions that can be reinforcing or problematic. Therefore, weather intelligence that accurately provides details about the present and the future atmospheric behaviors is required for a safe and profitable extraction of clean energy. Hau (2013) reported that onshore wind power is among the most cost-effective clean energy. On the other hand, this eco-friendly alternative is exposed to challenging near-surface icing conditions. These hazardous events will therefore affect automatically the power industry (Bernstein et al., 2011).

At high altitudes in the troposphere in-cloud icing is the dominant atmospheric condition that imposes economic challenges and safety concerns to aircraft navigation around the globe. On the other hand, at lower atmospheric levels near the surface, only the mountainous and cold climate regions are frequently exposed to icing events that can endanger near-surface structures, including wind turbines and power lines. Atmospheric icing issues have been studied from two points of view; by analyzing the meteorological conditions (cloud physics and cloud dynamics) which lead to icing events and from a mechanical perspective (adherence, accretion, icephobic materials...).

The direct meteorological key parameters : liquid water content, cloud droplets size, wind speed and temperature, control the quantification of in-cloud icing. These parameters do not contribute equally to the intensity of icing events. For this reason, an appropriate assessment of the severity of the icing event requires weighting factors which reflect the level of influence of each parameter. In addition, elevated topography with accentuated gradient slopes contribute significantly in originating near-surface orographic clouds and generating larger sizes of cloud droplets. Therefore, to accurately evaluate the icing events over complex terrains, it is crucial to involve an advanced microphysics scheme and meteorological variables at high resolution.

In-cloud icing

Cloud physics and ice accretion

In addition to the influential impacts of cloud on radiation and precipitations, the presence of cloud is a prerequisite for the occurrence of in-cloud icing. Therefore, it is crucial to understand cloud physical and dynamical mechanisms that favor icing events. Several atmospheric lifting processes (orographic, convective, frontal) contribute in triggering cloud formation. Within the subfreezing range of temperatures, cloud liquid water content and the associated droplets sizes, together with the wind speed, regulate the potential of the icing severity accordingly.

The atmospheric supercooled liquid water is the main indicator of the potential occurrence of atmospheric icing, either in-cloud or precipitation icing (Marwitz et al., 1997). Ice accretion on structure can be identified as glaze and rime. This type of icing event is determined by the following meteorological variables: air temperature, wind speed, size of supercooled water droplets and atmospheric water-content (Felin 1988).

Topography and icing events

Within the troposphere, various parameters such as temperature, moisture, air density, solar radiation and wind speed vary according to the height above sea level (Whiteman 2000). The effect of the topography and the position of the measuring station in combination with the height of wind turbines do not allow for a precise estimation of wind speed (Fortin et al 2005b) and consequently the icing events.

A mountain, depending on its size, shape, orientation, as well as the moisture of the air mass in a given area, can affect the regional climate by acting as a barrier to the regional

flows. The latitude, altitude, continentality, and exposure to regional circulations provide a general description of the climate of the mountainous region (Whiteman 2000). Microclimate factors will not be discussed; they are not the defined focus of this dissertation.

The concept and the classification of mountainous areas are completely arbitrary (Marsh, 2002). Neither qualitative nor quantitative distinction is established to identify the difference between mountains and hills. In North America, it is common to consider 600 meters as a limit that distinguishes the difference between mountains and hills (Thompson 1964). The altitudinal range of 600 m is enough to alter the vertical profile of the atmosphere (Roger 2008). Troll (1973) describes high mountains according to the features of a given landscape and the microclimate in the present and in the past near ground level. Bailey (1990) reported that rime ice can be expected for at least 10% of the time, during cold weather when the altitude is at approximately 700 m. Commonly, rime ice occurs in areas where supercooled cloud episodes often appear, especially when cloud bases are below mountain summits, strong wind speed, and large surfaces which collect supercooled droplets. Moreover, the latitude is an important factor that affects the climate of any given site because of the angle of solar radiation and most importantly because of its exposure to latitudinal belts of high and low pressure. These conditions reflect the potential significant rime accumulation on middle latitudes and Polar Regions (Whiteman 2000).

In reference to complex terrains located in the province of Quebec (Canada), the Mount-Bélair (485 m), located near Québec city, was selected to carry out ice accretion experiments. The topography of the Mount Bélair site as well as its proximity to the St-

Lawrence river makes it a prime location for the formation of atmospheric icing (Hardy et al., 1998). Similarly, the Mount Valin (980 m) in the Saguenay region is considered an ideal location for ice accretion (Savadjiev et al., 1996, Druez et al., 1988).

Challenges and motivations

Hazard assessment of icing events

In various studies that have addressed the accretion of ice, the severity of icing events was often assessed either by the duration of events (eg. Comeau et al., 2007), the accumulation rate (eg. Byrkjedal and Berge, 2009) or Severity index combining key parameters using weighting factors (eg. Lamraoui et al., 2013; Bernstein et al., 2006). Despite the fact that icing severity is controlled mainly by the liquid water content, droplet size and temperature (Bernstein et al., 2006), Hansman (1989) reported that the liquid water content and temperature have a dominant contribution.

The occurrence of icing events is often associated with the concern over the potential risk that can be generated. The assessment of the hazard level depends on weather conditions and the vulnerability of structures that intercept supercooled water. Depending on the field of application and the nature of structures affected by the ice, a large number of studies have assessed the seriousness of the economic and the safety consequences that range from perturbation to disaster. Among the structures that are vulnerable to ice accretion are the following; aircraft (eg. Cole and Sand, 1991; Gent et al., 2000), wind turbines (eg. Lamraoui et al., 2014; Etemaddar et al., 2014); power lines (Farzaneh 2008; Sakamoto, 2000), meteorological instruments (Fortin et al., 2005b; Tammelin et al., 1998). The hazardous impact of icing events on wind turbines is not exclusive to high amount of

ice accumulation; several studies (Marjaniemi and Peltola 1998, Jasinski, et al., 1998) demonstrated that even modest amounts of ice accumulation on the leading edge of the blade deteriorate substantially the aerodynamic of the blade and consequently reduce the expected electric power. In addition, Magued et al (1989) has associated 0.055% of the Canadian power failure to the occurrences of ice accretion on Power lines and telecommunication towers. This rate of power outage is five times higher than reliability level in the Canadian Design Code (CSA-S37). Moreover, in reference to tall structures under icing conditions, there is a lack in identifying the vertical profile of icing events (Makkonen et al., 2014). A previous experimental study that took place in Murdochville (Quebec), confirmed that the severity of icing events depends not only on the accumulation rate but also on the length of icing events (Fortin et al., 2005a).

Mesoscale Modeling of Atmospheric icing

In atmospheric science, the horizontal mesoscale ranges from a few kilometers to several hundred kilometers, where the vertical scale covers all the troposphere (Pielke 2001) with a time scale that covers one hour to yearly activity. During the last two decades the study of the microphysics of clouds has made great advances. Relative humidity is not involved in the icing rate calculations; however it is still considered the key parameter for icing estimations and a very good indicator for icing risk assessment. In addition to temperature and wind speed, the droplet size distribution and the liquid water content are the main parameters for icing. The lack of direct measurements of icing events has motivated researchers in atmospheric icing to use analytical, empirical, or numerical models of ice accretion as a function of meteorological variables (Makkonen, 1998 ;

Draganoiu et al., 1996; Jones, 1998).

Many numerical weather prediction models were used to produce an accurate forecast the occurrences of icing events in order to match field observations. As an example of these models, namely the ALADIN, HIRLAM, NCAR CAM, UKMO, MM5, WRF and GEM. Vassbo et al (1998) pioneered the use of the numerical weather prediction model (HIRLAM) to produce an atmospheric icing forecast. Drage and Hauge (2008) used the MM5 mesoscale model to simulate atmospheric icing by employing the microphysics scheme of Reisner (1998). Milbrandt et al (2006) have developed a sophisticated microphysics scheme that continually evolves. This scheme was initially created for the Mesoscale Compressible Community Model MC2 (Benoit et al., 1997) that then was transferred to the model GEM which is utilized in this thesis.

The RPN/CMC (Recherche en Prévision numérique/Centre Météorologique Canadien) Physics library is a comprehensive resource for advanced microphysics schemes; however they are not yet fully explored and used for atmospheric icing forecasts. These schemes provide information about icing intensity, weather hazards, such as freezing rain, mixed precipitation, fog or blowing snow (Guan et al., 2002).

According to Anthes (1983), studies using limited area mesoscale numerical models have considerably improved the skill of weather forecasting in general. An accurate prediction of natural icing hazards is very important; however numerous atmospheric icing algorithms need improvement, as is the case with the icing algorithm of Thompson (Thompson et al., 1997) which overestimates the icing forecast. Contrary to this, the Canadian microphysics scheme of Tremblay et al (1995) often underestimates icing events,

and provide a binary Yes-No forecast, without any information regarding the intensity of icing (Tremblay and Glazer, 2000). Most freezing forecasts are based on the presence of a warm layer. In spite of this, freezing event hydrometeors formed without a warm layer are often observed (Strapp et al., 1996). A study focused on the central England area (model run 3 days 7-8-9 December 1990) by Wareing and Nygaard (2009), resulted with a strong match between measurements and accretion simulated by WRF. In this study the model considers only the icing rate higher than $10 \text{ g}\cdot\text{h}^{-1}$.

Objective

This dissertation is the results of a joint collaboration between Hydro-Québec's research institute (IREQ), École de Technologie Supérieure and The Anti-Icing Materials International Laboratory (AMIL) which is an engineering research laboratory associated with the UQAC and it specializes in the certification of de/anti-icing fluids used on airplanes before takeoff.

In general, this thesis targets all near-surface structures that are sensitive to ice accretion and gives a particular attention to the industry of wind turbines under icing conditions. The diversity of the cold Canadian climate and its topographic heterogeneity impose major challenges on structure; (i) icing conditions and (ii) complex terrain.

The main objective of this dissertation focuses on the risk assessment associated with near-surface structures under icing conditions, over simple and complex terrains. In order to relevantly assess the hazards of icing conditions, this thesis aims to quantify the intensity of icing events based on an original icing severity index (ISI). The ISI involves different weighting factors that reflect the contribution of the key parameters that control the icing

events accordingly. In addition, this thesis gives particular attention to the occurrence of icing events and their impact on the performance of wind turbines.

This thesis aims at representing the climatology of icing events that occurred historically, displaying averages and extreme values of parameters that describe icing events like frequency, duration, intensity, and wind properties. To achieve this icing climatology, this thesis uses North American Regional Reanalysis spanning a 32 year time period and a mesoscale modeling that spans a 15 year time period.

Structure of the thesis

This thesis consists of bringing together three published peer-reviewed articles, each of these articles represents a chapter of this dissertation and tackles one section of the ensemble of this project. The first Chapter represents simultaneously the preliminary step for the characterization of icing events and the primary section for the foundation of the icing severity index that assesses the severity level of icing events. The results presented in this chapter utilize a very large database at pressure level of 1000 mb obtained from NARR to identify the near-surface climatology of icing events during an unprecedented long time period of 32 years (1979-2010). The cylinder model was used to quantify icing events. For validation purpose, comparisons were made with observation from case studies over complex terrain, simple terrain and the ice storm 1998. The first article revealed that the use of NARR data has a limitation regarding the detection of icing events over complex terrains. For this reason, the second article in the second chapter intervened to improve the resolution and implicate advanced microphysics scheme. The second article used NARR

data to initiate the mesoscale model GEM-LAM followed by double-nested downscaling to obtain three-dimensional high resolution microphysics and in-cloud icing climatology.

The icing severity index (ISI) that has been addressed in chapter 1 and 2 involves meteorological weighting factors that determine the severity level of the icing events. Subsequently, in an effort to explore additional factors that contribute to the significance of icing events on wind turbine production, chapter three focuses exclusively on the impact of icing events on wind turbine production. An original power loss factor which is a potential weighting for the icing severity index is introduced. In addition, this chapter addresses the location and the type of the accumulated ice on the blade, the corresponding meteorological conditions and consequently the resulting loss of wind energy.

References

- Anthes, R. A., 1983. A review of regional models of the atmosphere in middle latitudes. *Mon. Weather Rev.* 111(6), 1306-1335.
- Bailey, B. H., 1990. The Potential for Icing of Wind Turbines in the Northeastern U.S. *Windpower* 1990: 286-291.
- Benoit, R. and Co-authors., 1997. The Canadian MC2: A Semi-Lagrangian, Semi-Implicit Wideband Atmospheric Model Suited for Finescale. *Mon. Weather Rev.* 125, 2382-2415.
- Bernstein, B. C. and Co-authors., 2006. The New {CIP} Icing Severity Product. Proc. of {AMS} *Conference on Aviation Range and Aerospace Meteorology*.
- Bernstein, B.C., Wittmeyer, I., Gregow, E. and Hirvonen, J., 2011. LAPS-LOWICE: A real-time system for the assessment of near-surface icing conditions. *Proc 14th IWAIS*, Chongqing, China, May 8 - May 13, 2011.
- Byrkjedal, Ø. and Berge, E., 2009. Meso-scale models shows promising results in predicting icing, *Proc. of EWEC*, Marseille, France
- Cole, J., and W. R. Sand., 1991. Statistical Study of aircraft Icing Accidents. *Proc. 29th Aerospace Sciences Meeting*, Reno, NV, Amer. Inst. Aero. And Astro., *AIAA 91-0558*.
- Comeau, M. Masson, C. Morency, F. and Pelletier, F., 2007. Estimation of icing events using NARR data. *Proc 12th IWAIS*, Yokohama, Japon
- Drage, M.A. and Hauge, G., 2008. Atmospheric icing in a coastal mountainous terrain. Measurements and numerical simulations, a case study. *Cold Reg. Sci. Technol*, 53(2) 150-161.
- Draganoiu, G., Lamarche, L. and McComber, P., 1996. A Computer Model of Glaze Accretion on Wires. *J Offshore mech arct.* 118(2), 148-157
- Druez, J., M Comber, P. and Félin, B., 1988. Icing rate measurements made for different cable configurations on an icing test line at Mt. Valin. *Proc 4th IWAIS*, Paris, France, pp.477-485.
- Etemaddar, M., Hansen, M.O.L. and Moan, T., 2014. Wind turbine aerodynamic response under atmospheric icing conditions. *Wind Energy*, 17(2), p.241-265.
- Farzaneh, M., 2008. Atmospheric Icing of Power Networks. Berlin: Springer, 381 pp
- Felin, B., 1988. Freezing Rain in Quebec. Field Observations Compared to Model Estimations. *Proc 4th IWAIS*, Paris. 119-123.

- Felin, B., 1976. The observations of rime and glaze deposits in Quebec. Canadian Electrical Association Spring Meeting, 22-24 March 1976, Toronto, 53 p
- Fortin, G., Perron, J. and Ilinca., A., 2005a. A study of Icing Events at Murdochville – Conclusions for the Wind Power Industry. Quebec Premier Wind Energy Event, *International Conference, Wind Energy Remote Regions*, Magdalene Islands, Québec, Canada
- Fortin, G., Perron, J. and Ilinca A., 2005b. Behaviour and Modeling of Cup Anemometers under Icing Conditions, *Proc 11th IWAIS*, Montreal, Canada, June 12-16, 2005
- Gent, R. W., Dart, N. P. and Cansdale, J. T., 2000: Aircraft icing. *Philos. Trans. Roy. Soc.*, 358A, 2873–2911.
- Guan, H., Cober, S.G., Isaac, G.A., Tremblay, A. Méthot, A., 2002. Comparison of Three Cloud Forecast Schemes with In Situ Aircraft Measurements. *Wea. Forecasting*. 17, 1226-1235.
- Hansman, R.J., 1989. The influence of ice accretion physics on the forecasting of aircraft icing conditions. Preprints, *3rd Int'l Conf. on the aviation weather system*, Anaheim CA.
- Hardy.C., Brunelle .J., Chevalier, J., Manoukian, B. and Vilandre, R., 1998. Telemonitoring of climate loads on Hydro-Quebec 735 KV lines. *Atmos. Res.* 46(1-2), 181-191.
- Hau, E., 2013. Wind turbine economics. *Wind Turbines: Fundamentals, Technologies, Application, Economics*, 3rd edition, Springer, 845-870.
- Jones, K.F., 1998. A simple model for freezing rain ice loads. *Atmos. Res.* 46(1-2), 87–97.
- Lamraoui, F., Fortin, G., Benoit, R., Perron, J. and Masson, C., 2013. Atmospheric icing severity: Quantification and mapping. *Atmos. Res.* 128, 57-75.
- Lamraoui, F., Fortin, G., Benoit, R., Perron, J. and Masson, C., 2014. Atmospheric icing impact on wind turbine production. *Cold Reg. Sci. Technol.* 100, 36–49.
- Magued, M.H., Bruneau, M. and Dryburgh, R.B., 1989. Evolution of Design Standards and recorded Failures of Guyed Towers in Canada. *Can J civil eng.* 16, 725-732.
- Marjaniemi, M. and Peltola, E., 1998. Blade Heating Element Design and Practical Experiences. *BOREAS IVFMI*, Hetta, Finland 197–209.
- Makkonen, L., 1998. Modelling power line icing in freezing precipitation. *Atmos. Res.*46, 131-142.

- Makkonen, L., Lehtonen, P. and Hirviniemi, M., 2014. Determining ice loads for tower structure design. *Engineering Structures*, 74, 229-232.
- Marsh, J., 2002. Mountains of the world. a global priority. *Environ Rev*, 10(3), 191-193.
- Marwitz, J., Politovich, M., Bernstein, B., Ralph, F., Neiman, P., Ashenden, R. and Bresch, J., 1997. Meteorological conditions associated with the ATR72 aircraft accident near Roselawn, Indiana, on 31 October 1994. *Bull. Amer. Meteor. Soc.* 7
- Milbrandt, J.A. and Yau, M.K., 2006. A Multimoment Bulk Microphysics Parameterization. Part IV: Sensitivity Experiments. *J. Atmos. Sci.* 63(12), 3137-3159.
- Pielke, R A., 2001. Mesoscale Meteorological Modeling, Volume 78, Second Edition (International Geophysics) Academic Press; 2 edition (December 13, 2001) 676 pages
- Reisner, J., Rasmussen, R.J. and Bruintjes, R.T., 1998. Explicit forecasting of supercooled liquid water in winter storms using the MM5 mesoscale model. *Quart. J. Roy. Meteor. Soc.*, 123B, 1071-1107.
- Rogers, R.R., 1989. A short course in cloud physics. Third Edition International Series in Natural Philosophy, Butterworth-Heinemann; 3 edition 304 p.
- Roger, G.B., 2008. Mountain weather and climate, Cambridge university press 3rd edition
- Sakamoto, Y., 2000. Snow accretion on overhead wires. *Phil. Trans. R.Soc. London*, 358(1776), 2941-2970.
- Savadjiev, K., Latour, A. and Paradis, A., 1996. Estimation of Ice Accretion Weight from Field Data Obtained on Overhead Transmission Line Cables. *Proc 7th IWAIS*. Chicoutimi (QC), Canada, pp. 125-130
- Strapp, J. W., Stuart, R. A. and Isaac, G. A., 1996. A Canadian climatology of freezing precipitation and a detailed study using data from St. John's, Newfoundland. *Proc. of the FAA International Conference on In-flight Aircraft Icing*, Vol. II, DOT/FAA/AR-96/81, II, 45-56.
- Tammelin, B. et al., 1998. Ice Free Anemometers. BOREAS IV, Proceeding of an International Meeting. *Finnish Meteorological Institute*. Helsinki, pp. 239-252.
- Tremblay, A., Glazer, A., Szyrmer, W., Isaac, G. and Zawadzki, I., 1995. Forecasting of Supercooled Clouds. *Mon. Weather Rev.* 123(7), 2098-2113.
- Tremblay, A., and Glazer, A., 2000. An Improved Modeling Scheme for Freezing Precipitation Forecasts. *Mon. Weather Rev.* 128, 1289-1308.

Troll, C., 1973. High mountains belts between the polar caps and the equator: their definition and lower limit. *Arct. Alp. Res.*, 5(2-3), A19-A27

Vassbo, T., Kristjansson, J.E., Fikke, S.M., Makkonen, L., 1998. An investigation of the feasibility of predicting icing episodes using numerical weather prediction model output. *Proc 8th IWAIS*, 343-347, Reykjavic.

Wareing, B., and Nygaard B., 2009. WRF Model simulation of wet snow and rime icing incidents in the UK, *Proc 13th IWAIS*, Andermatt.

Whiteman C. D., 2000. *Mountain Meteorology: Fundamentals and Applications* Oxford University Press, USA; 1st edition (May 15, 2000) p.355

CHAPTER 1

ATMOSPHERIC ICING SEVERITY: QUANTIFICATION AND MAPPING

*This Chapter is published in the form of an original scientific article
in the journal of*

Atmospheric Research, 2013, vol 128, p. 57-75

dx.doi.org/10.1016/j.atmosres.2013.03.005

Fayçal Lamraoui ^{1*}, Guy Fortin ², Jean Perron ¹, Robert Benoit ³, Christian Masson ³

¹ *The Anti-Icing Materials International Laboratory, University of Quebec at Chicoutimi*

² *Bombardier Aerospace*

³ *École de technologie supérieure, University of Quebec*

* Corresponding Author address:

Fayçal Lamraoui

*The Anti-Icing Materials International Laboratory, University of Quebec at Chicoutimi
555, boulevard de l'Université, Chicoutimi, QC, G7H 2B1 Canada*

Email: faycal.lamraoui@gmail.com

1. ATMOSPHERIC ICING SEVERITY: QUANTIFICATION AND MAPPING

Abstract

Atmospheric icing became a primary concern due to the significant impact and hazardous conditions of its accretion on structures. The objective of this study is to provide a map of icing events over 32 years (1979 to 2010) that describes the severity of winter icing. This information will prove useful to prevent damages and economical losses due to icing events by documenting the risk factor. To validate the icing climatology method, two case studies involving two topographically contrasting sites were selected: a simple terrain site which is the airport of Bagotville, near Saguenay (Canada) and a complex terrain site located in Mt Bélair, near Quebec City (Canada). Ice accumulation calculated by the use of reanalysis data was quantified using ice accretion on a cylinder model. Comparison between measurement and the model over Bagotville revealed insignificant differences in ice accumulation less than 0.3 mm, and in duration of icing events less than 0.2 day. On the other hand, during winter months, the calculation that showed a maximum of 60 mm in January 1999 over Mt Bélair site also had an underestimation of ice accumulation that varies from 5 mm to 16 mm. The horizontal resolution of NARR imposes a challenge on the calculation of icing events over complex terrains, especially during the months of November and March when air temperature is near freezing point. Taking into account the liquid water content, the duration of icing events and the classes of icing events as weighting factors, the icing severity index based on reanalysis data was introduced to assess the severity level of icing events, covering the north-east of Quebec including Quebec City, Sept-Iles, the east of Saguenay, the lower St Lawrence River and the Gaspé region. Consequently, an icing severity index mapping that represents the climatology of in-cloud atmospheric icing was produced.

1.1 Introduction

Atmospheric icing, which refers to all meteorological conditions that result in ice accumulation (Fikke, 2005), represents a serious threat to numerous vulnerable structures as well as to human daily life activities, by posing a serious public safety threat. It continues to be a contributing factor of civilian and military aircraft accidents (Anthes, 1983; Isaac et al., 2001; Petty and Floyd, 2004; Green, 2006). Icing is more evident in northern countries because they experience it at ground level. Both wet and dry atmospheric icing processes result from supercooled droplets freezing on a surface when its temperature falls below 0 °C (Jacobson, 2005; Ahrens, 2007).

The supercooled liquid water is liquid water in an unstable state which remains in the liquid phase until -40 °C. When compared to ice at the same temperature, supercooled liquid water is characterized with a higher vapor pressure. These conditions make supercooled liquid water thermodynamically unstable compared to ice (Rock, 2003). Under these circumstances, the latent heat released by the freezing process does not compensate the energy required to create the solid–liquid interface. Consequently, the liquid water continues to cool without becoming frozen. This state can be destabilized and liquid water will immediately freeze when it comes into contact with a solid surface or a particular type of aerosol called freezing nuclei or a small perturbation would be sufficient to trigger an abrupt change to a solid phase (Huschke, 1959; Debenedetti, 1996; Rock, 2003). In the absence of aerosols that represent freezing nuclei, the supercooled liquid water freezes to form ice through homogeneous nucleation, for example at -40 °C in high clouds. On the other hand, heterogeneous nucleation occurs in the presence of freezing nuclei on which ice

forms and may increase (Debenedetti, 1996). Supercooled rain and drizzle drops mainly result from melted snow that falls through a warm layer of air which is embedded between two subfreezing layers of air. In mid-latitude regions, the falling hydrometeors become supercooled near the surface when the warm frontogenesis of an extratropical cyclone penetrates a subfreezing zone (Strapp et al., 1996; Marwitz et al., 1997; Gyakum and Roebber, 2001).

Through a statistical study, Bernstein et al. (1998) investigated the relationship between Aircraft Icing and Synoptic-Scale Weather pattern. The results indicated that the regions with the highest icing conditions were arctic, West Coast, and East Coast air masses; 250–600 km ahead of warm fronts; in regions of freezing drizzle, freezing rain, and ice pellets; and in regions with cloud coverage when there was no precipitation. Icing events were also associated with low pressure centers and troughs.

Due to the higher air density in cold regions, cold climate sites have vast wind energy potential which is approximately 10% higher than other climate regions (Fortin et al., 2005). Also wind turbine farms located at higher altitudes store more wind energy compared to lower altitudes (Parent and Ilinca, 2011). Thus, higher wind potential areas are often more exposed to increased icing risk.

Meteorologists tend to use 30-year data sets to show the climatology. Various icing maps have been developed in order to locate areas in which icing may endanger wind energy production. A number of different concepts have been used to map atmospheric icing. These concepts tend to consist of the yearly number of icing events, icing days, number of icing hours, as well as icing severity index.

The first European version of atmospheric in-cloud icing map was produced as part of the WECO EU project (Tammelin and Säntti, 1998; Tammelin et al., 2000). The average annual number of icing days was obtained from 120 meteorological observation stations spread over Europe between 1991 and 1996 (Tammelin et al., 1999). High relative humidity (>95%) and subzero temperatures (<0 °C) have been widely used for icing assessments (Laakso et al., 2003), but this approach has failed to detect icing events that were identified by ice detectors (Tammelin et al., 2005). An earlier study by Laakso et al. (2003) had demonstrated that 33% of all ice detectors located at 80 m level showed icing accumulations at a relative humidity below 95%. Using high relative humidity and sub-zero temperatures to assess icing is standard if numerical model analysis is being used for the assessment. The reason that this fails to detect some icing events caused by icing detectors is that the models can have errors for both the relative humidity and temperature, and also because freezing precipitation can fall through sub-saturated environments to the surface.

Furthermore, icing detection methods that are based on visibility and cloud base height are too expensive and are not generally used for site assessments (Parent and Ilinca, 2011). Moreover, the cloud base height method underestimates mass of accreted ice (Tammelin et al., 2005). Different studies have used a variety of time periods (10, 20 or 30 years) during the mapping of atmospheric icing. For example Tammelin and Säntti (1998) attempted to illustrate icing distribution over Europe between 1996 and 1998, using data from 100 meteorological stations. Icing was detected by evaluating observations of cloud base height at various airport stations in Norway. Simultaneously, the WRF model was employed to generate the meteorological variables required for calculating icing. It is

important to note that severe icing events can occur when in-cloud icing persists for long periods of time. Byrkjedal and Berge (2008) created a map of simulated atmospheric icing based on NWP output for the year 2005 over Norway. It showed the duration (in hours) of icing accumulation for a one-year period by summing up the number of hours when the icing rate was higher than $10 \text{ g}\cdot\text{h}^{-1}$. The icing rate was calculated using ice accretion model and meteorological variables (liquid water content, wind speed at 80 m in height and air temperature) obtained from running the WRF model. Dobesch et al. (2003) carried out a study that produced a rime ice map for all of Scandinavia during the winter months (January, February and March); its timeline covered the years 1999 through 2002. The map displayed the mean number of icing days. In-cloud icing was recorded from all available stations across Scandinavia only when the temperature was below $0 \text{ }^{\circ}\text{C}$ and cloud base height was less than 200 m (or visibility below 300 m). A study on freezing precipitation conducted by Vedin (1998) included a map displaying the annual number of hours of freezing rain and drizzle from observations taken over the period 1961-1990 in Sweden. Yip (1995) introduced a mapping of freezing precipitation over Canada by representing an average of a 30-year timeline. Ice accretion of this mapping was based on the semi-empirical model of Chaine and Skeates (1974) which assumes the freezing fraction to be one and clear ice density $900 \text{ kg}\cdot\text{m}^{-3}$. Horizontal ice accretion which is considered equivalent to freezing precipitation rate, and vertical ice accretion which is proportional to precipitation rate and wind speed (McKay and Thompson, 1969) were combined to conclude a radial ice thickness caused by freezing precipitation only on a cylindrical object (Chaine and Castonguay, 1974; Stallabrass and Hearty, 1967). Also Stuart and Isaac (1999)

presented national maps that show the climatology of freezing precipitation in Canada and the occurrence frequencies of freezing rain and freezing drizzle. The maps were based on observations from different stations all over Canada. Bernstein et al. (2007) created 14 years climatology of icing conditions over Canada and continental U.S, based on balloon borne soundings of temperature and moisture and observations at surface level of cloud cover and precipitation. This method was previously validated by Bernstein et al (2005).

Numerous studies have been attempted to quantify icing events, although none have been approached from the severity point of view during a climatologically extended period of time which involves multiple influencing factors. Whereas, in the current study, atmospheric icing and its severity were quantified, by using a numerical model to estimate ice accretion on a cylindrical object. The model used the meteorological data such as; wind speed, air temperature, liquid water content, median volume diameter and the duration of icing events. These variables were extracted from reanalysis data. An icing severity index defined as (ISI) was introduced in order to better represent the potential dangers of icing events that occurred in the region of study during a long time period 32 years (from 1979 to 2010). Accumulated icing alone cannot be viewed as representative of the different levels of icing severity and icing risk. This study introduces a new type of severity index. Fortin et al. (2005) have confirmed that the severity of icing events depends not only on icing accumulation rates, but also on the duration of these events. Furthermore, Makkonen (1984) has demonstrated that the duration of an ice storm becomes an important factor influencing mean ice growth rate.

1.2 Methodology

In order to represent icing, the meteorological data related to the generation of atmospheric icing was statistically analyzed. Considering the location of the study (Quebec, Canada), the North American Regional Reanalysis (NARR) was a cost-effective and reliable option for collecting the necessary data. The model presented in this study detects in-cloud icing events, quantifies icing accumulation and assesses in-cloud icing severity by mapping its climatology. The model presented in this study identifies in-cloud icing events, quantifies icing accumulation and assesses in-cloud icing severity by mapping its climatology. In accordance with the meteorological variables extracted from NARR, the model evaluates only the severity of in-cloud icing near ground level. In these circumstances, the model deals exclusively with supercooled stratiform clouds at low altitudes or supercooled fog. Therefore, vulnerable structures to icing are affected near ground level, for example wind turbines as well as aircrafts only during the take-off.

The validation of the model is based on two case studies that are located over Mt Bélair (~20 km west of Quebec City) and Bagotville. The icing severity index is obtained by modeling of in-cloud icing based on cloud water, wind speed and temperature from re-analysis data at 1000 mb level. In order to compare simulation and measurements of in-cloud icing over Mt Bélair and Bagotville, a monthly icing accumulation and duration of icing events were calculated, for the months November and December 1998, as well as January, February and March 1999.

In addition, an application involving the calculation of ice accumulation during the January 1998 ice storm over the southern region of Quebec (Montreal area) was achieved

through the use of the precipitation rate, air temperature and wind speed obtained from reanalysis. This ice calculation utilized the same model as did the two case studies previously mentioned, except the liquid water content was calculated from the supercooled precipitation rate that comes from reanalysis instead of cloud water.

Topographically, the Montreal area and Bagotville are viewed as simple sites: they are at low altitude close to sea level. The Mt Bélair site which is a complex terrain near Quebec City, is at an altitude of 480 m, and is frequently exposed to icing events. Since 1994, the Mt Bélair site has been adapted for ice accretion experiments. Its topography as well as its proximity to the St-Laurence River makes it a prime location for the formation of atmospheric icing (Hardy et al., 1998). The IRM instrument, developed by Hydro-Quebec, is a device that automatically detects icing accumulation (Claffey et al., 1995; Stein, 1993) and captures all types of atmospheric icing (in-cloud icing, freezing rain). The IRM is composed of a cylindrical probe 6.2 mm in diameter and 25.4 mm long (Laflamme, 1993; McComber et al., 1996). In the absence of icing accumulation, an oscillator causes this sensing probe to vibrate axially at a resonant frequency of 40,000 Hz. An icing accumulation threshold of 0.51 mm is required in order to trigger the probe. Once accumulation reaches the preset trip point, an automatic de-icing procedure is activated by means of an internal heater (McComber et al., 1996). A series of measurements of in-cloud icing over Mt Bélair and Bagotville sites were obtained from AMIL (Anti-icing Material International Laboratory, Chicoutimi, Canada). In-cloud icing was measured using IRM located high up on a tower in order to record in-cloud icing events above the site.

Fig. 1 shows the Hydro Quebec icing-rate meter used by AMIL. This device includes a Rosemount sensor and a RTD (resistance temperature detector) that both measure the temperature of the IRM (Fortin et al., 2005).



Figure 1.1. A Hydro-Quebec icing-rate meter (AMIL-UQAC).

1.2.1 Reanalysis Data

In the present study, the meteorological variables used to capture icing events originated from reanalysis. The North American regional reanalysis (NARR) is a joint project, undertaken by two U.S. agencies, the National Center for Environmental Prediction (NCEP) and the National Center for Atmospheric Research (NCAR). NARR contains four-dimensional fields of various meteorological parameters in space and time. Compared to previous global versions of reanalysis, NARR has an improved spatial resolution of 32kmx32km horizontally at 29 pressure levels. They were generated utilizing Eta 32km/45-layers model, with a three-hour time resolution during which eight daily analyses are provided, from 1979 until the present (Mesinger et al., 2006); however it covers only North America.

There are two types of NARR files which have GRIB format: these are classified as "NARR-a" and "NARR-b" (NCEP, 2004). Unlike The "b" file that contains instantaneous values, the "a" file type that was chosen for this study contains an averaged values. Alongside this, the GRIB file called AWIP32 for fixed fields (NARR homepage) is used, in order to obtain NARR topography (Mesinger et al., 2006).

The extracted meteorological variables used in this study for icing calculation were:

TMP: Temperature [K], CLWMR: Cloud liquid water mixing ratio [$\text{kg}\cdot\text{kg}^{-1}$] (liquid water [kg]/dry air [kg]), UGRD, VGRD: Zonal and meridional wind speed [$\text{m}\cdot\text{s}^{-1}$]

The NARR fields are computed by a data assimilation scheme based on the ETA NWP model which uses the Ferrier cloud microphysics to predict clouds and precipitation. Nygaard et al. (2011) showed that the Ferrier scheme slightly underestimates the supercooled liquid water content compared to direct measurements.

Only supercooled cloud water (i.e. $\text{TMP} < 0\text{ }^{\circ}\text{C}$) at level 1000 mb was considered for icing calculation. The cloud water at level 1000 mb was chosen from NARR, because it represents the only pressure level with cloud water that is available near the ground surface.

The variables used to calculate ice, cover the whole NARR zone with a 349×277 horizontal grid. For each month, each variable used is a 3D space-time (x,y,t) matrix: $349 \times 277 \times N_b$ ($N_b = 8 \times$ number of days for each month). N_b refers to the number of NARR data records during one month.

1.2.2 Icing calculations

In this study, ice accretion was calculated on two types of solid obstacles: on a cable 25 mm in diameter for the purpose of comparison, while on an icing-rate meter (IRM) of

cylindrical shape with a diameter of 6.2 mm in order to perform the mapping of the icing severity index. The investigation of icing and its severity was focused on winter months (December, January and February) from 1979 until 2010.

Eq. (1) describes the fundamental physics of time-dependent water collection rate per unit surface on a cylinder (Messinger, 1953).

$$\dot{M}'' = E \cdot LWC \cdot U \quad (1)$$

The collected mass rate per unit surface \dot{M}'' [$\text{g}\cdot\text{m}^{-2}\cdot\text{s}^{-1}$] depends on the parameters; LWC the liquid water content [$\text{g}\cdot\text{m}^{-3}$], the wind speed U [$\text{m}\cdot\text{s}^{-1}$] and collection efficiency E .

According to Walton and Woolcock (1960), the local collection efficiency E for a cylinder is calculated using Eq. (2). It represents the ratio of impinging droplet mass flux to freestream droplet mass flux ($U\cdot LWC$) on a cylinder.

$$E = \frac{St^2}{(St+0.7)^2} \quad (2)$$

St is the Stokes number, which is calculated using Eq. (3):

$$St = \frac{U \cdot (MVD)^2 \cdot \rho_w}{9 \cdot \mu_a \cdot d_c} \quad (3)$$

Where U is the wind speed in $\text{m}\cdot\text{s}^{-1}$, while MVD is the cloud droplet median volume diameter, ρ_w represents the water density in $\text{kg}\cdot\text{m}^{-3}$, d_c represents the cylinder diameter in m and μ_a is a dynamic viscosity of air in $\text{Pa}\cdot\text{s}$, calculated using Clift's empirical correlation (Brodkey and Hershey, 1988). The median volume diameter (MVD) is assumed to be $18 \mu\text{m}$ in this study. Winter stratiform clouds typically have a median volume diameter between $15 \mu\text{m}$ and $20 \mu\text{m}$ (Isaac, 1991; Cober et al., 1995).

It is known that atmospheric supercooled liquid water holds a potential for the occurrence of atmospheric icing, either for in-cloud or precipitation icing (Bernstein et al., 2000; Ratvasky et al., 1999; Rasmussen et al., 2005; Sand et al., 1984). The supercooled liquid water (SLWC) was extracted from NARR data by multiplying air density by cloud liquid water mixing ratio, and taking only subzero temperatures into account.

$$SLWC[kg\ m^{-3}] = \rho_{air} \cdot CLWMR \quad (4)$$

$SLWC$ is the supercooled liquid water content [$kg \cdot m^{-3}$]; ρ_{air} is air density [$kg \cdot m^{-3}$] and $CLWMR$ is cloud liquid water mixing ratio [$kg \cdot kg^{-1}$].

The thickness rate \dot{h} that indicates the accumulated ice on a fixed cylinder is represented with Eq. (5).

$$\dot{h} = E \cdot SLWC \cdot U \cdot F / \rho_{ice} \quad (5)$$

ρ_{ice} which represents ice density is involved in quantifying icing thickness and was calculated using Laforte ice density empirical relation (Laforte et al., 1992) and F is the freezing fraction. For rime ice, all of the supercooled water collected freeze; but for glaze ice only a fraction of it freezes (Messinger, 1953; Mazin et al., 2001). The critical liquid water content known as the "Ludlam limit" is used to represent the boundary between wet and dry growth of ice. This limit will then be used to obtain the freezing fraction (Ludlam 1951, Mazin 2001).

The Mt Bélair test site is a well-appointed icing measurement station. An icing-rate meter (IRM) has been placed at the top of a tower close by 315 kV double-circuit and 735 kV transmission lines installed by Hydro-Quebec in 1994 (Savadjiev et al., 1999).

Compared to average monthly temperatures for winter months over a 32-year period, the variations in the percentage of temperatures that fall within a range of $[-1^{\circ}\text{C } 0^{\circ}\text{C}]$ over the Mt Bélair area at 2.5%, and over the Bagotville area at 3.5%. This temperature range corresponds to glaze ice, when the drops don't freeze completely.

1.2.3 Icing events

Insignificant icing events were excluded from our calculations because we prefer concentrate our efforts on cases that may involve risks. The monthly icing accumulation (in millimetres) corresponding to icing rates below $0.001\text{ mm}\cdot\text{hr}^{-1}$ was approximately 0.01%. This justified our exclusion of events that are characterized by icing rates lower than $0.001\text{ mm}\cdot\text{hr}^{-1}$.

Also, the duration of icing events and ice accretion were calculated separately for each month (December, January and February). Since the reanalysis timestamp duration is 3 hours, consequently the duration of icing events are in multiples of 3 hours.

Icing was calculated on each single NARR cell ($32\text{km} \times 32\text{km}$) using a coordinate (i,j) of a desired subset area within the NARR zone, based on a cylindrical object of 6.2 mm in diameter corresponding to the cylindrical Hydro-Quebec icing-rate meter (IRM). This method is used to measure icing events at the Mt Bélair and Bagotville sites

1.2.4 Freezing rain storm of 1998

The severe ice storm of 1998 was an unprecedented meteorological event in North America (DeGaetano, 2000). This event was located in an area between a warm cyclonic circulation to the south and a cold anticyclonic flow to the north. At the planetary-scale the circulation structure that generated the ice storm of 1998 has been repeated five times

during a 34-year period. The ice storm of 1998 was the only occurrence among the six that produced such remarkable amounts of freezing rain. When warm frontal air overrides a sub-freezing zone, it forms what is known as a “warm nose”, a layer of above-freezing air that allows melting solid precipitation. Subsequently, the resulting rain fall into the sub-freezing layer of air located between the 'warm nose' and the surface, will re-freeze to become supercooled rain (Carrière et al., 2000, Bernstein et al., 2000).

The January 1998 ice storm measurements were provided by Environment Canada. The freezing precipitation in the ice storm was primarily caused by ice crystals and snow which formed in the clouds in a sub-freezing layer. The ice crystals and snow fell and melted in a warm layer and then fell and supercooled in a lower cold layer and deposited on the surface. For this ice storm, the model re-analysis infers precipitation rate rather than cloud water. This was done in order to achieve a reliable comparison between measurements and calculations.

In this section, ice thickness was calculated using the same accretion model, involving supercooled liquid water content that was calculated from precipitation rate, closest wind speed from reanalysis to surface (at 10 meter) and temperature at surface level.

According to an experimental study (Mason, 1971; Best, 1950), the distribution of rain droplets diameter was obtained. Following a smoothing of experimental data, the study revealed a relationship between freezing rain precipitation rate, liquid water content, and medium volume diameter. Based on the results of Best (1950), the liquid water content was concluded indirectly using freezing rain precipitation rate from reanalysis.

Therefore, precipitation rate from reanalysis that covers the period of January 4th - 10th, 1998 was higher during January 5th, 8th and 6th respectively. These dates correspond to highest liquid water content 0.084, 0.083 and 0.034 $\text{g}\cdot\text{m}^{-3}$ as shown in Figure 2. During this ice storm, Figure 3 shows that January 5th and 8th hold the highest freezing rain droplet diameter of approximately 1.45 mm.

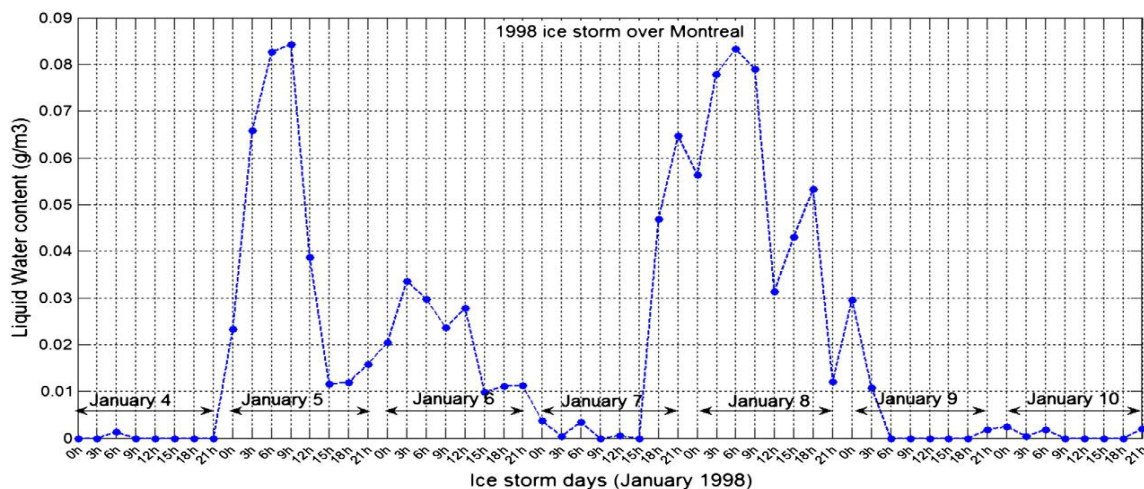


Figure 1.2. Liquid water content calculated using precipitation rate from reanalysis that covers the period January 04th until January 10th.

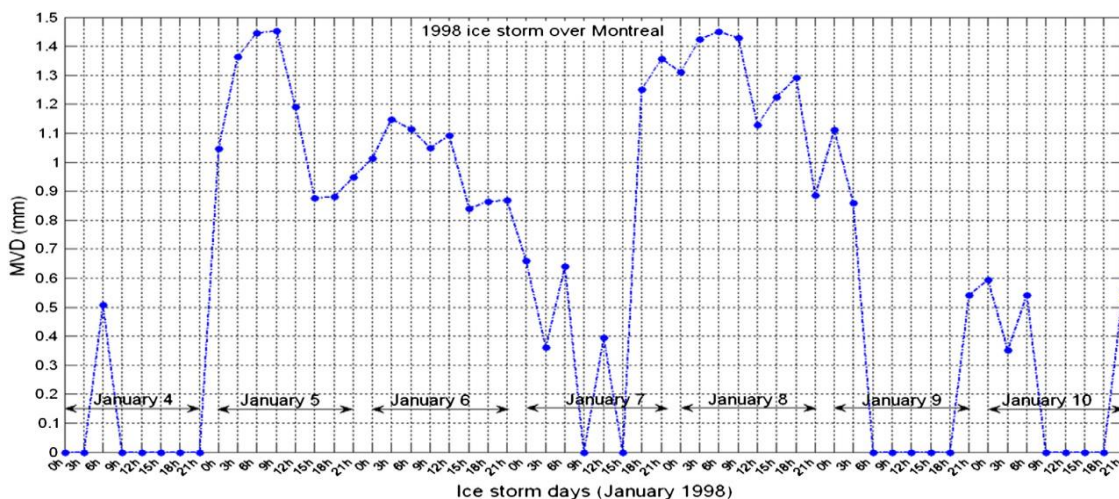


Figure 1.3. Median volume diameter calculated using precipitation rate from reanalysis that covers the period January 04th until January 10th.

1.2.5 Icing severity index

An icing severity index (ISI) was introduced in order to better represent the potential dangers of icing events. Accumulated icing alone cannot be viewed as representative of the different levels of icing severity and icing risk. This study introduces a new type of severity index. Fortin et al. (2005) have confirmed that the severity of icing events depends not only on icing accumulation rates, but also on the duration of these events. Furthermore, Makkonen (1984) has demonstrated that the duration of an ice storm becomes an important factor influencing mean ice growth rate.

Different levels of icing severity were presented in Table 1.1. An in-situ study (Fortin et al., 2005) was carried out at a site in Murdochville (Quebec-Canada) to investigate atmospheric icing effects on wind turbines; the average duration of an icing event was found to be about six hours. NARR reanalysis data became available every three hours, and a six-hour icing event might last long enough to obtain NARR data twice. Newton (1978) has already classified the potential accumulation on four different classes. During the current study, five different icing-event classes (trace, light, moderate, severe and extreme) were created, based on the different ranges of icing rates. Since liquid water content is proportional to icing rate, a weighting called LWC weight was given to each class that was determined by a range of icing rate. A weighting reference equal 1 was appointed to class Moderate, for light and trace classes LWC weighting decreases and it increases for severe and extreme classes (Table 1.1). The thresholds that distinguish the five classes were based on the icing thickness accumulated compared to the cylinder diameter of the icing rate meter.

Table 1.1 : Severity classes

Class	Lower limit	Icing rate (mm·hr ⁻¹)	Higher limit	Accumulation of ice over 6 hours (mm)	LWC weight
Trace	0.001	$< \dot{M} \leq$	0.5	3	0.1
Light	0.5	$< \dot{M} \leq$	1.0	6	0.5
Moderate	1.0	$< \dot{M} \leq$	2.6	16	1
Severe	2.6	$< \dot{M} \leq$	5.1	30	1.5
Extreme	5.1	$< \dot{M}$		>30	2

Supercooled liquid water content and thickness of icing accumulation illustrated in Table 1.1 are factors that influence severity level.

Consequently, several different weighting factors were considered in this study, in order to provide an accurate evaluation of the level of icing severity. Liquid water content weighting, event duration weighting and icing classes were included in the severity risk assessment. In this study, only the winter months (January, February and March) were taken into account over 32-year period (1979 to 2010). Atmospheric icing was quantified for each week from 1979 through to 2010. Three weighting factors were applied in order to accentuate icing index levels.

The monthly icing index that involved the effect of three weighting factors is shown in Eq. (6) as SW.

$$SW = \sum_i^{classes} Wt_i \cdot WL_i \cdot h_i \quad (6)$$

h_i is the monthly icing accumulation for each class, and it includes class weightings; Wt_i is the weighting for icing-event duration, while WL_i is the liquid water content (LWC) weighting for each class (Table 1.1).

Weighting for icing-event duration was calculated by applying Eq. (7), because NARR data was available every three hours, while a typical icing event lasts six hours, or

two time steps from NARR data. Icing events lasting six hours are considered as references, each generating a neutral weighting of 1. In events lasting longer than six hours, Wt increases gradually, while for events that shorter than six hours, Wt decreases.

$$Wt = 1 + \left(\frac{i-2}{10}\right) \quad (7)$$

$i = \frac{Nb_{hours}}{3}$, Nb_{hours} : indicates the duration of icing events, in hours.

Eq. (8) illustrates the icing severity index (ISI) over each NARR cell (32km by 32 km) which is the average of the monthly icing index as shown in Eq. (6), covering a 32-year period.

$$ISI = \frac{\sum_{j=1}^N SW_j}{N} \quad (8)$$

$N=32$ months (32 years)

1.3 Results

The whole NARR zone is represented by 349 x 277 cells. From a NARR-data topographical point of view, Figure 1.4 illustrates a portion of one cross-sectional area representing an approximately South-North profile of elevations above sea level. In order to identify the Mt Bélair elevation using NARR, the cross section was located at a fixed NARR X-coordinate (X=254) and at an interval of Y-coordinates that includes the Mt Bélair site (X=254, Y=151). The Mt Bélair site is located within a NARR cell that has an elevation of 112 metres above sea level (Figure 1.4). This elevation is underestimated when compared to its real value of 480 meters, due to the small horizontal area occupied by Mt Bélair (less than 5 km). Also, as illustrated in Figure 4, just northward of Mt Bélair's

NARR cell ($Y \geq 152$), the elevation of NARR terrain rises sharply to 480 meters, due to the presence of the Laurentian Plateau.

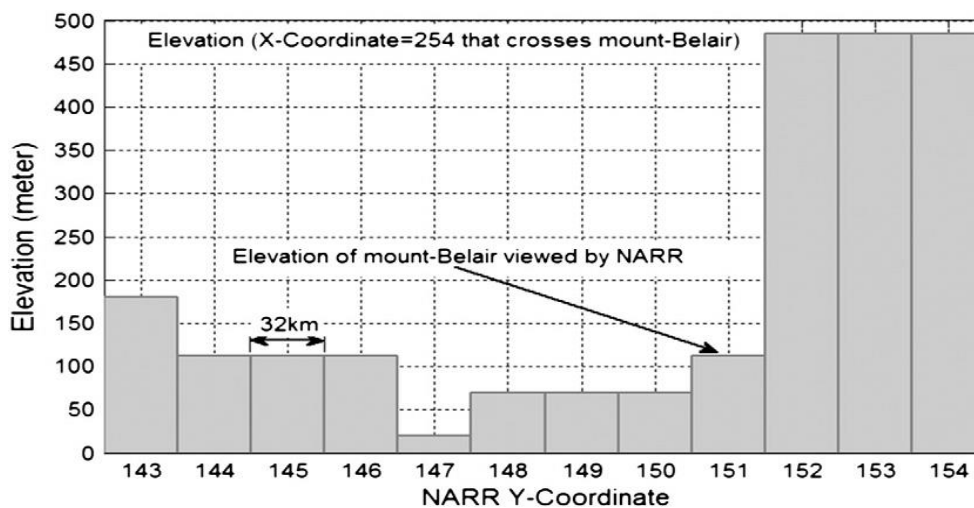


Figure 1.4. Cross-section of NARR topography.

1.3.1 Case studies

Since icing climatology is the purpose of this study and due to the limitation of in-cloud icing measurements, a monthly comparison of icing accumulation and duration of icing events has been presented.

Icing was calculated for each time step with the use of reanalysis over both Bagotville and Mt Bélair sites. In addition, Table 1.2 shows values of the key variables and parameters that were extracted from reanalysis, only during icing events that characterized the two sites of case studies during November, December 1998, January, February and March 1999. Furthermore, Table 1.2 shows the maximum and the average of supercooled liquid water content and wind speed, the minimum and the average of air temperature that characterize both sites during each month. The monthly averages of collection efficiency shown in Table 1.2 indicate a range of values between 0.26 and 0.48. In addition, results

from Table 1.2 indicate that the Mt Bélair site had higher supercooled liquid water content during all five months, compared to the Bagotville site. A maximum liquid water content of $0.41 \text{ g}\cdot\text{m}^{-3}$ was recorded at the Mt Bélair site during January 1999, followed by $0.21 \text{ g}\cdot\text{m}^{-3}$ for March 1999, $0.18 \text{ g}\cdot\text{m}^{-3}$ for December 1999, $0.13 \text{ g}\cdot\text{m}^{-3}$ for February 1999 and the lowest of $0.04 \text{ g}\cdot\text{m}^{-3}$ during November 1999. Contrary to Mt Bélair, reanalysis revealed that the Bagotville site captured icing events with a much smaller values of liquid water content $\sim 0.01 \text{ g}\cdot\text{m}^{-3}$.

According to Table 1.2, the Bagotville site had no icing events during November and December 1998. On average, the Bagotville site experienced the coldest weather with the lowest air temperature. During the icing months shown in Table 1.2, Bagotville had an average wind speed of $3.7 \text{ m}\cdot\text{s}^{-1}$ which is slightly higher than the average wind speed of approximately $2.9 \text{ m}\cdot\text{s}^{-1}$ over Mt Bélair.

Table 1.2 : Monthly key variable in the two sites

	Mt Bélair					Bagotville				
	Nov98	Dec98	Jan99	Feb99	Mar99	Nov98	Dec98	Jan99	Feb99	Mar99
SLWC_{Max} (g/m³)	0.04	0.18	0.41	0.13	0.21	no ice	no ice	0.01	0.015	0.006
SLWC_{Mean} (g/m³)	0.02	0.05	0.12	0.045	0.05	no ice	no ice	0.006	0.007	0.003
Wind_{Max} (m/s)	4.2	6	7.9	5.9	6.1	no ice	no ice	6.2	6.1	5.6
Wind_{Mean} (m/s)	2.2	2.7	4.1	3.1	2.6	no ice	no ice	3.3	3.5	4.4
T_{Min} (°C)	-4.4	-26	-23	-18.5	-14.9	no ice	no ice	-32	-28	-22.8
T_{Mean} (°C)	-2.6	-5.5	-12.4	-8	-5.7	no ice	no ice	-19.7	-10	-21
E	0.26	0.32	0.45	0.37	0.32	no ice	no ice	0.40	0.41	0.48

The difference in diameter between the Hydro-Quebec icing-rate meter and Hydro-Quebec's electrical cables yielded different results in collection efficiency values. Under the same meteorological conditions, icing accumulation thickness on Hydro-Quebec electrical cables are about 20% lower than icing accumulation on the icing-rate meters. In these case

studies, due to the limitations of available reanalysis variables, icing was calculated at 1000 mb.

The results presented in Figures 1.5 and 1.6 correspond to a comparison between model-based calculation and measurements of monthly icing accumulation and duration of events, on both sites: Mt Bélair and Bagotville. Moreover, Figures 1.5-a, 1.6-a, 1.5-b and 1.6-b illustrate the fluctuation of the monthly duration of events and ice accumulation during November and December 1998 as well as January, February and March 1999. Basically, one notices that icing accumulation on Mt Bélair was consistently much larger than the icing accumulation on Bagotville. These results confirm that complex terrain sites are exposed to higher icing accumulation than simple sites. Model-based calculations of icing accumulation were smaller than the measurements. This can be explained by the underestimation of cloud water that characterizes the microphysics scheme used with reanalysis.

Regarding the Bagotville site, Figure 1.5-a demonstrates that the model was able to detect the presence and the absence of icing events. The detection of icing events revealed differences between measurement and calculation of 0 day, 0.1 day, 0.1 day, 0.15 and 0.2 day during November and December 1998 and in January, February and March 1999 respectively. The quantification of icing accumulation shown in Figure 1.5-b was well predicted, except in December 1998 and in February 1999. The differences of icing accumulation between measurement and calculation were 0 mm, 0.1 mm, 0 mm, 0.3 mm and 0 mm for November and December 1998 and for January, February and March 1999 respectively. The curves of tendency that are represented in Figures 1.5-c and 1.5-d

characterize the comparison between model-based calculations and measurements. Regarding all five months, the comparison shows a high correlation between the calculations and measurements with a slope of 0.91 for the duration of events and 0.90 for the accumulation of icing.

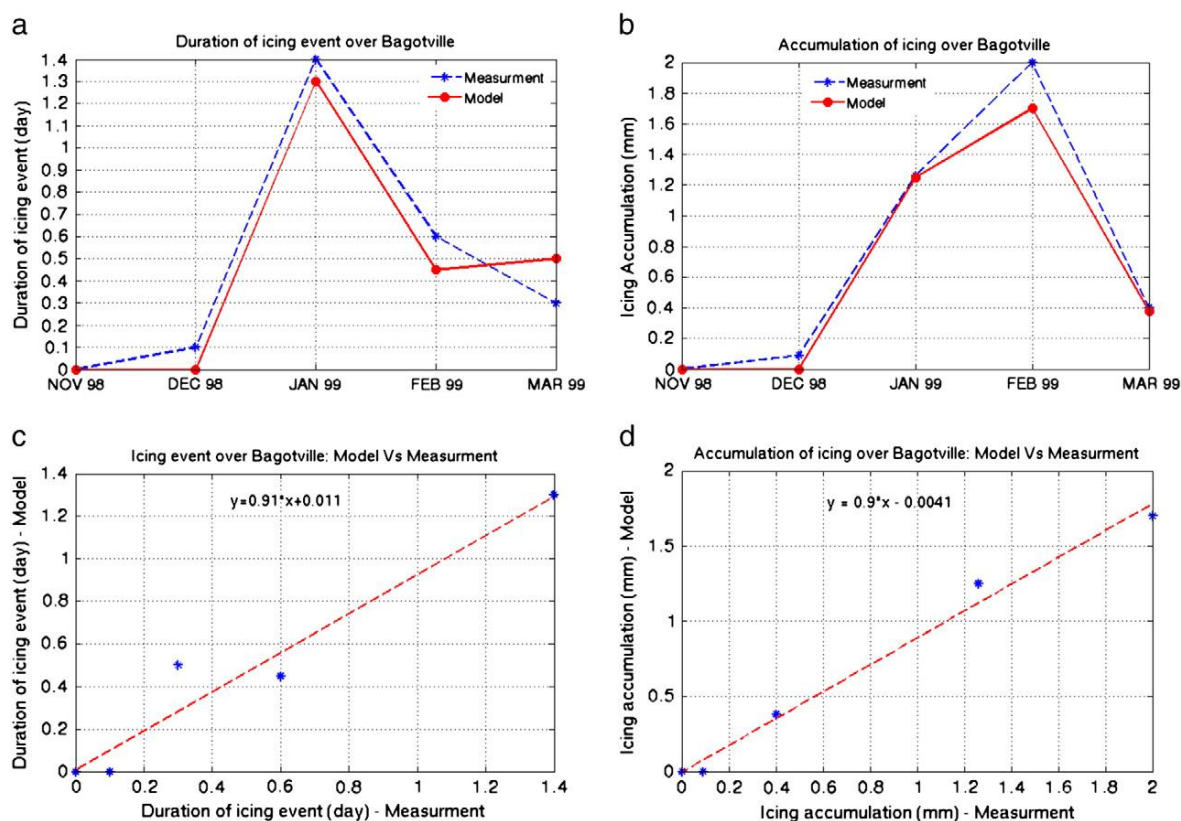


Figure 1.5. Monthly model-based calculation and measurements on Bagotville;
 (a) duration of icing events (b) accumulation of ice
 (c) duration of event-model vs observation (d) accumulation-model vs observation.

According to the results shown in Figure 1.6, the Mt Bélair site reveals an underestimation for the entire five months. The difference between the model and the measurements for the duration of icing events is demonstrated in Figure 1.6-a. They were

0.4 day, 0.57 day, 0.4 day 0.8 day and 0.2 day during November and December 1998, and during January, February and March 1999 respectively. Both icing accumulations obtained from model and measurements are shown in Figure 1.6-b. The differences between measurements and calculations of icing accumulation were 75 mm, 16 mm, 5 mm, 12 mm and 67 mm during November and December 1998 and during January, February and March 1999 respectively. On the other hand, during the winter months a better correlation between the model and measurements is manifested in Figure 1.6-b with results that indicate a difference of 16 mm for December 1998, 5mm for January 1999 and 12 mm for February 1999. The accumulation of icing represented in Figure 1.6b shows an underestimation of the model-based thickness of icing accumulation over Mt Bélair. On the other hand, no tendency between the calculations and the measurements for the duration of icing event is shown at Figure 1.6a. The underestimation of cloud water from reanalysis, thereafter contributes to the underestimation of model-based icing accumulation. During November (Fall 1998) and March (Spring 1999), the simulation underestimated largely the amount of icing accumulation that was measured over Mt Bélair. Since the calculation was based on meteorological variables from reanalysis at 1000 mb level that correspond only to subfreezing temperatures, and Mt Bélair represents a complex terrain with elevated topography, it is conceivable that the model wasn't able to precisely capture the icing during November 1998 and March 1999, when the air temperature is slightly above freezing point. The Mt Bélair elevation viewed by reanalysis is 112 meters which is underestimated compared to the real elevation of 480 meters. Considering the vertical

variation of the temperature in the atmosphere, a difference of a few hundred meters in elevation can generate a difference in the air temperature by more than few degrees Celsius.

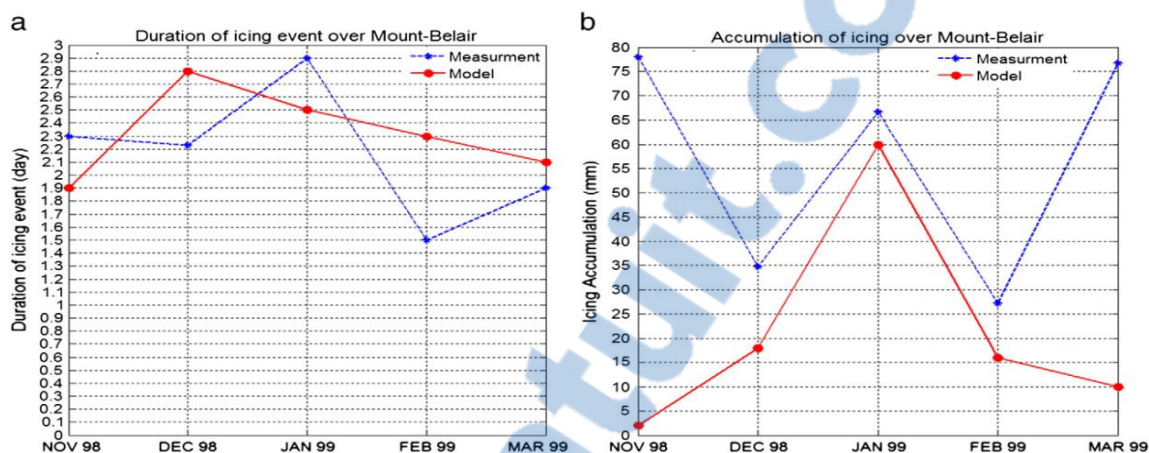


Figure 1.6. Monthly model-based calculation and measurements on Mt Bélair; (a) duration of icing events (b) accumulation of ice.

The climatology of both the duration of icing events and ice accumulation that span a 32-year period for the month of January, over Bagotville is represented in Figure 1.7. This Figure also shows that the model-based calculation generated icing events only from a trace class of icing events (Table 1.1). The longest event occurred in January 1984 which lasted for 2.25 days. The highest amount of icing accumulation of 2.25 mm took place in January 1982. Durations of the icing events that occurred over Bagotville during the 32 year period, average approximately half a day.

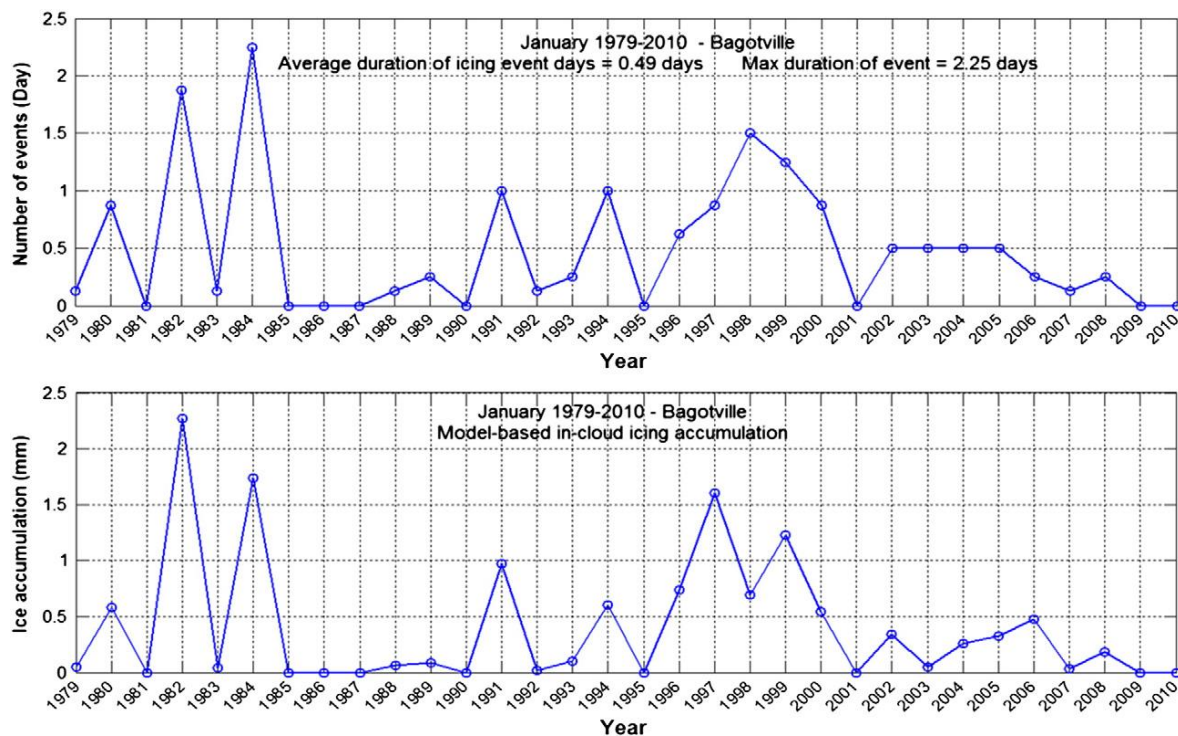


Figure 1.7. Climatology of model-based in-cloud icing events, duration and accumulation over Bagotville in January for 32 years.

The calculation of the duration of icing events from reanalysis and the various icing event classes at Mount Bélair are displayed in Figure 1.8. These events occurred at 1000 mb over the 32-year time period. Mount Bélair experienced icing events that averaged 3.25 days in duration, with a maximum duration of 6.75 days. Icing events were classified as follows: 62.02% trace events, 17.67% light events, 16.12% moderate events, 3.49% severe events and 0.72% extreme events. Also, January 2006 saw the longest duration of extreme events (in red circles) of the 32 years covered by the graph. According to Figure 1.8, January 1998, 2003 and 2010 demonstrated a persistence of icing events that exceeded 6 days. The duration of icing events over this complex terrain site were above average for 13 years within the 32 years that were analysed. The 13 years in which this occurred in the

month of January were 1980, 1981, 1988, 1997, 1998, 2000, 2001, 2003, 2004, 2006, 2007, 2008 and 2010. Overall, trace class represents the majority of severity classes, followed by light, moderate, severe and finally extreme classes (Table 1.1). January 1997 and January 1999 were characterized with the longest duration of severe class events which lasted a half day.

The duration of icing events over Mont-Bélair site shown in Figure 1.8 confirmed that extreme events were less frequent during January, with two isolated occurrences in the course of 1998 and 2006. It also demonstrates that more severe the icing event, the shorter the duration of the event.

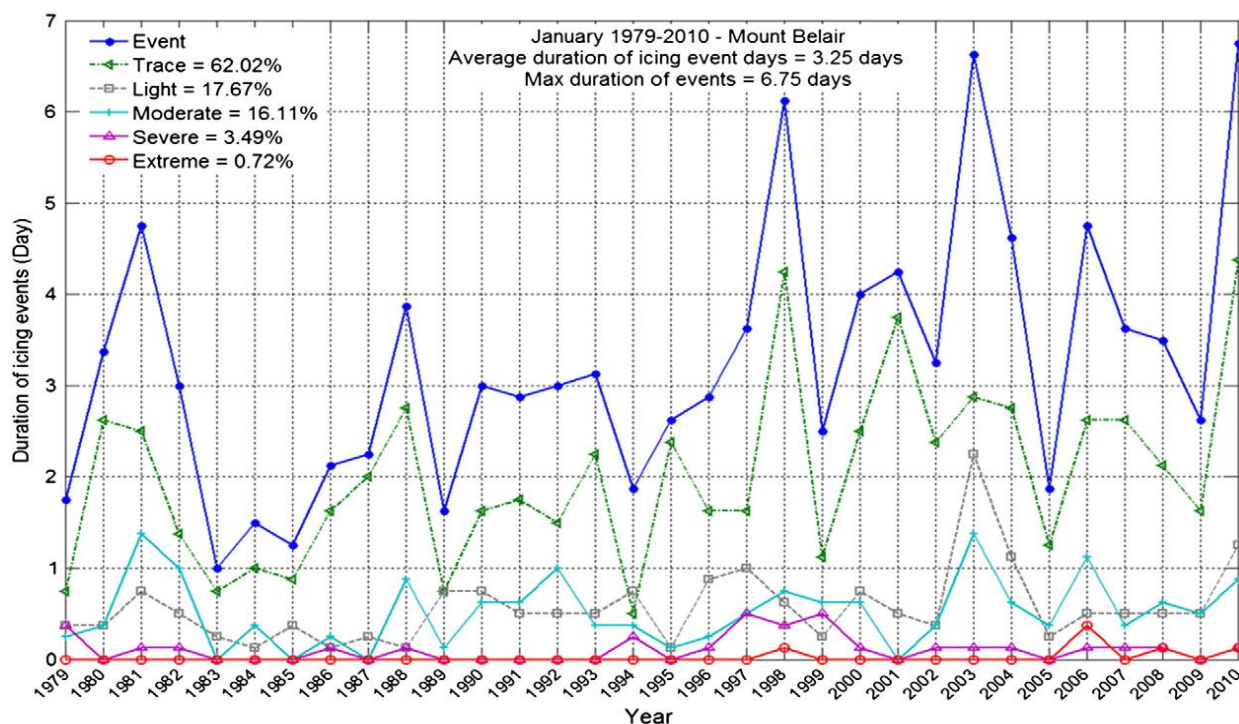


Figure 1.8. Model-based monthly duration of icing events in January for 32 years at Mount Bélair (Quebec, Canada).

For both sites, model-based ice accumulation and icing severity index are represented in Figure 1.9 and 1.10, in order to illustrate how icing severity index varies

during 32-year period compared to ice accumulation. As shown in Figure 1.9, Bagotville which represents a simple topography site was identified as a low icing risk site with a very small 32-year average icing severity index of 0.07. Icing calculations from reanalysis over Bagotville shown in Figure 1.9 confirmed that January 1982 followed by January 1984 experienced the highest ice accumulation and icing severity index within very low values overall. Unlike Bagotville, Figure 1.10 reports that the complex terrain of the Mt Bélair site holds a high potential of icing risk with a 32-year average icing severity index of 16.3. Throughout a 32-year period, as shown in Figures 8 and 10, January 1999 and January 2006 were associated with the most severe and extreme icing events respectively. Despite the fact that January 2006 had a higher ice accumulation than January 1999, both months were identified with the same icing severity index. January 2006 had more ice accumulation but a shorter duration of extreme icing events compared to January 1999. The month of January during the years; 1981, 1990, 1997, 1998, 1999, 2003, 2004, 2006, 2008 and 2010 indicated values of icing severity index that were above average and distinctive of the Mt Bélair site. Furthermore, according to Figure 10, in January 1997, the Mt Bélair site was characterized by higher risk icing events than ever before. On the contrary, in January 1983 and 1985 there was ice accumulation as low as 5 mm in 32 years over Mount-Bélair. Although this ice accumulation is considered quite low for Mt Bélair, it is still larger than the highest amount of ice accumulation during January in Bagotville during a 32-year time period.

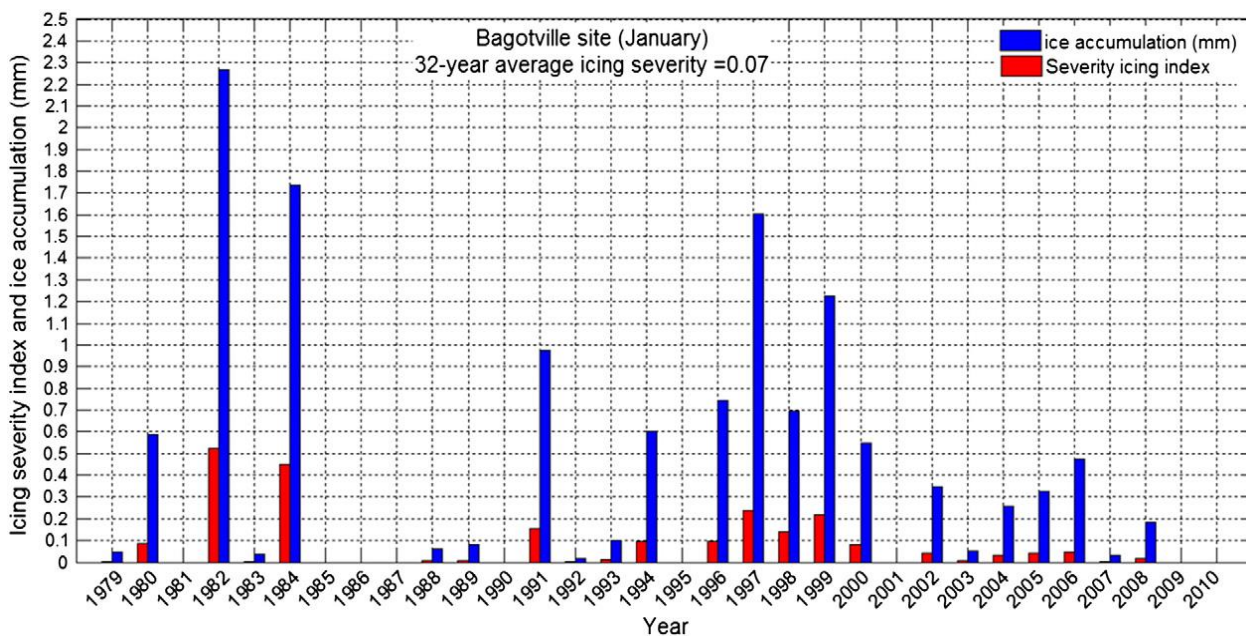


Figure 1.9. Monthly model-based severity and ice accumulation on Bagotville during January of each year - 32 years.

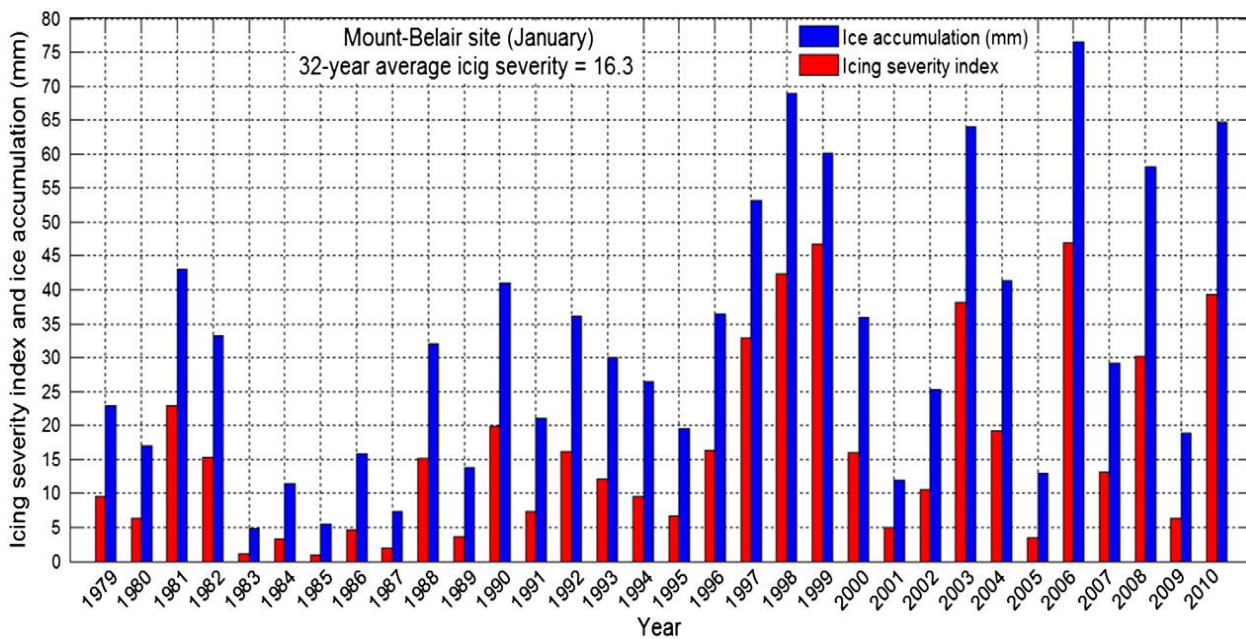


Figure 1.10. Monthly model-based severity and ice accumulation on Mt Bélair during January of each year - 32 years.

1.3.2 Ice storm of January 1998

The Monteregie ice storm of 1998 is investigated separately, with the use of the icing model developed herein. Ice accumulation is calculated with the same ice accretion model that is used for in-cloud icing calculations over Mt Bélair and Bagotville. Regarding in-cloud icing, the only variable factor related to airborne water being expressed as a cloud water mixing ratio. The cloud water originated directly from reanalysis at 1000 mb level. Differently in this section, the liquid water content used for the 1998 ice storm is deduced from the precipitation rate of freezing rain available from NARR data. In addition, the temperature and wind speed at 10 meters were extracted from reanalysis to calculate ice accretion.

The spatial distribution of the icing accumulation observed during the period of January 4 to 10, 1998 shown in Figure 1.11(b) (Environment Canada, 1998), corresponds to the historic ice storm event that occurred over the province of Quebec in the Montérégie, the Eastern Townships regions, and northern New York State, USA. Covering the same time period, Figure 1.11(a) shows a model-based icing accumulation generated using the following meteorological variables from reanalysis: precipitation rate, air temperature at surface level and wind speed at 10 meters level. Calculations for Figure 1.11(a) were performed within a zone of 20x20 NARR Cell, i.e. a $(640 \text{ km})^2$ area.

Moreover, the greatest amount of icing accumulation, based on observations over the Island of Montreal, shows a value between 40 mm and 60 mm of icing (Figure 11b) and approximately between 60 mm and 70 mm from the calculations. The distribution of icing accumulation shown in Figure 1.11 corresponds to the severe icing event, which took place

in Montreal in January 1998, causing substantial ice accumulation within six days long. Both maps in Figure 1.11 illustrate approximately the same position regarding the core of the ice storm, which reached a maximum accumulation of 133 mm based on calculations from reanalysis, and 100 mm based on measurements, with a relative error of 33%. In regard to the ice storm, the comparison that revealed an overestimation of ice accumulation generated from reanalysis was based on wind speed from reanalysis at level 10 m above ground level. Eq. (1) revealed that ice accretion is proportional to the moisture flux $LWC \cdot U$. Liquid water content and wind speed vary strongly near ground level. Since wind speed follows the power law that represents its vertical profile that varies according to z^α (Manwell, 2010), z : represents the elevation above the ground while $\alpha \approx 1/7$, therefore, the wind speed can be adjusted at 1 m above the ground. Consequently, the relative errors of ice accumulation can be minimized to approximately 3%. On the other hand, the fact that the vertical variation of liquid water content is unknown poses a challenge on adjusting liquid water content at different elevations.

Both the model and observations of the 1998 ice storm from Figure 1.11 display a large gradient between Montreal and Ottawa. Figure 1.11-a and 1.11-b also show how the line of maximum icing spreads from the south of Montreal (Montérégie region) to the south of Brockville, Ontario. Figure 1.11-a extends the peak line further reaching south of Kingston and east of lake Ontario. The Mt Tremblant National Park and its surrounding area located northeast of Montreal is represented in Figure 1.11-a with high icing accumulation. Measurements from Figure 1.11-b show an absence of icing over this area

during the 1998 ice storm. In this zone, the difference between measurement and calculation is due to the very complex, mountainous and irregular topography.

Figures 1.2 and 1.3 presented before that show the liquid water content and median volume diameter extracted from NARR over the region of Montreal corroborate the fact that the precipitation was the highest during 5-6 and 8-9 January 1998. In addition, Figures 11a and 11b display a pattern of an elongated peak of precipitation during this ice storm. This pattern reflects the mesoscale details like frontal structure and the orography of the Saint Lawrence River valley that controlled the area and the intensity of freezing precipitation.

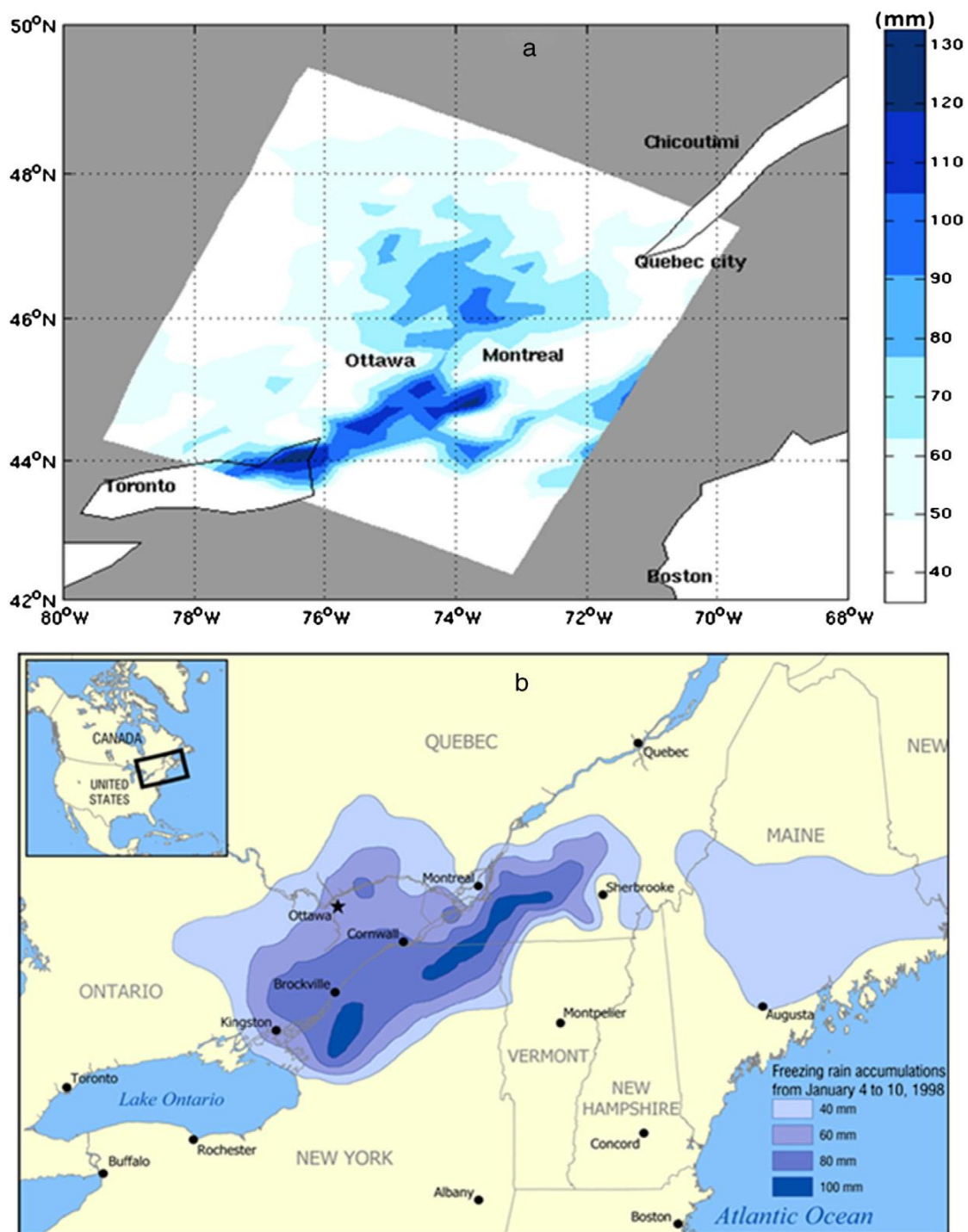


Figure 1.11. Icing accumulation from January 4 to 10, 1998 over the southwestern region of Quebec (Canada) (a) ice accumulation calculated using NARR reanalysis (b) measurements (courtesy of Environment Canada).

1.3.3 Icing severity index

Despite the fact that icing is still a threat in the area of the study during November 1998 and March 1999, the inadequate correlation over the complex terrain (Mount Bélair) between measurements and model-based calculations during these two months limited the choice of mapping to winter months only (December, January and February). The real elevation of 480 meters that defines the Mt Bélair site is underestimated by reanalysis that represents it with an elevation of 112 meters. In this region at level 1000 mb, March and November are characterized with air temperatures that are around freezing point. When air temperature is around freezing point at 1000 mb, this implies that at a few hundred meters above this level, the air temperature is likely at subfreezing range. Knowing that the model captures icing events only at subfreezing temperatures, in order to reduce air temperature errors due to the topography, it was convenient to choose winter months that are characterized mostly with subfreezing air temperatures in the region of the study.

The icing severity index shown in Figures 1.12, 1.13 and 1.14 was obtained from Eq. (8) and it covers a 17 x 20 NARR cell zone. Each cell covers approximately 32 km by 32 km; the implication is that the icing severity index calculation zone is 544 km by 640 km at the 1000 mb level.

All Figures of icing severity index reveal that most severe icing events at the surface, tends to occur offshore. The offshore zone around the Gaspé Peninsula holds the highest wind speeds in the entire region. Since ice accretion is proportional to liquid water content and wind speed, in presence of moisture, it is reasonable that the most severe icing occurs over this specific zone.

Icing index maps also indicate that most of onshore severe icing events occurred in areas located in the west of Moncton (New Brunswick). The map in Figure 1.12 shows an icing severity index for January revealing noticeably severe icing over the Moncton area with a severity index between 70 and 80, followed by Quebec City and its surrounding areas (including the Mt Bélair area) with a severity index between 50 and 60; and then the eastern part of the Gaspé region; Cap-chat, Matane, and greater Rimouski until Riviere-du-loup with a severity index of around 30.

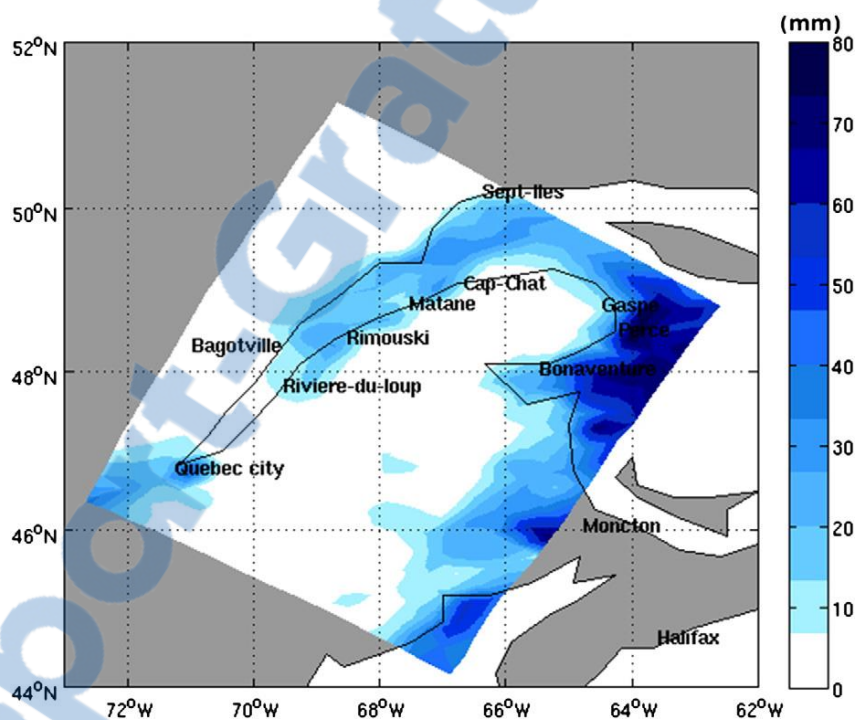


Figure 1.12 : Icing severity index map - January 1979–2010.

Regarding February, the icing severity index map in Figure 1.13 shows that the severity level was the lowest over onshore areas and the highest over offshore area north of the St Lawrence valley. During this month exceptionally, Sept-Îles area was characterized

with the most significant icing severity index of approximately 40, compared to a values between 20 and 30 during January. On the other hand, during this month, the lack of moisture flow towards the east and the south (Mt Bélair) of the St Lawrence valley significantly reduced the icing severity index to 18 and 30 respectively.

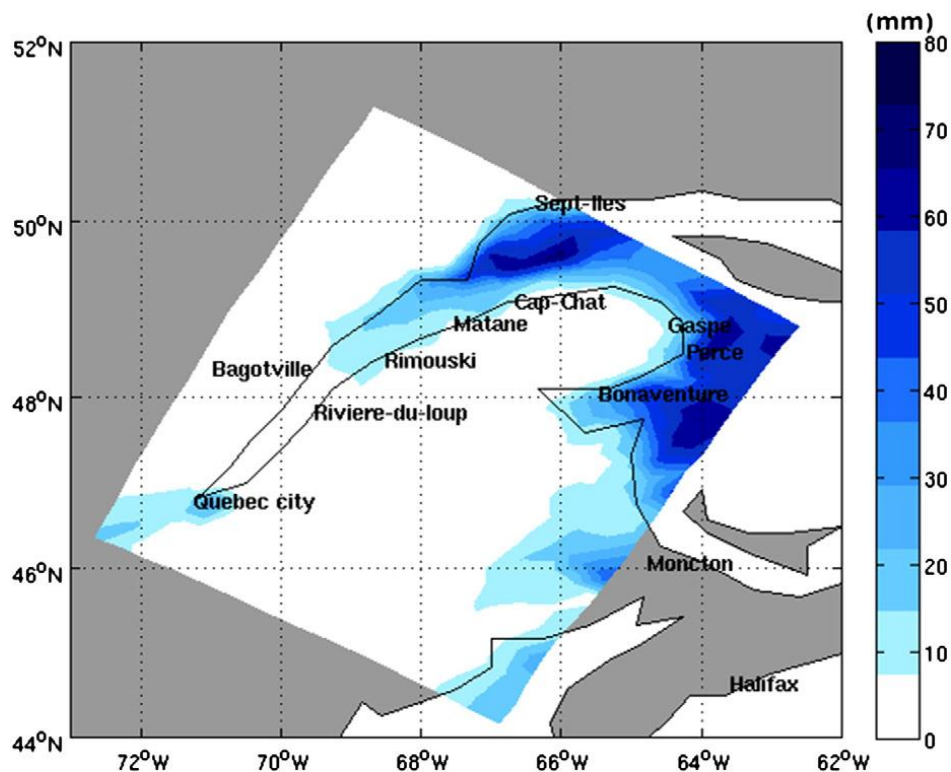


Figure 1.13. Icing severity index map - February 1979–2010.

The icing severity index in Figure 1.14 shows, in addition to the Moncton area, the icing severity index in December over Quebec City was less intense than January with a value equal to 30. Alongside this, the index varied from 20 to 30 in Rimouski continuing south through the nearby cities including Rivière-du-loup. In the Gaspé region, Matane was the most affected area where the icing severity index was at an approximate value of 18. The coastal areas of the Gaspé Peninsula were also affected to a lesser degree. During

December, the Moncton area was associated with an index of 50 which is less severe than January and more severe than February.

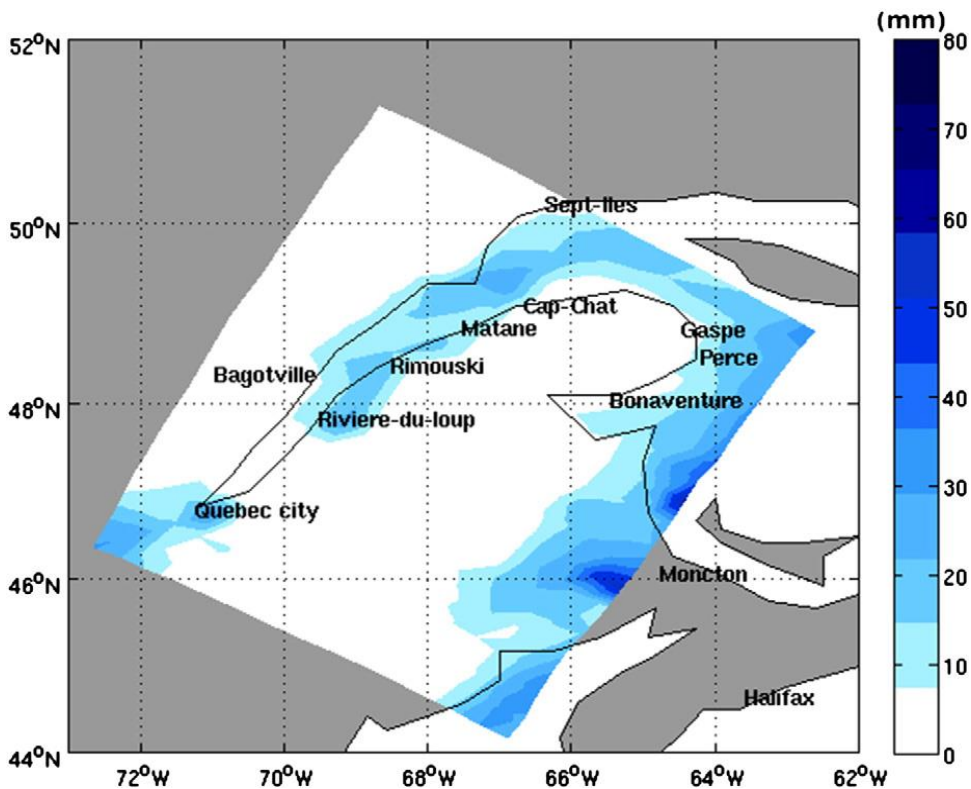


Figure 1.14. Icing severity index map - December 1979–2010.

An obvious and consistent icing pattern can be seen surrounding the Gaspé Peninsula, covering coastal areas.

In observing Figures 1.12 through 1.14, the icing severity index for three individual months reveals that the most severe icing events over Matane, Quebec City, Mt Bélair and the Gaspé area occurred in January. December resulted in slightly less intense conditions, except in the zone between Rimouski and Rivière-du-loup which is the highest icing severity index during December, while February recorded the weakest over this area. An



average of the icing severity index for 32 years during December, January and February is shown in Figure 1.15. For the Sept-Iles area, the month of February had maintained the highest icing severity index.

The icing severity index represented in Figures 1.12, 1.13, 1.14 and 1.15 indicates that the northeastern part of the Gaspé Peninsula, followed by the Quebec City area, Mont-Joli, Rimouski and neighbouring areas to the south near the city of Rivière-du-loup, are at the greatest risk for icing in this entire region. Mapping the three-month average (in Figure 1.15) also provided a clear view of consistently intense icing over the Gaspé region, specifically in coastal areas, with particularly strong icing severity over the lower St Lawrence River areas. Except for coastal areas, the geography of the Gaspé region mainly contains complex terrains with high altitudes of up to 1200 meters. The maps in Figures (1.12, 1.13, 1.14, and 15) showed that cities along the coast like Cap-chat, Matane, Sept-Iles and Rimouski until Rivière-du-loup are exposed to higher icing risks compared to other onshore locations. These areas are located between hilly topographies that are on both sides of the Saint Lawrence River valley. This scenario therefore increases the channeling of the wind and moisture towards the northeast or southwest direction. Due to its location, the Quebec City area including the Mt Bélair site is exposed to high coastal convergence that is initiated by wind funneling which generally causes a significant increase of wind speed. Once this moist flow of air is below freezing temperature, supercooled fog or the stratus clouds that form in turn will generate in-cloud icing upon contact on an object. In addition, the location of the Saguenay River, north of Bagotville which joins the St Lawrence River,

enhances the funneling out of the moisture flow from the Saguenay River towards Rimouski and its surroundings.

The icing peak across eastern Canada is commonly related to the synoptic-scale forcing that is prone to cloud formation. In the Maritimes and the Gaspé regions, the pronounced gradient in icing severity is associated with storm tracks, low pressure centers and their interaction with landmasses that direct the transfer of moisture into these regions.

Furthermore, the Gaspé Peninsula and the lower St. Lawrence River region, during the winter season in general, ice storms are more frequent and severe accompanied with a strong wind coming from the west and northwest direction. The results of this study also corroborates the fact that the highest potential of icing events was found over eastern Canada, specifically the offshore zone in the Atlantic and Maritimes region, followed by the eastern parts of Gaspé Peninsula and then the lower St. Lawrence River. In addition, a large potential of icing is located over the Moncton area in New Brunswick.

The results of Figures (12, 13 and 14) that represent the mapping of the icing severity index show a more significant icing severity index over the Mt Bélair region during January followed by December and then February. As well, Figure (6-b) confirms that the monthly ice accumulation during January 1999 is the highest, followed by accumulation in December 1998 which is slightly larger than the ice accumulation in February.

Based on observation from Figure 5 and the mapping of model-based icing severity index in Figures 12, 13, 14 and 15, the simple terrain site of Bagotville which was used as a case study has a very low icing risk potential.

The city of Murdochville located in the Gaspé Peninsula is exposed to intense and frequent icing events during winter. On the other hand, Figures 12, 13, 14 and 15 display Murdochville with a low icing severity index. This discrepancy is due to the fact that Murdochville is located in a very complex and hilly terrain surrounded by mountains with elevations over 800 m, within a small horizontal area of approximately 1 km². Therefore, the coarse resolution of NARR which is 32 km, prevents the detection of the variations of the meteorological conditions at lower scale.

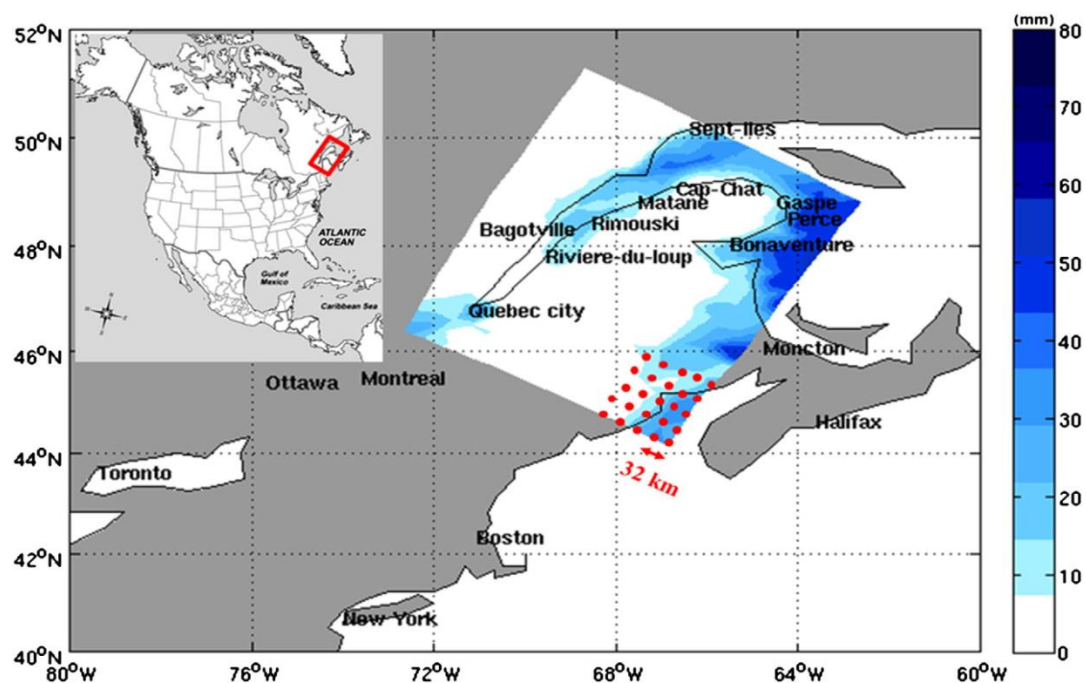


Figure 1.15. Icing severity index map — 3 month's average 1979–2010.

1.4 Discussion of the results

This study has provided a statistical analysis through the use of NARR data, involving the longest model-based climate investigation of ground level in-cloud icing done to date with a focus on only the winter months (January, February and December) that spanned a 32 year period.

The ways of estimating the severity of icing can differ based on the targeted field of application and the available data. Many of the previous studies that have attempted to explore the potential risk of icing events were applied exclusively for forecasting aircraft icing. The classification of different severity ranges was based on the level of necessity for de-icing in order to control icing hazards. Climatological estimates are used mainly for planning and design purposes, but can also substitute a specific forecast for areas without data.

The icing severity index suggested in this study assesses the icing severity near ground level with involving long time period data at climate scale, weighting based on critical parameters and relevant to larger applications not only Aircraft.

A climate investigation from reanalysis of Bagotville and Mt Bélair, conducted during the months of January over a 32-year time period, yielded an average duration of icing events of 3.25 days for Mt Bélair and approximately a half day for Bagotville.

In order to investigate ice accumulation over complex terrain (the Mt Bélair site), and simple terrain (Bagotville), icing was calculated at 1000 mb level. In this study, a cylinder model is used in order to obtain a reliable comparison that respects the measurement conditions. The results obtained from the comparison between measurement

and simulation indicated that the calculated ice accumulation has been underestimated at both sites. Calculated ice accumulation over both sites at 1000 mb showed a consistent pattern of icing events during winter months. In November and March, the comparison between the measurements and the calculations of the icing events at the Mt Bélair site revealed a clear discrepancy, caused by the coarse resolution of the cloud water from reanalysis which is insufficient to resolve that isolated and elevated site.

Complex terrain due to mountainous or land/water discontinuities, has a significant effect on meteorological conditions, unlike simple sites represented by flatland regions. This was evident in ice accumulation results over Mt Bélair. Therefore, the inconsistencies that arose while comparing measurements with icing calculations from reanalysis over mountainous areas such as Mt Bélair confirm the need for high-resolution meteorological data in order to quantify icing more accurately.

The icing and its severity level (duration of event, ice accumulation and icing severity index) were estimated and calculated for each NARR cell (32km)² in the region of study. Five classes of severity (trace, light, moderate, severe and extreme) were created, based on five ranges of the ice accumulation rate. The icing severity index is based on parameters that affect icing risk levels. These parameters include ice accumulation, duration of icing events, liquid water content and the classes of icing severity. A monthly icing severity index was introduced in order to quantify the icing severity index for each year.

With regard to the 1998 ice storm over southeastern Canada, a comparison between the measurements and the calculations of ice accumulation produced promising results and

demonstrates that our method can be extended to cover both in-cloud and freezing rain icing conditions. This revealed a relative error of 33% with regard to the maximum ice accumulation from measurement and calculation over the entire zone. The difference in ice accumulation between measurement and calculation varied from 10mm to 20 mm over the island of Montreal.

The challenges encountered with the use of reanalysis data for mapping and icing calculations were due to the lack of measurements available for comparison, as well as the coarse resolution of reanalysis.

In this study, the cloud water extracted from reanalysis proved to be an essential variable for quantifying ice accumulation. In addition, the nearest level to the surface for which this variable is available from reanalysis is 1000 mb. Furthermore, an icing calculation based on 1000 mb level does not recognize the effect of topography, and thus produces underestimated results over mountainous areas, icing calculations over simple terrain areas are fairly reliable. This became apparent in the current study when icing calculations were done over the Bagotville area, using NARR cells at lower altitudes.

The calculation of icing events was based on the collection of cloud water on a cylindrical object that freezes upon contact at subfreezing temperature. The model evaluated an accurate duration of the icing events and the accumulation of ice over the simple site (Bagotville) during November and December of 1998, January, February and March of 1999. The comparison between measurement and calculation showed insignificant differences in ice accumulation from 0 mm to 0.3 mm, and in duration of icing events from 0 day to 0.2 day. On the other hand, the model revealed an underestimation of

icing events over the complex terrain site (Mt Bélair). However, during the winter months, the model-based icing calculation maintained a reasonable correlation with the measurements. During this period, the differences in ice accumulation varied from 5 mm to 16 mm, and varied from a 0.4 day to a 0.8 day in duration of icing events.

1.5 Conclusion

An updated mapping that represents the climatology of the in-cloud icing severity index for the northeast region of Quebec has been achieved. The ice accretion model was driven by meteorological variables cloud liquid water, wind speed and air temperature which originated from reanalysis data. The icing severity index that is based on ice accretion on a cylinder model, was used assess and display the risk potential of icing events. The model-based calculation of icing was validated with measurements from 2 sites that are topographically different. Consequently, comparisons between the model-based icing calculation and measurements revealed the reliability of the model to capture the observed icing events, especially over simple sites and during winter months. In the northeast region of Quebec, in-cloud icing events occur throughout the winter months in one place or another. The highest icing severity indexes were detected on the Atlantic side of the Gaspé Peninsula and the St. Lawrence River Valley and its surrounding areas. In these areas, the icing events are dependent on moisture flow, wind direction and topographic local effects.

One way to overcome these challenges may involve choosing alternative data sources, such Mesoscale meteorological models (GEM-LAM or WRF), that may provide

high-resolution data, otherwise a statistical downscaling of the NARR data can be used to serve as an optimal and less time-consuming alternative which may bypass the limitations of the coarse resolution. The icing severity index map provides the intensity and location of icing events risk potential, thereby enabling the prevention of hazardous icing events. Therefore in conclusion, the results found by creating an icing severity index map can facilitate and allow for well-scrutinized decisions when considering possible future projects for wind energy parks, transportation, electrical transmissions and aviation.

1.6 References

- Ahrens, C.D., 2007. *Meteorology Today. An Introduction to Weather, Climate, and the Environment*, 8th ed. Thomson Brooks/Cole, Belmont, CA 537.
- Anthes, R., 1983. Regional models of the atmosphere in middle latitudes. *Mon. Weather Rev.* 111, 1306–1335.
- Bernstein, B.C., Tiffany, A., Omeron, A., Politovich, M.K. and McDonough, F., 1998. Surface weather features associated with freezing precipitation and severe in-flight aircraft icing. *J. Atmos. Res.* 46, 57–73.
- Bernstein, B.C., Ratvasky, T.P., Miller, D.R., and McDonough, F., 2000. Freezing Rain as an In- Flight Icing Hazard. *NASA TM-2000-210058*. (June 2000).
- Bernstein, B.C., McDonough, F., Politovich, M.K., Brown, B.G., Ratvasky, T.P., Miller, D.R., Wolff, C.A. and Cuning, G., 2005. Current icing potential (CIP): algorithm description and comparison with aircraft observations. *J. Appl. Meteorol.* 44, 969–986.
- Bernstein, B.C., Wolff, C.A. and McDonough, F., 2007. An inferred climatology of Icing conditions aloft, including supercooled large drops. Part I: Canada and the Continental United States. *J. Appl. Meteorol. Climatol.* 46, 1857–1878.
- Best, A.C., 1950. Empirical formulae for the terminal velocity of water drops falling through the atmosphere. *Q. J. R. Meteorol. Soc.* 76, 302–311.
- Brodkey, R.S. and Hershey, H.C., 1988. *Transport Phenomena: A Unified Approach*. McGraw International Edition, New York (847 pp.).
- Byrkjedal, Ø. and Berge, E., 2008. The use of WRF for wind resource mapping in Norway. *9th WRF Users' Workshop*. (Colorado, USA).
- Carrière, J.M., Lainard, C., Le Bot, C., and Robart, F., 2000. A climatological study of surface freezing precipitation in Europe. *Meteorol. Appl.* 7, 229–238.
- Chaine, P.M. and Castonguay, G., 1974. New approach to radial ice thickness concept applied to bundle-like conductors. Canadian Climate Centre Internal Report, Industrial Meteorology - Study IV. Atmospheric Environment Service, Downsview, Ontario, Canada.
- Chaine, P.M., and Skeates, P., 1974. Wind and ice loading criteria selection. Canadian Climate Centre Internal Report, Industrial Meteorology – Study III. Atmospheric Environment Service, Downsview, Ontario, Canada.
- Claffey, K.J., Jones, K.F. and Ryerson, C.C., 1995. Use and calibration of Rosemount ice detectors for meteorological. *Atmos. Res.* 36, 277–286.

- Cober, S.G., Isaac, G.A. and Strapp, J.W., 1995. Aircraft icing measurements in east coast winter storms. *J. Appl. Meteorol.* 34, 88–100.
- DeBenedetti, P.G., 1996. *Metastable Liquids: Concepts and Principles*. Princeton University Press, Princeton, NJ (400 pp.).
- DeGaetano, A.T., 2000. Climatic perspective and impacts of the 1998 northern New York and New England ice storm. *Bull. Am. Meteorol. Soc.* 81, 237–254.
- Dobesch, H., Zach, S. and Tran, H.V., 2003. A New Map of Icing Potentials in Europe - Problems and Results. BOREAS VI.FMI, Pyhänturi, Finland 9.
- Environment Canada, 1998. Ice Storm '98: January 4–10, 1998 Ottawa, *courtesy of Environment Canada*.
- Fikke, S.M., 2005. Modern meteorology and atmospheric icing. In: *Proc 11th IWAIS, Montreal, Canada. June 2005*. Paper IW73.
- Fortin, G., Perron, J. and Ilinca, A., 2005. A Study of Icing Events at Murdochville: Conclusions for the Wind Power Industry. *Colloque international «énergie éolienne et sites éloignés», îles de la Madeleine, Canada 19-21 October 2005*.
- Green, S.D., 2006. A study of U.S. inflight icing accidents and incidents, 1978 to 2002. *AIAA 2006-82. 44th AIAA Aerospace Sciences Meeting and Exhibit, Reno, 9–12 January*.
- Gyakum, J.R. and Roebber, P.J., 2001. The 1998 ice storm - Analysis of a planetary-scale event. *Mon. Weather Rev.* 129, 2983–2997.
- Hardy, C., Brunelle, J., Manoukian, B. and Vilandre, R., 1998. Telemonitoring of climate loads on Hydro-Quebec 735 KV lines. *Atmos. Res.* 46, 181–191.
- Glossary of Meteorology. In: Huschke, R. (Ed.), *American Meteorological Society* (638 pp.).
- Isaac, G.A., 1991. Microphysical characteristics of Canadian Atlantic storms. *Atmos. Res.* 26, 339–360.
- Isaac, G.A., Cober, S.G., Strapp, J.W., Korolev, A.V., Tremblay, A. and Marcotte, D.L., 2001. Recent Canadian research on in-flight aircraft icing. *Can. Aeronaut. Space J.* 47, 1–9.
- Jacobson, M.Z., 2005. *Fundamentals of Atmospheric Modeling*. Cambridge University Press, Cambridge (813 pp.).
- Laakso, T., Peltola, E., Antikainen, P. and Peuranen, S., 2003. Comparison of Ice Sensors for Wind Turbines, *BOREAS VI. FMI, Pyhänturi, Finland 11*.

- Laflamme, J., 1993. Spatial variation of extreme values in the case of freezing rain icing. *Proc 6th IW AIS*, Budapest, Hongrie, pp. 19–23.
- Laforte, J.-L. and Allaire, M.A., 1992. Évaluation du Givromètre d'Hydro-Québec à Différentes Intensités de Givrage Sec et Humide. *Rapport HQ-92-02*.
- Ludlam, F.H., 1951. The heat economy of a rimed cylinder. *Q. J. R. Meteorol. Soc.* 77, 663–666.
- Makkonen, L., 1984. Modeling of ice accretion on wires. *J. Appl. Meteorol. Climatol.* 23, 929–993.
- Manwell, J.F., McGowan, J.G. and Rogers, A.L., 2010. Wind Energy Explained: Theory, Design and Application, 2nd ed. *John Wiley & Sons Ltd.*(689 pp.).
- Marwitz, J., Politovich, M., Bernstein, B., Ralph, F., Neiman, P., Ashenden, R. and Bresch, J., 1997. Meteorological conditions associated with the ATR72 aircraft accident near Roselawn, Indiana, on 31 October 1994. *Bull. Am. Meteorol. Soc.* 78, 41–52.
- Mason, B.J., 1971. The Physics of Clouds, Second edition. *Clarendon Press, Oxford* 671.
- Mazin, I.P., Korolev, A.V., Heymsfield, A., Isaac, G.A. and Cober, S.G., 2001. Thermodynamics of icing cylinder for measurements of liquid water content in supercooled clouds. *J. Atmos. Ocean. Technol.* 18, 543–558.
- McComber, P., Latour, A., Druetz, J. and Laflamme, J., 1996. The icing rate meter, an instrument to evaluate transmission line icing. *Proc 7th IW AIS*. Chicoutimi, Canada, pp. 159–168.
- McKay, G.A. and Thompson, H.A., 1969. Estimating the hazard of ice accretion in Canada from climatological data. *J. Appl. Meteorol.* 8, 927–935.
- Mesinger, F., DiMego, G., Kalnay, E., Mitchell, K., Shafran, P.C. and Ebisuzaki, W., 2006. North American Regional Reanalysis. *Bull. Am. Meteorol. Soc.* 87, 343–360.
- Messinger, B.L., 1953. Equilibrium temperature of an unheated icing surface as a function of air speed. *J. Aerosol Sci.* 29–42 (Jan).
- NARR homepage, e. <http://www.emc.ncep.noaa.gov/mmb/rrean/>.
- NCEP, N. W. S., NOAA, U.S. Department of Commerce, 2004. NCEP North American Regional Reanalysis, NARR, DSI-6175 (Maryland, USA).
- Newton, D.W., 1978. An integrated approach to the problem of aircraft icing. *J. Aircr.* 15, 374–380.

- Nygaard, B.E.K., Kristjánsson, J.E. and Makkonen, L., 2011. Prediction of in-cloud icing conditions at ground level using the WRF model. *J. Appl. Meteorol. Climatol.* 50, 2445–2459.
- Parent, O. and Ilinca, A., 2011. Anti-icing and de-icing techniques for wind turbines. *Cold Reg. Sci. Technol.: Crit. Rev.* 65, 88–96.
- Petty, K.R. and Floyd, C.D.J., 2004. A Statistical Review of Aviation Airframe Icing Accidents in the U.S. 11th ARAM Conf., Hyannis, 11–14 Oct. *American meteorological Society*, Boston.
- Rasmussen, R. and Geresdi, I., 2005. Freezing drizzle formation in stably stratified layer clouds. Part II: the role of giant nuclei and aerosol particle size distribution and solubility. *J. Atmos. Sci.* 62, 2037–2057.
- Ratvasky, T.P., Van Zante, J.F. and Riley, J.T., 1999. NASA/FAA Tailplane Icing Program Overview. *NASA TM-1999-208901*. (Jan).
- Rock, P.A., 2003. *Chemical Thermodynamics*, University Science Books, USA (548 pp.).
- Sand, W.R., Cooper, W.A., Politovich, M.K. and Veal, D.L., 1984. Icing conditions encountered by a research aircraft. *J. Clim. Appl. Meteorol.* 23, 1427–1440.
- Savadjiev, K., Farzaneh, M., Druetz, J., McComber, P. and Paradis, A., 1999. Analysis and interpretation of icing rate meter and load cell measurements on the Mt. Bélair icing site. *Proc of the Ninth International Offshore and Polar Engineering Conference* (Brest, France, May 30-June 4, 1999).
- Stallabrass, J.R. and Hearty, P.F., 1967. The icing of cylinders in conditions of simulated freezing sea spray. Mechanical Engineering Report MD-50, NRC No. 9782. *National Research Council of Canada*, Ottawa, Canada (July, 1967).
- Stein, P., 1993. Rosemount freezing rain sensor. *Proc. Sixth Int. Workshop on Atmospheric Icing of Structures*. Budapest, Hungary, Hungarian Electrotechnical Association, pp. 121–124.
- Strapp, J.W., Stuart, R.A. and Isaac, G.A., 1996. A Canadian climatology of freezing precipitation, and a detailed study using data from St. John's, Newfoundland. *Proc. Int. Conf. On Aircraft Inflight Icing. Federal Aviation Administration*, Springfield, VA, pp. 45–56.
- Stuart, R.A. and Isaac, G.A., 1999. Freezing precipitation in Canada. *Atmosphere-Ocean* 37–1, 87–102.

Tammelin, B. and Säntti, K., 1998. Icing in Europe. Proc. Fourth Int. Conf. on Wind Energy Production in Cold Climate, BOREAS IV. Finnish Meteorological *Institute*, Hetta, Finland, pp. 125–132

Tammelin, B., Kimura, S., Säntti, K. and Seifert, H., 1999. Icing in Europe – effect upon wind power production. Proceedings of the EWEC. Nice, France 1–5 March, *European Wind Energy Conference*, pp. 1051–1054.

Tammelin, B., Cavaliere, M., Holttinen, H., Morgan, C., Seifert, H. and Säntti, K., 2000. *WECO final report. European Commission*, Brussels, Belgium.

Tammelin, B., Dobesch, H., Durstewich, M., Ganander, H., Kury, G., Laakso, T. and Peltola, E., 2005. Wind turbines in icing environment: improvement of tools for siting. Certification and Operation - *NEW ICETOOLS.FMI 127*.

Vedin, H., 1998. Distribution of Freezing Rain and Drizzle in Sweden during the Period 1961-1990. Rep. L1998-1839. *Swedish Meteorological and Hydrological Institute* (6 pp.).

Walton, W.H., Woolcock, A., 1960. The suppression of airborne dust by water spray. *Int. J. Air Pollut.* 3, 129–153.

Yip, T.C., 1995. Estimating icing amounts caused by freezing precipitation in Canada. *Atmos. Res.* 36, 221–232

CHAPTER 2

HYBRID FINE SCALE CLIMATOLOGY AND MICROPHYSICS OF IN-CLOUD ICING: FROM 32KM REANALYSIS TO 5KM MESOSCALE MODELING

*This Chapter is published in the form of an original scientific article
in the journal of*

Atmospheric Research, 2015, vol 154, p. 175-190

dx.doi.org/10.1016/j.atmosres.2014.11.006

Fayçal Lamraoui ^{1*}, Robert Benoit ³, Jean Perron ¹, Guy Fortin ², Christian Masson ³

¹ *The Anti-Icing Materials International Laboratory, University of Quebec at Chicoutimi*

² *Bombardier Aerospace*

³ *École de technologie supérieure, University of Quebec*

* Corresponding Author address:

Fayçal Lamraoui

*The Anti-Icing Materials International Laboratory, University of Quebec at Chicoutimi
555, boulevard de l'Université, Chicoutimi, QC, G7H 2B1 Canada*

Email: faycal.lamraoui@gmail.com

2. HYBRID FINE SCALE CLIMATOLOGY AND MICROPHYSICS OF IN-CLOUD ICING: FROM 32KM REANALYSIS TO 5KM MESOSCALE MODELING

Abstract

In-cloud icing can impose safety concerns and economic challenges for various industries. Icing climate representations proved beneficial for optimal designs and careful planning. The current study investigates in-cloud icing, its related cloud microphysics and introduces a 15-year time period climatology of icing events. The model was initially driven by reanalysis data from North American Regional Reanalysis and downscaled through a two-level nesting of 10 km and 5 km, using a limited-area version of the Global Environment Multiscale Model of the Canadian Meteorological Center. In addition, a hybrid approach is used to reduce time consuming calculations. The simulation realized exclusively on significant icing days, was combined with non-significant icing days as represented by data from NARR. A proof of concept is presented here for a 1000 km area around Gaspé during January for those 15 years.

An increase in the number and intensity of icing events has been identified during the last 15 years. From GEM-LAM simulations and within the atmospheric layer between 10 m and 200 m AGL, supercooled liquid water contents indicated a maximum of 0.4 g m^{-3} , and 50% of the values are less than 0.05 g m^{-3} . All values of median volume diameters (MVD) are approximately capped by $70 \text{ }\mu\text{m}$ and the typical values are around $15 \text{ }\mu\text{m}$. Supercooled Large Droplets represent approximately 5%. The vertical profile of icing climatology demonstrates a steady duration of icing events until the level of 60 m. The altitudes of 60 m and 100 m indicate substantial icing intensification toward higher elevations. GEM-LAM demonstrated a substantial improvement in the calculation of in-cloud icing, reducing significantly the challenge posed by complex terrains.

Keywords: Mesoscale modeling, reanalysis, in-cloud icing, cloud microphysics, climatology

2.1 Introduction

Freezing precipitation and its related icing hazards have been largely investigated in previous studies (Bernstein et al., 1998; Bernstein et al., 2000; Carrière et al., 2000; Fernández-González et al., 2014; Laflamme, 1993; Stuart and Isaac, 1999). According to Fikke (2005), atmospheric icing is the accumulation of ice generated from any meteorological condition. More specifically, the current study focuses on in-cloud icing which is originated from the immediate freezing of non-precipitating supercooled cloud droplets upon contact with a solid surface (Ahrens, 2007; Cortinas et al., 2004; Debenedetti, 1996; Jacobson, 2005; Rock, 2003).

Despite the low intensity of in-cloud icing compared to freezing precipitation, economic and safety consequences on various sectors (wind turbine, electric cables, and aviation) can be devastating, especially those associated to prolonged occurrences of icing events (Laakso et al., 2010).

In addition, the precipitation is commonly considered the only element for the hydrological cycle and the unique source of water for watersheds. According to previous study (Schemenauer and Cereceda, 1994), this consideration can generate a serious underestimation of water input, over foggy forested high-elevation areas that are exposed to frequent advection of near surface clouds. Furthermore, a precise estimation of ice accretion from non-precipitating cloud droplets can contribute to the improvement of water budget calculations over complex terrains or areas with highly elevated obstacles (trees, building, wind turbine ...) that intercept cloud advection.

The relevant meteorological factors that control the atmospheric icing are the liquid

water content, air temperature, wind speed and droplet size (e.g., Shin et al., 1991). The occurrences of hazardous atmospheric icing events are associated with supercooled droplets. The supercooled liquid water (SLW) is one of the very significant elements that govern the weather. Furthermore, it is an important component for mixed phase clouds (Boudala et al., 2004), cloud microphysical (Morrison et al., 2011) and radiative properties (Bennartz et al., 2013).

The presence of supercooled liquid water in various types of cold clouds is very common (Turner, 2005; Shupe, 2011), and can be found at -40°C (e.g., Heymsfield et al., 1991). Cober et al. (2001) found that liquid, mixed, and glaciated phases are represented by the portions of 40%, 40%, and 20% of the total clouds, respectively. The coexistence of the supercooled cloud droplets with solid hydrometeors assures maximum crystal mass growth rate (at a given temperature) and the potential for accretion of droplets by crystals.

Illingworth et al. (2007) reported that there is a challenge encountered in the representation of mixed phase cloud in numerical weather prediction and climate models. According to Lau and Wu (2003) even in the tropics, 69% of liquid precipitations are originated from ice phase hydrometeors in higher altitudes.

Low concentration of ice Nuclei causes the inhibition of glaciation process, and subsequently, favors an increase of Supercooled Large Drops (SLD) (Fernández-González et al., 2014). Frequently, SLD refers to drop size between $50\ \mu\text{m}$ and a few hundred μm (Politovich, 1996). Other studies (e.g., Sand et al., 1984) consider the range between $30\ \mu\text{m}$ and $400\ \mu\text{m}$ as the critical sizes of SLD that are responsible for most of the serious aircraft icing incidents. An experimental study (Politovich, 1996) found that SLW higher than $0.2\ \text{g}$

m^{-3} with SLD larger than $30 \mu\text{m}$ generate in-flight icing that cause a significant rapid degradation. With regard to SLD data, the majority of measurements were within the range of temperatures $[-24^{\circ}\text{C}$ to 0°C] in stratiform and winter frontal clouds (Cober et al., 2001).

In reference to aircraft icing, even low concentrations (10 L^{-1}) of SLD that are higher than $50 \mu\text{m}$ can be seriously hazardous (Bernstein et al 2007), when exposure time is within 10-15 min (Politovich, 1989). Furthermore, Marwitz et al. (1997) confirmed that low SLD concentrations (10 L^{-1}) are often found in the Maritime stratiform clouds. Lasher-Trapper et al. (2008) reported that giant aerosols have a very limited contribution in the formation of SLD. On the other hand, various favourable conditions can lead to accelerated formation of SLD such as: the presence of low droplet concentration with larger cloud liquid water content (Rasmussen et al., 1995; Murakami et al., 1992); the presence of vertical wind shear in stable thermodynamic profile at cloud top (Pobanz et al., 1994) and the high water vapor supersaturation (Korolev and Isaac, 2000).

Using the North American regional reanalysis data (NARR), at an extended time period of 32 years during winter months, Lamraoui et al. (2014) determined that the mean duration of icing events is approximately 6 h.

The current study provides further investigation on the effect of cloud microphysics parameters that contribute in generating atmospheric icing (Rime or Glaze) during wintertime. An earlier study (Lamraoui et al., 2013) demonstrated that NARR has limitations on representing atmospheric icing over complex terrains, due to the coarse resolution and lack of terrain-following data therein for cloud parameters and accretion calculation. Therefore, this study represents the climatology of in-cloud icing (duration of

icing events, ice accumulation and Icing Severity Index (ISI)) at a finer resolution using a limited-area version of the Global Environment Multiscale model (GEM-LAM). This regional non-hydrostatic atmospheric model of the Canadian Meteorological Center (CMC) was initially driven by NARR data and downscaled through a two-level nesting. The cloud microphysics is available in GEM through an advanced multiphase scheme (Milbrandt and Yau, 2005).

2.2 Method

A previous study by Lamraoui et al. (2013) analysed the climatology of atmospheric icing by mapping the ISI over the Eastern part of the province of Quebec (Canada) which spanned a 32-year period. The representation of icing severity used meteorological variables with a resolution of 32 km extracted from NARR. The use of NARR alone indicated that the lack of horizontal and vertical space resolution imposes a challenge on the calculation of icing events over complex terrains, especially during the months of November and March when air temperature is near freezing point. In order to counterbalance the lack in NARR resolution, this study aims to obtain higher resolution climatology of atmospheric icing through the use of a finer scale mesoscale model GEM-LAM with a resolution of 5km. Although the use of a mesoscale model for a 32-year period provides more localized details it also in turn becomes a time consuming process. Alongside this, the calculation of atmospheric icing from the NARR data neglects details within 32 km over hilly topography. For this reason, to reach an optimal compromise and to obtain detailed icing events at finer resolution with reasonable time consuming calculations,

a hybrid approach was introduced. As shown in Figure 2.1, this approach involves the combination between North American Regional Reanalysis and the mesoscale limited area model GEM-LAM-5km. To identify the significant icing events, a preliminary climatology of icing events was produced based on reanalysis. Subsequently GEM-LAM-5km was applied during the significant icing events in order to enable their higher resolution calculation of icing events. The resulted ISI mapping is an indicator of risk levels of icing events. This information will prove useful to prevent damages and economical losses due to icing events by documenting their risk factor.

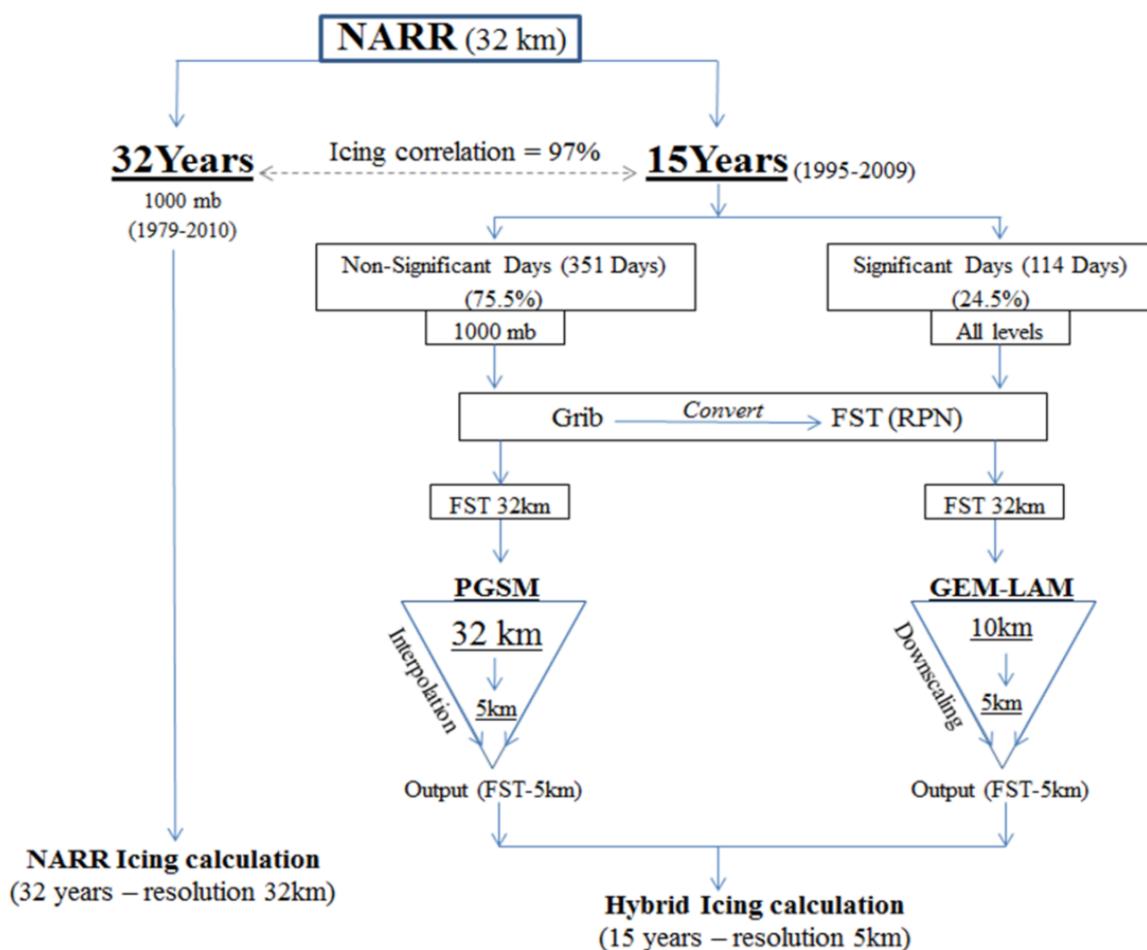


Figure 2.1. Hybrid approach using NARR 32km and GEM-LAM 5km combination.

To avoid the time consuming calculations for a 32-year period and without affecting the quality of the results, the climatology of a 32-year period is substituted by a comparable representative 15-year period. The period of 15 years is an optimal time scale that is determined based on several motivating factors that characterize the available data, the computation resources and the period of interest related to the current study. This study focuses mainly on wind turbines that have an approximate economical life span of 15 years. The use of a 15 year time period was a reasonable choice given the computation resources that are available. Lastly, for the wind turbine industry, it is more relevant to use a recent time period that reflects the current and near future climate. Regarding the mesoscale modeling, only the days with significant ISI in the following five locations across the province of Quebec (Canada) (Lamraoui et al., 2013); Mount-Bélair, Rivière-du-Loup, Rimouski, Matane and Gaspé were considered. These sites represent a variety of topographies which are exposed to the Maritime and Continental air masses.

All available files from NARR database have a binary GRIB format which is not compatible in order to run GEM-LAM. For this reason, conversion tools are created to convert GRIB format files from reanalysis to RPN (*Recherche en Prévision Numérique*) file format (FST) required for the mesoscale model GEM-LAM: Camion (2012) showed that this can be done using a polar stereographic mesh that optimally preserves the accuracy of the original NARR data, using MATLAB. Besides loading NARR files, additional files were added which contain sea surface temperature and snow depth, necessary for initiating and providing the nesting data needed by the GEM-LAM.

Following the creation of a 15-year database of RPN files, two downscaling procedures were performed using GEM-LAM and PGSM (Programme Général de Sortie des Modèles). The interpolation of data using PGSM from coarse to fine scale is only in the horizontal and actually is an oversampling of the NARR original data. On the other hand, GEM-LAM, being a full Navier Stokes solver of the atmospheric dynamics, is able to downscale these RPN files along horizontal, vertical and time dimensions. The limited area model is focused on the Eastern part of the province of Quebec (Canada), spanning ~1000 km and only for January here. This section of the study aims to create a refinement of the NARR database for only significantly severe days with the 5 km resolution. If successful, this proof of concept can be applied to other cold areas of North America (with NARR) and of the entire world using other global reanalyses such as the Era-Interim (Dee et al., 2011)..

2.3 Results

2.3.1 Climatology of atmospheric icing

In order to quantify this climate shift, with NARR data that spans a period of 30 years (1980-2009) over Quebec regions and part of New Brunswick, the mean value of ice accumulation and the duration of icing events are calculated and presented in Figure 2.2. This figure reveals that the month of January 1998 holds the longest mean icing event duration, followed by 1995, 2001, 2008 and 2003 respectively. One notices that all these long icing durations are found in the last 15 years. The Figure 2.2 shows the mean values during two periods of 15 years [1980-1994] and [1995-2009]. The last 15-year period reveals an average icing duration of 50 h which exceeds the first 15-year period that

indicates a shorter mean duration of icing events of approximately 36 h. Moreover, the monthly mean of ice accumulation in Figure 2.2 manifests its maximum on January 1995 with approximately 87 mm, followed by 1998 and 2008 with approximate accumulations of 50 mm and 45 mm respectively. Further to this, the monthly mean accumulation during 1995-2009 is 28 mm which is also higher than the monthly mean accumulation of 18 mm during 1980-1994. Overall, the results of Figure 2.2 reveal an increase in the duration of icing events and more accumulation of ice. Furthermore, these results confirm that, considering 30 years will underestimate the mean values of the duration and accumulation of icing events of the last 15 years. Therefore, for industries that are vulnerable to icing conditions, it is appropriate to count on the latest climate representation of icing.

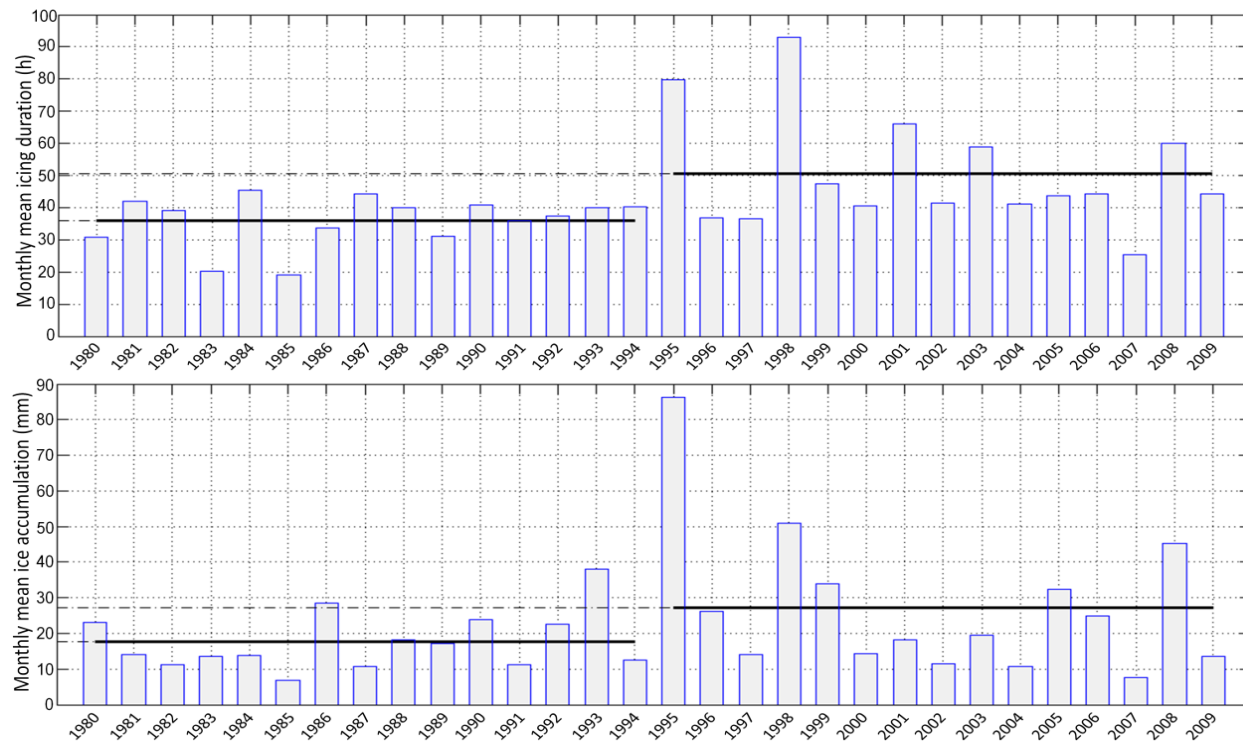


Figure 2.2. Mean values of the ice accumulation and the duration of icing events (January: 1980-2009)

2.3.2 Transition from 32-year to 15-year

In reference to the previous study by Lamraoui et al. (2013) that used the time period of 32 years, the present study is a continuing work that attempts to refine the previous results in order to achieve the representation of atmospheric icing at a finer scale. Lamraoui et al. (2013) calculated the ISI obtained from NARR data over a zone of $17 \times 20 = 340$ NARR cells (each having 32×32 km) that is approximately centred on the city of Rivière-du-Loup (QC - Canada). This previously calculated ISI spans a 32-year time period. Since the present study addresses a shorter recent 15-year time period (1995-2009), Figure 2.3 illustrates the comparison of ISI obtained from NARR data for 32-years (Y-axis) versus that 15-year (X-axis) time period. The 340 dots in Figure 2.3 represent the mean values of ISI on each NARR cell during the time periods of 32 years and 15 years. This comparison manifests a good agreement between the two time periods with a high correlation of 97%. This result demonstrates that both time periods have similar spatial distribution of ISI with more intense values during the 15-year time period. Consequently, the climatology of ISI for both time periods has an approximately similar spatial pattern but more intense severity, by about 47%, during the latest 15-year period.

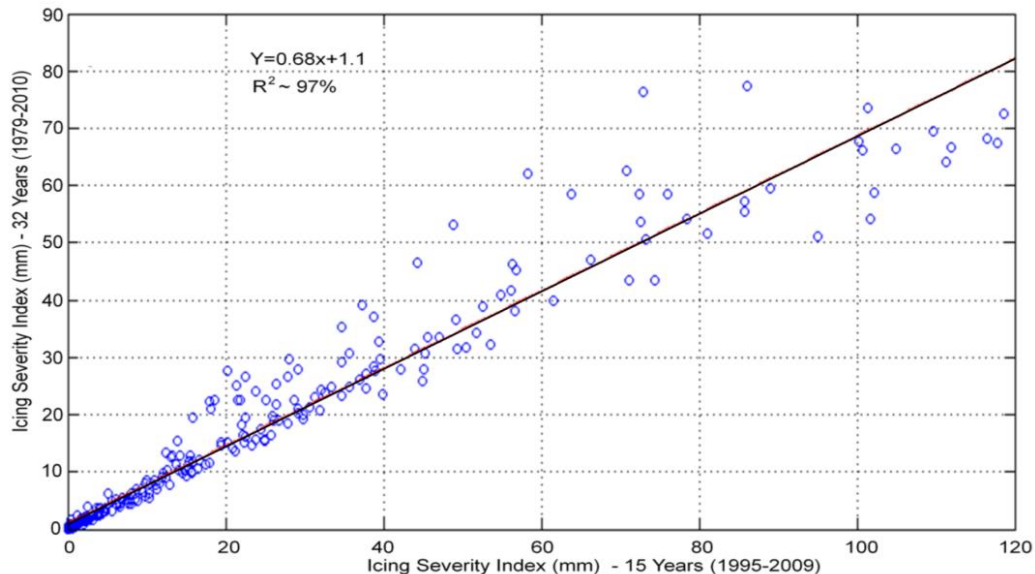


Figure 2.3. Comparison between the Icing Severity Index during 32 years and 15 years over 17 x 20 NARR cells centred at Rivière-du-Loup

In order to show and verify the results presented in Figures 2.2 and 2.3, in terms of mapping, Figure 2.4 reveals further details about the trend of icing events by comparing the duration, ice accumulation and severity index of icing events. In order to perform a reliable comparison, the highest values in the mapping representation of the 15-year time period were clipped at the maximum value obtained from the time period of 32 years. Figures 2.4a, 2.4c and 2.4e illustrate the 32-year time period climatology of the duration of icing events, the ice accumulation and the ISI, with maximum values of 140 h, 90 mm and 80 mm respectively.

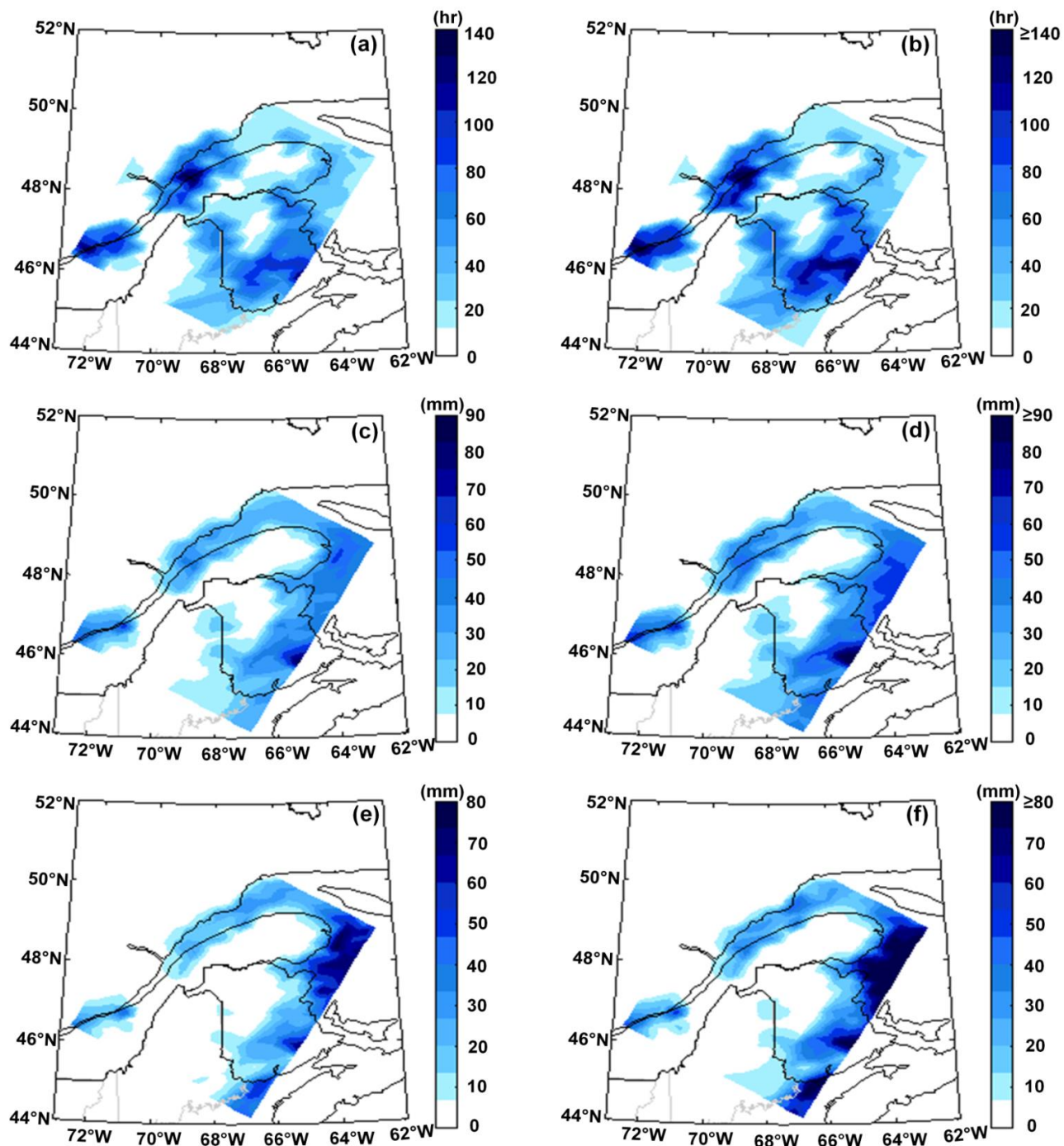


Figure 2.4. Comparison between 32 years and 15 years: Duration of icing events (a,b), ice accumulation (c,d) and Icing severity index (e,f). Colour scales are clipped for the 15 year period.

In addition, the climatology of icing shown in Figures 2.4b, 2.4d and 2.4f demonstrates more accentuated and intense peaks, with slightly wider features. The comparison between a 32-year and a 15-year time period, of the same database revealed an accentuation in the intensity of atmospheric icing (Duration, ice accumulation and ISI) during the latest 15-year time period. Therefore, in order to assess the severity of icing events prior to wind farm implantation, it is more appropriate to use 15-year estimation rather than 32-year estimation, since a 32-year assessment tends to reduce the average of icing severity.

2.3.3 GEM-LAM and NARR performances

The orography has a significant influence on enhancing the cloud water content, cloud phase, evaporation and sublimation of cloud hydrometeors. Therefore, it is crucial for numerical weather modeling to utilize the topography at higher resolution to achieve a better representation of weather conditions over mountainous and complex terrain areas. Since this study involves the improvement of the resolution using the output of GEM-LAM 5km rather than those obtained from NARR 32 km data, Figure 2.5 demonstrates the disparity in topography from different resolutions. This figure is a cross section of the elevations intersecting the site of Mount-Bélair (~ 480 m) near Quebec City (Canada). Figure 2.5 shows a noticeable difference between the three topographies. The resolution of 32 km NARR flattens the elevations by averaging out the details within 32 km. With reference to 1 km, this coarse resolution of 32 km shows underestimations that can reach 400 m, and also potential overestimates that can exceed 200 m. The difference is more pronounced in the sides of each NARR 32 km cell. Also, when compared to the resolution

of 1 km, the resolution of 5 km of GEM-LAM manifests an improvement and considerably reduces errors in elevations. The real elevation of the Mount-Bélair site is approximately 480 m. The GEM-LAM 1km resolution indicates the best estimate of 453 m followed by GEM-LAM 5km and NARR 32 km with elevations of 334 m and 147 respectively.

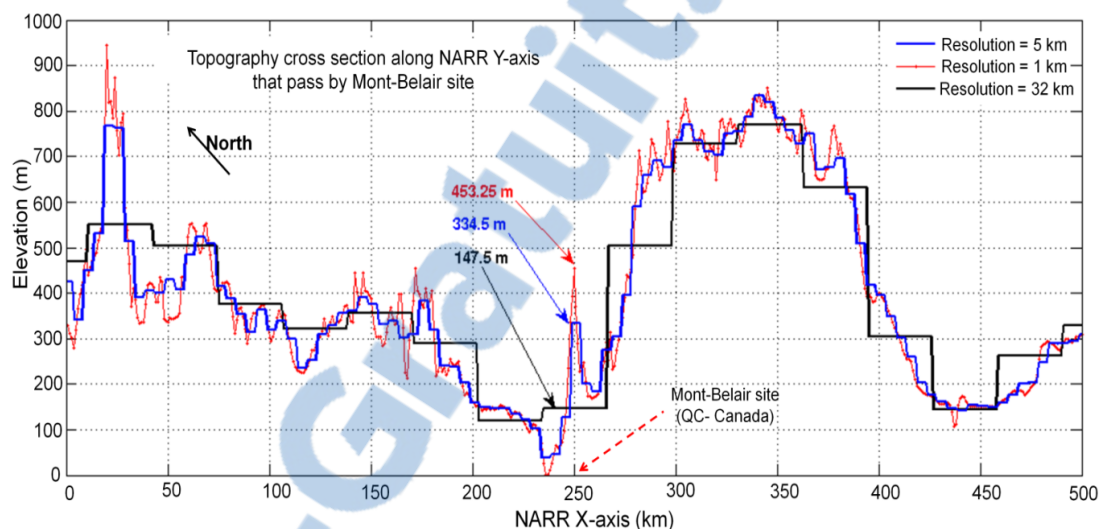


Figure 2.5. Topography Cross Section Viewed by NARR 32km, GEM-LAM 5km and GEM-LAM 1km

In order to test the sensitivity to the resolution along with meteorological variables directly involved in calculating icing events, Figure 2.6 shows a comparison of temperatures at 30 m above ground level obtained from observation at Mount-Bélair, GEM-LAM 5 km and NARR 32 km. The simultaneous values of a sequence of 22 events from the three sources occurred during the month of January 1999. Figure 2.6a shows the temperature values (Y-axis) for each corresponding observation number (X-axis). Additionally, Figure 2.6b quantifies the differences from the models (NARR, GEM-LAM) with reference to observations. The behaviour of the curves in Figure 2.6 reveals that the output of the two models (NARR, GEM-LAM) is warmer than the observations. The

results of GEM-LAM 5 km are more accurate compared to those from NARR. The better consistency of GEM-LAM 5 km with the observations can be explained by the enhanced resolution of the topography discussed in Figure 2.5 and the more sophisticated microphysics scheme (M&Y) used with GEM-LAM than that in the NARR

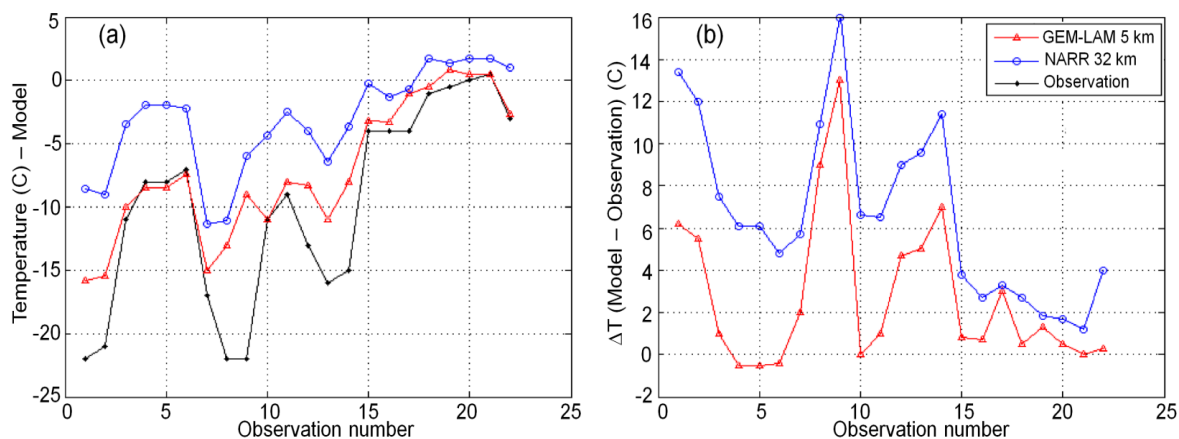


Figure 2.6. Comparison of Temperatures from NARR 32 km, GEM-LAM 5km and Observation

The results of both Figures 2.5 and 2.6 have shown the improvement brought by GEM-LAM compared to NARR. It would even be better and more recommended to use GEM-LAM 1 km; however, the time consuming calculation prevents this option. Subsequently, this study is limited to the use of GEM-LAM 5 km. One could perhaps simply replace the GEM-LAM-1km with an air-mass adjustment of the 5 km results to the 1 km terrain (eg. Byrkjedaal, 2013) to reap most of its increased performance. GEM-LAM has already shown good performance in producing the key parameters that control in-cloud icing. Through the use of three-level nesting that target the resolution of 1km and comparison with observation, Yang et al. (2012) investigated in-cloud icing on Mount Washington and Prescormic (2014) explored icing events on sites in Gapsé. Furthermore,

with regard to in-cloud icing in Sweden, Prescormic (2014) compared the performance of GEM-LAM versus MM5 from a previous study (Drage and Hauge, 2008). Both studies (Yang et al., 2012; Prescormic, 2014) used similar triple nesting simulation strategies with resolutions 10 km, 5 km and 1 km and timesteps 300 s, 60 s and 30 s respectively. The obtained results of 1km resolution demonstrated an agreement with observations over complex terrains for case studies during time periods less than 24 h. The current study investigates the climatology of in-cloud icing spanning a long time period. Consequently, triple nested GEM-LAM simulations that target the resolution of 1 km appear to be very time consuming. Therefore, the resolution of 5 km that demonstrates an improvement compared to NARR 32 km is considered in order to cover the climatology during 15 years.

2.3.4 Selection of significant days

After having demonstrated the benefit of use the latest 15 years versus 32 years, and also the preference of the data of finer scale resolution (GEM-LAM 5km) compared to the coarse resolution, Table 1 identifies the days selected for downscaling by mesoscale modeling. Table 1 presents the 114 days that were selected over 15 year period (1995-2009). With regard to icing severity, these significant days represent an average of 7.6 days per year. These days were determined based on the ISI over the critical selected sites (Mount-Bélair, Riviere du Loup, Rimouski, Matane, Gaspé) from the zone of the study. The selected days are associated with icing events occurrences that have an average daily icing rate of 0.04 mm h^{-1} and more. In Table 2.1, it is noticeable that some years have more than 10 significant severe icing days per month, with January 1998 having the most at 13 significant icing days, followed by 2005, 2006, 2003, 2008 with 12 days, 11 days, 10 days

and 10 days respectively. On the other hand, January 2002 has the shortest severe period with only 3 significant icing days.

Table 2.1 : Selected significant days for GEM-LAM

Year	Nb of days	Selected days for GEM-LAM
1995	08	14-15-16-17-18-19-20-21
1996	08	07-17-18-19-22-23-27-28
1997	05	01-09-15-19-25
1998	13	02-03-04-06-07-08-09-15-18-20-24-25-28
1999	09	03-04-08-16-18-19-23-24-28
2000	08	07-09-10-18-24-26-29-30
2001	04	19-22-23-30
2002	03	02-21-30
2003	10	02-04-05-06-15-16-24-26-29-31
2004	04	02-03-12-27
2005	12	01-03-04-08-09-10-11-12-13-14-17-24
2006	11	01-03-04-08-09-11-13-14-17-26-28
2007	04	01-03-18-19
2008	10	01-04-05-06-07-17-18-22-29-30
2009	05	12-17-25-27-28

In order to test the sensitivity of the selection of significant days shown in Table 2.1, Figure 2.7 compares ISI obtained over the site of Mount-Bélair using only the selected days versus using all the days of the month.

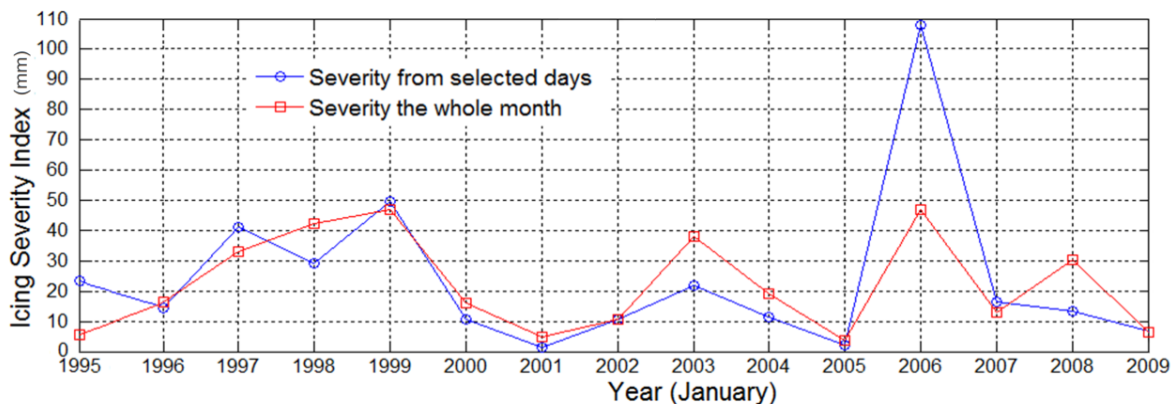


Figure 2.7. Comparison of ISI over Mount-Bélair (15 years) with all days versus selected days.

The site of Mount-Bélair is recognized by its frequent and severe icing events. The tendency of the curves in the comparison in Figure 2.7 shows a satisfying correlation with slight differences between the ISI values of the same year. Other than 1995, 1997 and 2006, the ISI of the selected days have an average underestimation of 6.5 mm compared to the ISI of the entire month. The average ISI over Mount-Bélair is 24.5 mm. Therefore, the selection of significant days which represents only 24% of the total duration appears to be adequate in describing the level of Icing Severity.

2.3.5 Mesoscale modeling and simulation setup

To acquire the key meteorological variables for icing events at fine resolution during the selected days introduced. In the presented Table 2.1, a series of numerical procedures have been performed. This section describes the steps followed for the mesoscale modeling. The simulations involve two different grids with three nested domains. As shown in Table 2.2, the simulation is initially (i.e. on the outer domain) driven by NARR data transformed to polar stereo grids in FST files (Camion, 2012) which is available every 3h with a spatial resolution of 32 km. Simulations that utilize GEM-LAM are those of the domains D2 and D3 occupying 124x124 grids 200x200 grids with spacing of 10 km and 5 km respectively. The timesteps associated with the domains D2 and D3 are 5 min and 1 min respectively.

The objective of the simulations is to obtain output by series of 24 h that correspond to each of the significant days (Table 2.1). To reduce the numerical errors from the initialization and to ensure stabilization of the model, the beginning of each simulation is advanced in time. The first simulation of the domain D2 begins 6 h prior to each target day. Then the second simulation, which is automatically initialized by the output of the first

simulation, starts 3 h prior to each target day (3 h after the first simulation). Both simulations finish at the end of each target day. Consequently, both simulations for the domains D2 and D3 cover periods of time of 30 h and 27 h respectively. The target time period is the last 24 h.

Table 2.2 : Grid setup for the numerical experiment

Domain	dx (km)	Nx	Ny	Time step (s)	t0 (hr)	Data format	Run Period (hr)	Source
D1	32	349	277	-	-	Grib	-	NARR
D2	10	124	124	300	-6	RPN	30	GEM-LAM
D3	5	200	200	60	-3	RPN	27	GEM-LAM

Table 2.3 : The lowest 17 vertical levels used in GEM-LAM that correspond to ABL

Level Number	Hybrid level	AGL (m)
40	0.85400	1097
41	0.87250	948
42	0.88960	813
43	0.90530	691
44	0.91980	581
45	0.93300	482
46	0.94510	392
47	0.95620	311
48	0.96600	240
49	0.97450	179
50	0.98180	128
51	0.98750	87
52	0.99180	57
53	0.99490	36
54	0.99700	21
55	0.99850	10
56	0.99950	3

In addition to the advantage of its high customizable resolution, The GEM model provides output along the atmospheric column at 56 terrain-following vertical levels above the ground. With regard to the atmospheric boundary layer (ABL), Table 2.3 shows the

lowest 17 vertical levels, their corresponding hybrid levels and above ground levels (AGL).

The present study uses the versions 4.2 of GEM of Environment Canada with the physics package RPNPHY_5.2.1. The two simulation zones share the same center, which is located near the city of Rivière-du-Loup (QC- Canada) defined by the latitude 47.83° and the longitude -69.53° . For the purpose of numerical optimization and to prevent the narrowing effect within the calculation domains toward the North, the longitude of the same center is rotated 20.47° in order to ensure that the numerical equator is oriented toward the East while passing through the Rivière-du-Loup location.

Given the required variables for the calculation of icing events and the location of the target domains, the configuration is based on the double moment (DM) condensation scheme of Milbrandt and Yau (Milbrandt and Yau, 2005) and the activation of CCN.

Commonly, continental air masses carry much more aerosols that serve as cloud condensation nuclei (CCN) compared to maritime air masses. Therefore, with the same moisture, Maritime air masses (CCN ~ 10 to 100 cm^{-3}) originate larger droplets compared to Continental air masses (CCN ~ 100 to 1000 cm^{-3}) (Pruppacher and Klett, 2010). More precisely, for the simulation of this study, Maritime air masses considered by GEM-LAM use a CCN concentration of 80 cm^{-3} .

Both domains D2 and D3 of nested simulations are presented in Figure 2.8 by the two outer squares, which are geometrically correlated. D2 and D3 occupy areas of $1240 \times 1240 \text{ km}^2$ and $1000 \times 1000 \text{ km}^2$ respectively. D1, the NARR domain, covers more than the entire area depicted in Figure 2.8. Furthermore, within D3 Figure 2.8 illustrates an additional delineation represented by a slanted rectangular shape. This third area that covers the Gaspé

Peninsula and its surroundings is the target zone to be used for the purpose of comparison with the results shown in Figure 2.4 and also the results of a previous study (Lamraoui et al., 2013). The target zone occupies an area of approximately $640 \times 544 \text{ km}^2$ (i.e. the 20×17 NARR cells mentioned in section 2).

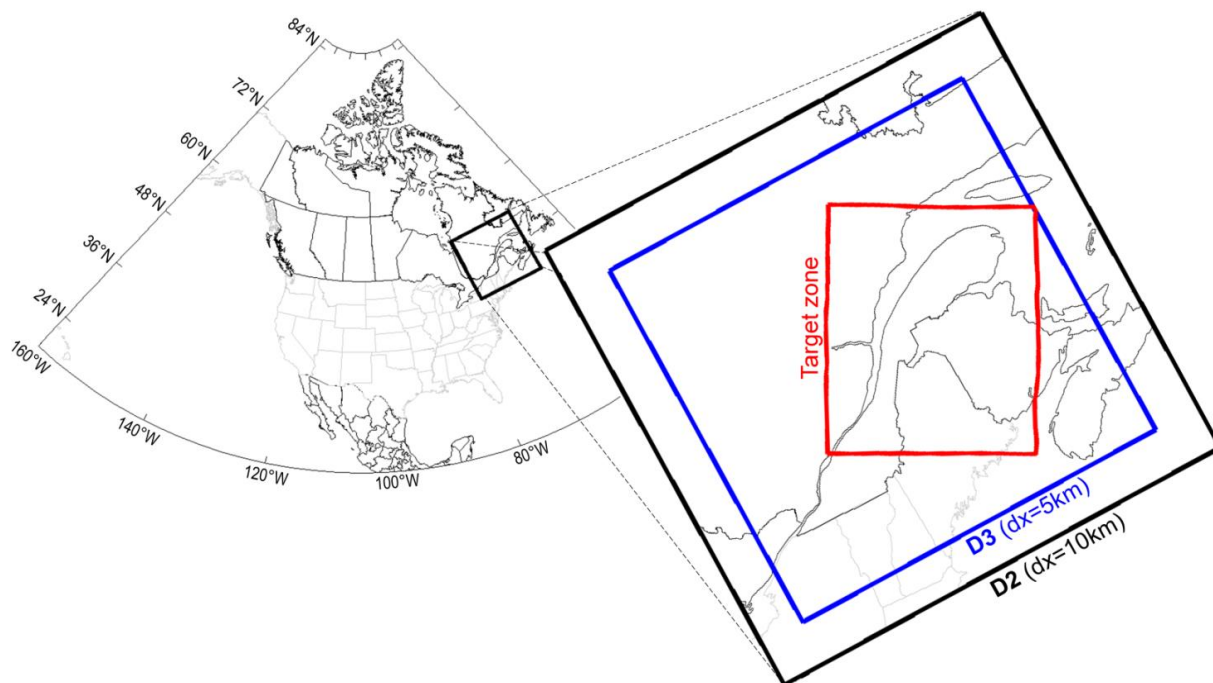


Figure 2.8. Simulation domains and target zone

The simulations of GEM-LAM were realized using the cluster Boreas (ETS – University of Quebec) which is a high performance supercomputer cluster with 464 processors (58 nodes) in parallel with 928 GB of RAM, infiniband technology and equipped with Sun Grid Engine (SGE) batch-queuing system.

For this study, eight simulations were launched simultaneously and continuously, until covering all target days. Each simulation made use of one node (8 processors) and lasts

approximately for 8 h including both domains D2 and D3 with 360 timesteps, 1620 timesteps respectively.

2.3.6 Statistics and cloud microphysics properties

After completing the simulations and retrieving the required variables for the calculation of icing events, Figure 2.9 was prepared to scrutinize the microphysical properties of supercooled clouds associated with the occurrence of icing events. Moreover, Figure 2.9 depicts statistically the interrelationship between the key parameters that determine the intensity of icing events. In this figure, the variables SLW, median volume diameter (MVD), air temperature and wind speed are derived from the simulation of the domain D3, and more precisely at the levels 21 m, 36 m, 57 m, 87 m and 128 m (Table 2.3). All the obtained data of this section correspond to the 114 significant icing days, with a frequency of one value each 10 min for each grid point of the total 200x200 grid points (domain D3). Since this study focuses on the range of temperatures below zero, only the data occurring within this range are considered.

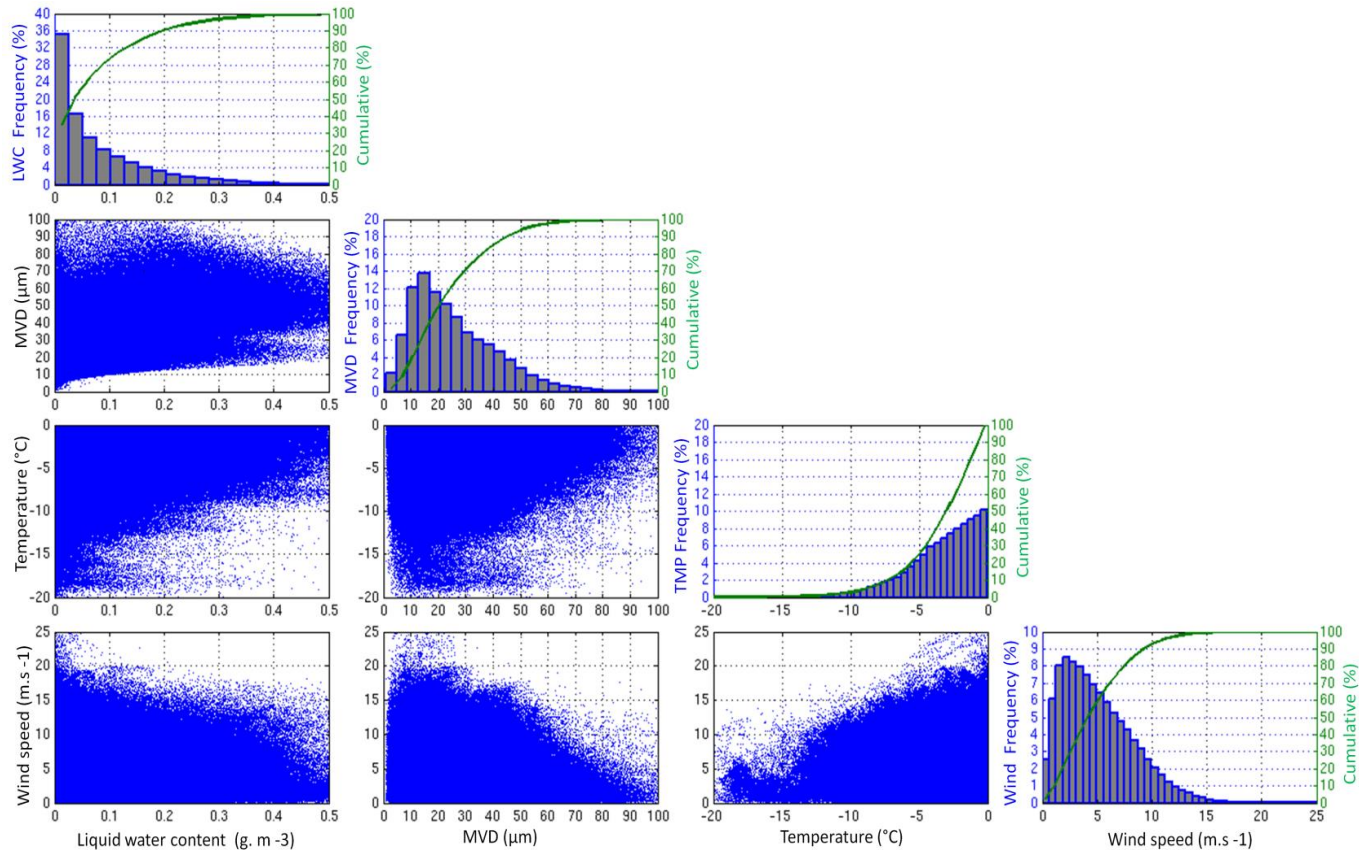


Figure 2.9. Statistics of meteorological icing parameters

The histogram and the cumulative sum of SLW indicate that smaller values of SLW that are less than 0.05 g m^{-3} are more frequent with a percentage that exceeds 50%. Moreover, SLW between 0.1 g m^{-3} and 0.3 g m^{-3} manifest a frequency of 30%. Statistically, SLW that are equal or greater than 0.4 g m^{-3} have insignificant frequency.

With respect to the obtained spectrum of MVD, the values around $15 \mu\text{m}$ take the lead in terms of frequency. In addition, within a relatively broader spectrum of MVD, the range of MVD between $10 \mu\text{m}$ and $20 \mu\text{m}$ appears with a frequency that exceeds 30% of the occurrences. Consequently, this finding demonstrates that the typical MVD that is associated with near surface supercooled clouds and icing events is approximately $15 \pm 5 \mu\text{m}$.

Small droplets with MVD less than 10 μm show a frequency around 18%. The frequency of MVD ranging from 30 μm to 50 μm is around 23%. Supercooled droplets with MVD larger than 50 μm are considered by the World Meteorological Organization as SLD. Due to their hazardous impact on structures; SLD has been studied with a particular intention. From this study, the frequency of SLD in Figure 2.9 indicates a percentage that exceeds 5%. Also, the whole spectrum of MVD is capped approximately by $\text{MVD} = 70 \mu\text{m}$.

In addition to the variables from cloud microphysics (SLW, MVD), the meteorological dynamic parameters (temperature and wind speed) are significantly influential in quantifying icing events. By taking into account the atmospheric layer considered in this section, the histogram of temperature reveals that the supercooled liquid cloud droplets occur exclusively between $-15 \text{ }^\circ\text{C}$ and $0 \text{ }^\circ\text{C}$. More specifically, the temperatures between $-5 \text{ }^\circ\text{C}$ and $0 \text{ }^\circ\text{C}$ encompass 75% of all occurrences, followed by the ranges $[-10 \text{ }^\circ\text{C}$ to $-5 \text{ }^\circ\text{C}]$ and $[-15 \text{ }^\circ\text{C}$ to $-10 \text{ }^\circ\text{C}]$ with approximate frequencies around 20% and 5% respectively. The histogram of the wind speed in Figure 2.9 indicates that over 50% have wind speeds below 5 m s^{-1} . Wind speeds ranging from 5 m s^{-1} to 10 m s^{-1} have a frequency of 30%. On the other hand 10% of the frequencies are assigned to the range between 10 m s^{-1} and 15 m s^{-1} . Furthermore, the corresponding weibull distribution to the wind speed histogram indicates a shape coefficient of 5.64 and a scale coefficient of 1.6. All values of wind speeds are capped at around 15 m s^{-1} .

2.3.7 Vertical profile of icing events climatology

In order to investigate the spatial distribution of the climatology of icing events and its vertical evolution along the atmospheric column, Figure 2.10 examines independently

the duration of icing events, ice accumulation, the frequency of occurrences of different severity classes of icing severity (Trace, Light, Moderate, Severe and Extreme), and corresponding topography.

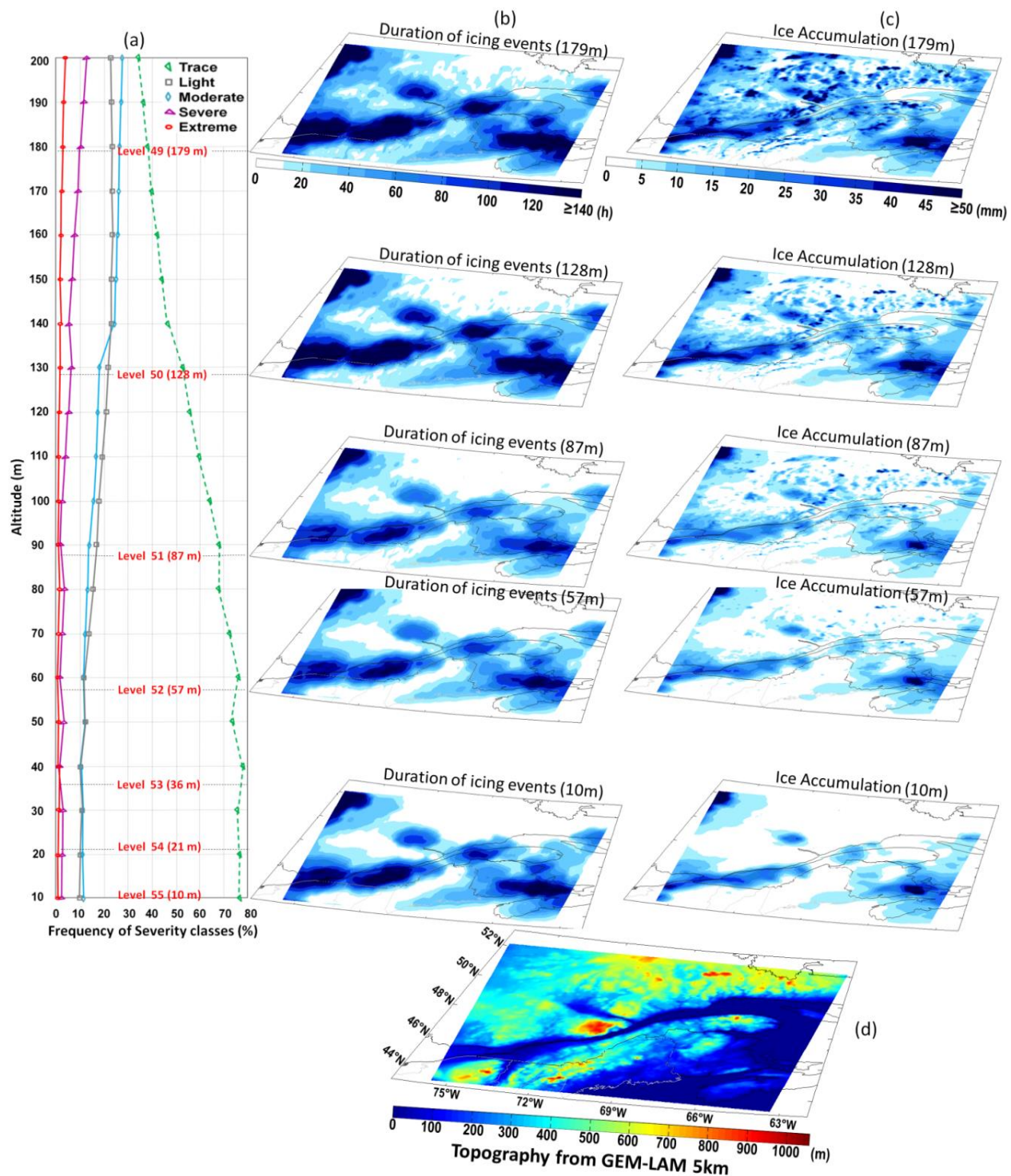


Figure 2.10. Vertical profiles of high resolution 15-year climatology of icing events: (a) severity classes (b) duration of icing events (c) ice accumulation (d) Topography from GEM-LAM5km

The results in this figure are derived from all points in the simulation of domain D3 for the significant days and from NARR (1000 mb) for the insignificant days. The results cover the time period of 15 years (1995-2009) and represent only GEM-LAM model levels (10 m, 57 m, 87 m, 128 m and 179 m). For the purpose of comparison, the duration of icing events and ice accumulation in Figure 2.10 are capped by 140 h and 50 mm respectively. The curves located in the left side of Figure 2.10 represent the percentage of the frequency of each icing severity class. From the interpolation of model levels, the occurrence frequency of each severity class is derived along the atmospheric layer from 10 m until 200 m with an interval of 10 m. The vertical distribution of icing results in Figure 2.10 reveals a disparity between the climatology profiles of the ice accumulation and the duration of icing events. The pattern of the duration of icing events indicates a steady behaviour without showing a significant variation along the studied atmospheric layer. On the other hand, toward higher elevations, the subfigures of the ice accumulation of each layer demonstrate a gradual intensification.

Lamraoui et al. (2013) have subdivided the intensity of icing events in 5 classes based on the accumulation rate. Therefore, regarding the frequency, Figure 2.10 (left side) introduces the vertical profiles of each of these classes. Within the lowest layer above ground between 10 m and 60 m, each of severity classes has a vertical profile of frequencies that are approximately steady, with values around 75% of Trace, 10% of Light and Moderate, between 2% and 3% of Severe and around 1% of extreme. Figure 2.10 indicates that Trace (weakest icing class) is the dominating class all along the atmospheric

layer between 10 m and 200 m. Starting at level of 60 m above ground, the class Trace decreases upward to reach 35% of the occurrences. Light and Moderate classes manifest an increase of frequency starting from level 60 m. On the other hand, the classes Severe and Extreme demonstrate increasing occurrences above 100 m. In this range of elevations and with different tendency of classes, Light and Moderate severities show increasing frequencies that reaches 23% and 27 % respectively, at the elevation of 200 m. Meanwhile, the severe and extreme classes start to manifest a different behaviour, only above the height of 100 m. Compared to previous classes, these intense classes increase slowly at higher elevations to reach 13 % and 4 % respectively, at the height of 200 m.

2.3.8 Icing severity index at fine scale resolution

This section discusses the advantages of using the mesoscale Model (GEM-LAM) with its advanced microphysics scheme on quantifying icing events, compared to the use of NARR. Therefore, to compare the results of these two data sources, Figure 2.11, illustrates the climatology of the ISI derived from (a) NARR data at 1000 mb and (b) GEM-LAM-5km at 1000 mb.

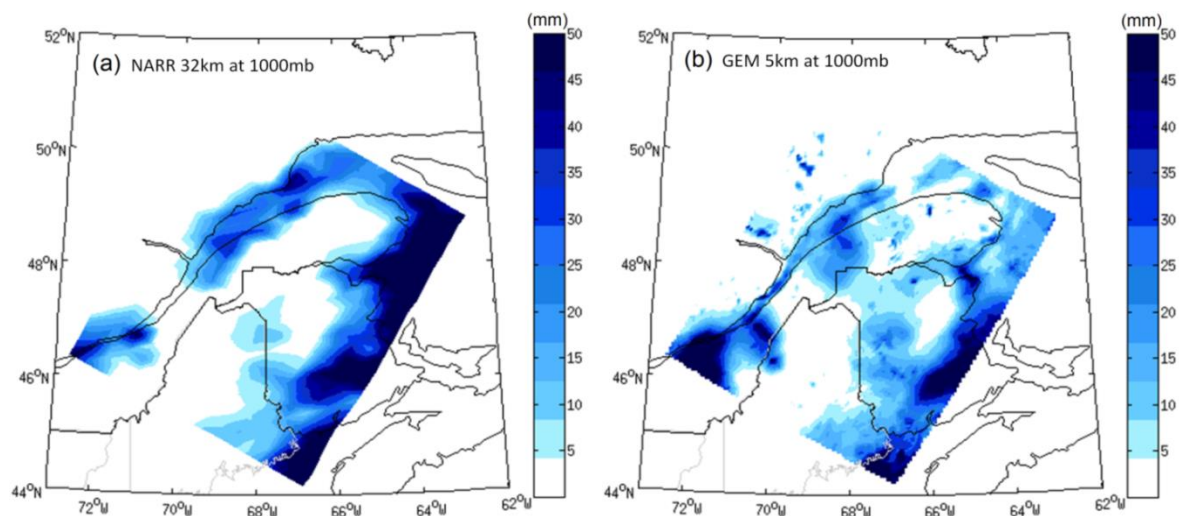


Figure 2.11. 15-year climatology of icing Severity Index at 1000 mb: (a) NARR 32 km, (b) GEM-LAM 5km

The two sub-figures in Figure 2.11 represent the same pressure level of 1000 mb. It is noticeable that Figure 2.11b reveals more details at smaller scale. Small areas of fine scale resolution that are shown in Figure 2.11b are mainly Continental and manifest a proportional response to the topography.

The small intense areas are located mainly in mountainous regions, such as in the Gaspé Peninsula. It is noticeable that Murdochville and its surroundings have an intense icing climate. Also an intense ISI extends along the mountain ridge from the National Park of Gaspésie until the Matane Wildlife Reserve.

On the west side of the St Lawrence River and more precisely in the North of the Saguenay region, a significant icing climate is marked over the National Park of Monts-Valin including the Monts-Valin themselves. Southward and between the region of Saguenay and Quebec City, the Laurentian Wildlife Reserve shows significant values of ISI.

Regions with very intense icing severity that occupy larger areas shown in Figure 2.11b are found mainly in the National Capital region, including the site of Mount-Bélair, followed by the region of Chaudière-Appalaches and the Lower St. Lawrence Region especially between Rimouski and Matane including Mont-Joli and continuing Southward to reach the north of the province of New Brunswick.

Moreover, both Figure 2.11a and b demonstrates that regions of the North-east and the centre of the province of New Brunswick manifest very high icing severities. However, 2.11b exclusively manifests a high icing severity which covers the Mount Carleton Provincial Park and its surroundings including the Mount-Carleton with its summit that exceeds 2600 ft, a zone that encompasses the Caribou Wind Park.

Besides Canadian regions, Figure 2.11b reveals a narrow zone with very localized and intense ISI in the state of Maine (USA) on the Mount Katahdin, the highest mountain in Maine with an elevation over 1600 m.

In order to target the wind industry, Figure 2.12 focuses on three critical levels above ground of ice accretion on a typical wind turbine with a hub of 80 m and tips of the blades in sweeping motion within the atmospheric layer between 40 m and 120 m. Therefore, this figure represents the climatologies of ice accumulation and duration of icing events at these levels. The accumulation and the duration of icing demonstrate that the level of 120 m contains the highest values.

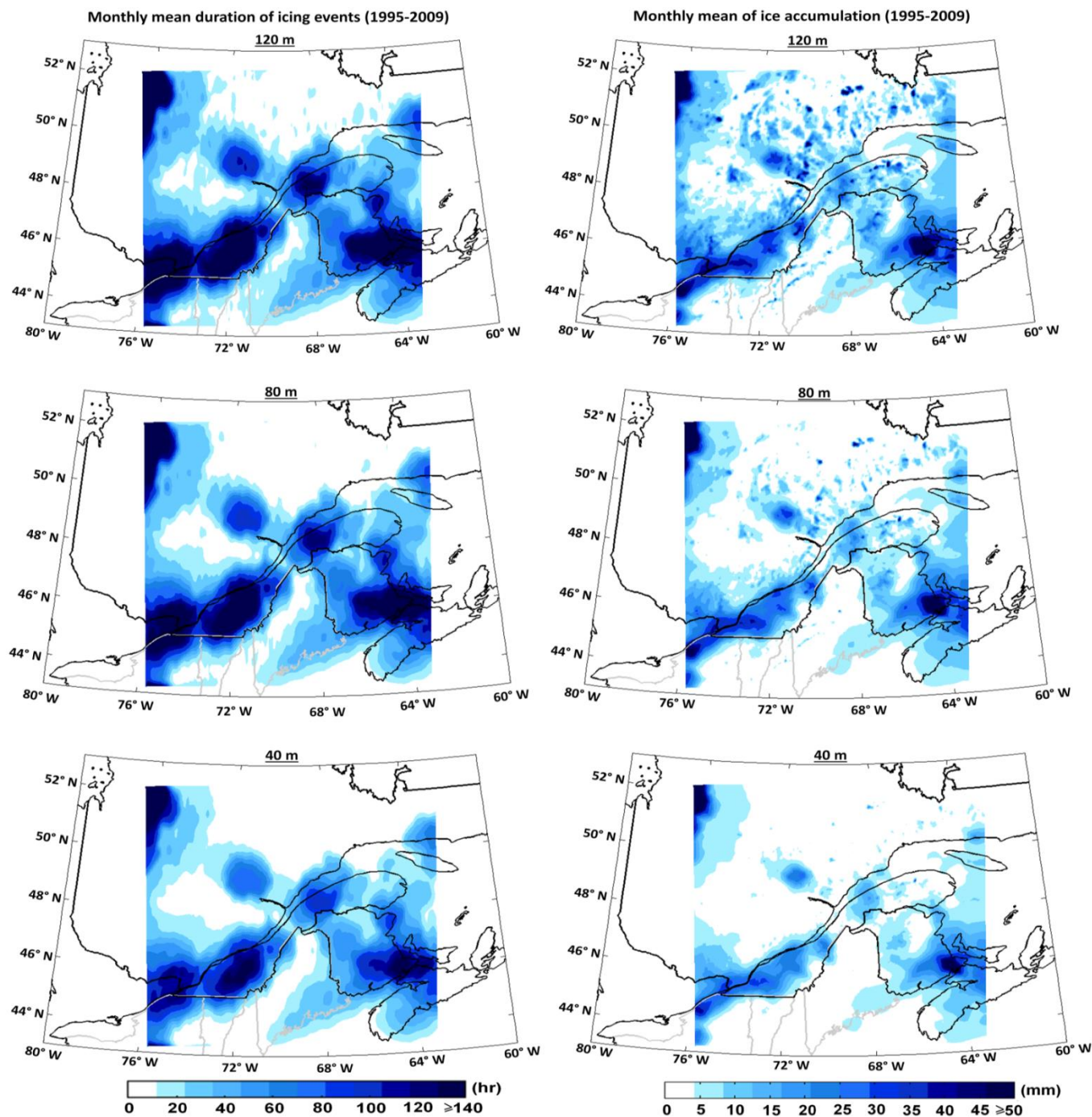


Figure 2.12. 15-year climatology of ice accumulation and duration of icing events at 40m, 80m and 120

The mapping in Figure 2.12 demonstrates higher response of ice accumulation to topography compared to duration of icing events which shows larger areas. With regard to

the duration of icing events, the peak values show persistence in all levels. Meanwhile, very localized zones with more elevated topography show an increase in ice accumulation at higher altitudes.

Figure 2.13 illustrates the vertical profile of the mean values of ice accumulation and duration of icing events at each level starting from 10 m to 200 m. This statistical estimation covers the entire D3 area and occupies an area of 1000x1000 km². Also, in Figure 2.13, the ice accumulation shows a gradual intensification toward higher elevations. On the other hand, the duration of event shows that increase only starting from the level of 60 m. The range of the mean values of ice accumulation vary from 6 mm at the level of 10 m to reach 17.2 mm at 200 m. On the other hand, the mean values of the duration of icing events is approximately 39 h below 60 m. Beyond the level of 60 m the duration increases to reach 61 h at 200 m.

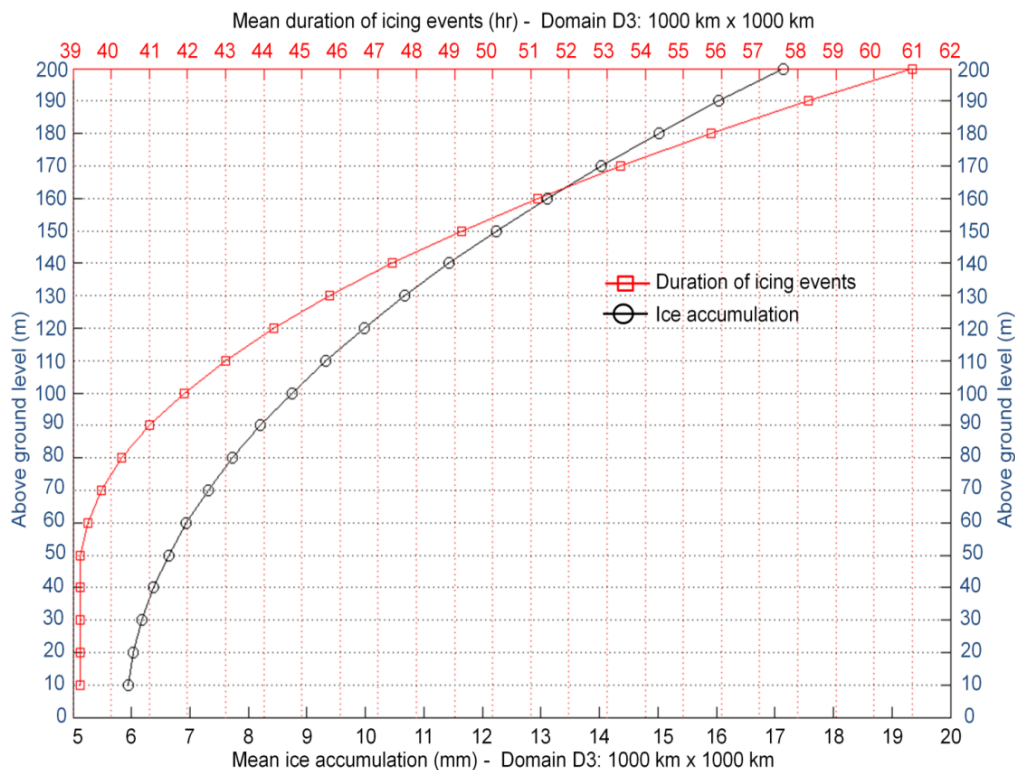


Figure 2.13. Vertical profiles of ice accumulation and duration of icing events between 10 and 200 m.

Following the presentation of results of the accumulation of ice and the duration of icing events, Figure 2.14 shows the climatology of the ISI during the 15-year time period from 1995 to 2010. The ISI combines the accumulation and duration by joining them with weighting factors that reflect the influence of the accumulation rate, the liquid water content and the duration of icing event, to assess the level of the severity of icing events. Given the typical operational height 80 m (Hub) of wind turbine, Figure 2.14 illustrates the ISI at that height.

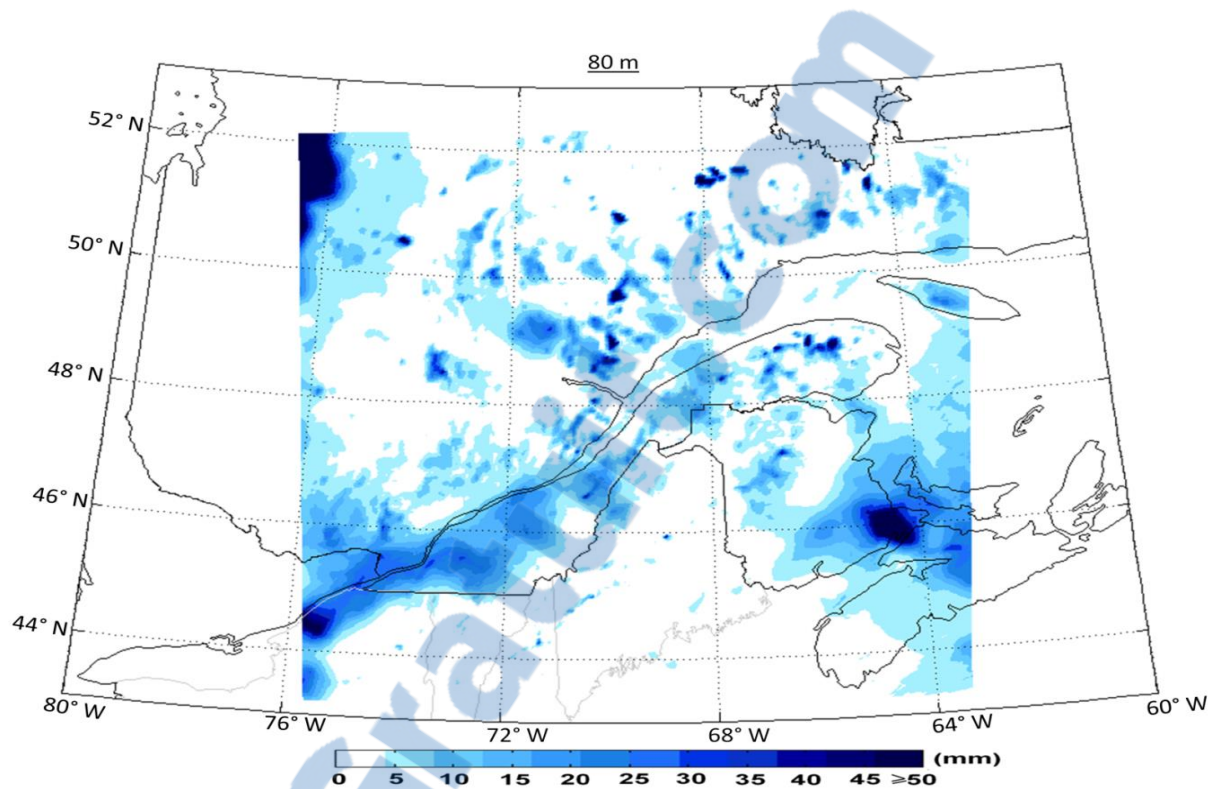


Figure 2.14. 15-year climatology of icing Severity Index at 80 m.

This map shows two categories of regions with extreme ISI; large areas and very localized areas. In reference to large areas, Figure 2.14 shows the region that extends from the Moncton area in New Brunswick to Amherst in Nova Scotia, the northern region of the state of New York between St. Lawrence River and the west of Adirondacks, The Montérégie area in Quebec, Chaudière-Appalaches, The north of lac St-Jean (Saguenay) and the large region that is located in the east of the James Bay. On the other hand, numerous small extreme areas are unevenly spread on the map and are mainly found in the Gaspé peninsula and northeast of the province of Quebec. Murdochville which is a typical complex field site indicates a very pronounced ISI. The Caribou wind park in the province of New Brunswick is definitely exposed frequently to severe icing events. Also, it is

noticeable that the mountainous regions of New York, Vermont, New Hampshire have high values of ISI, except for elevated areas between the Mt Washington and the Mt Kathadin (Maine).

2.4 Conclusion

The leading idea of this study is based on the identification of in-cloud icing events derived from non-precipitating supercooled cloud droplets by locating their occurrences, quantifying their intensities and then determining their durations. In order to achieve this goal, the present study utilized an original hybrid approach that provided fine resolution climate representations of icing events. In a previous study by the same authors the use of a 32-year time period (1979-2010) was applied to map the atmospheric icing severity. The current study was focused on the last 15 years of this time period, specifically from 1995 to 2009.

A statistical assessment showed that the month of January had an average of 7.6 icing days over the Gaspé Peninsula and its surroundings, including Eastern New Brunswick. The use of NARR data indicated a limitation in capturing icing events over complex terrains. Therefore, the involvement of finer scale modeling is crucial for adequate representation of atmospheric phenomena, particularly near the surface. The simulations are driven by NARR data and implicate the use of a limited-area version of GEM model with multi-nested domains that have spatial resolutions of 10 km and 5 km and temporal resolutions of 300 s and 60 s respectively.

The simulations of GEM-LAM for the entire 15-year time period are very time

consuming, therefore this study implicated a hybrid approach that involved only the significant icing days in the GEM-LAM calculations. In turn, icing calculations for the non-significant icing days in this time period used data directly from NARR. Consequently, the final product represents the entire 15 years period (1995-2009) with finer scale resolution details of icing events. In addition, since NARR data is not directly compatible for the use of GEM model, conversion tools (projection, format) were created to meet the operational requirements of GEM-LAM.

The findings of this study during the significant icing days revealed typical supercooled droplet sizes associated with near-surface icing events with 30% of MVD around $15 \mu\text{m} \pm 5 \mu\text{m}$ and 5% of supercooled large droplets ($\text{MVD} > 50 \mu\text{m}$). Furthermore, the temperature range is mainly dominated by values between -5°C and 0°C , which represent 75% of occurrences. Ultimately, with the use of an original strategy, this study explored the icing events at fine scale resolution and in three dimensions. The results indicated the importance of the altitudes 60 m and 100 m that mark substantial transitions in the vertical profile of the severity classes. Moreover, toward higher elevations, the duration of icing events and the ice accumulation indicated higher values at higher elevations. Conclusively, the data at fine scale resolution contributes significantly in revealing more details of orographic clouds and condensation that lead to larger cloud droplet sizes and consequently more ice accumulation.

2.5 References

- Ahrens, C.D., 2007. *Meteorology Today: An Introduction to Weather, Climate, and the Environment*, 8th ed. Thomson Brooks/Cole, Belmont, CA 537.
- Bennartz, R., Shupe, M. D., Turner, D. D., Walden, V. P., Steffen, K., Cox, C. J., Kulie, M. S., Miller, N. B. and Pettersen, C., 2013. July 2012 Greenland melt extent enhanced by low-level liquid clouds. *Nature*. 496, 83-6.
- Bernstein, B.C., Tiffany, A., Omeron, A., Politovich, M.K. and McDonough, F., 1998. Surface weather features associated with freezing precipitation and severe in-flight aircraft icing. *J. Atmos. Res.* 46, 57–73.
- Bernstein, B.C., Ratvasky, T.P., Miller, D.R. and McDonough, F., 2000. Freezing Rain as an In-Flight Icing Hazard. (NASA TM-2000-210058, June 2000).
- Bernstein, B.C., Wolff, C.A. and McDonough, F., 2007. An inferred climatology of Icing conditions aloft, including supercooled large drops. Part I: Canada and the Continental United States. *J. Appl. Meteor. Climatol.* 46, 1857–1878.
- Boudala, F. S., Isaac, G. A., Cober, S. G. and Fu, Q., 2004. Liquid fraction in stratiform mixed-phase clouds from in situ observations. *Q. J. R. Meteorol. Soc.* 130, 2919-2931.
- Byrkjedal., Ø., 2013. Icing map of Sweden, (Winterwind, Östersund, 12.02.2013)
- Camion, A., 2012. La modélisation des événements de givre atmosphérique: Interpolation de la NARR pour l'utilisation de GEM. (MSc thesis). University of Quebec, École de Technologie Supérieure, 255.
- Carrière, J.M., Lainard, C., Le Bot, C. and Robart, F., 2000. A climatological study of surface freezing precipitation in Europe. *Meteorol. Appl.* 7, 229–238.
- Cober, S.G., Isaac, G.A., Strapp, J.W., 2001. Characterizations of Aircraft Icing Environments that Include Supercooled Large Drops. *J. Appl. Meteor.* 40, 1984–2002.
- Cortinas, J.V; Bernstein, B.C; Robbins, C.C. and Strapp, J.W. 2004. An analysis of freezing rain, freezing drizzle, and ice pellets across the United States and Canada: 1976-90. *Weather and Forecast.* 19 (2) 377-390
- Debenedetti, P.G., 1996. *Metastable Liquids: Concepts and Principles*. Princeton University Press, Princeton, NJ (400 pp.).
- Dee, D.P., Uppala, S.M., Simmons, A.J., Berrisford, P., Poli, P., Kobayashi, S. and Andrae, U., Balsameda, M.A., Balsamo, G., Bauer, P., et al., 2011. The ERA-Interim reanalysis:

- configuration and performance of the data assimilation system. *Q. J. R. Meteorol. Soc.* 137, 553–597.
- Drage, M.A. and Hauge, G., 2008. Atmospheric icing in a coastal mountainous terrain. Measurements and numerical simulations, a case study. *Cold Reg. Sci. Technol.* 53(2), 150-161.
- Fernández-González S., Valero F., Sánchez J.L., Gascón E., López L., García-Ortega E. and Merino A., 2014. Observation of a Freezing Drizzle Episode: A Case Study. *Atmos. Res.* 149, 244-254.
- Fikke, S.M., 2005. Modern meteorology and atmospheric icing. In: *Proc 11th IWAIS*, Montreal, Canada. June 2005. Paper IW73.
- Heymsfield, A. J., Miloshevich, L. M., Slingo, A., Sassen, K. and Starr, D. O. C., 1991. An Observational and Theoretical-Study of Highly Supercooled Altocumulus. *J. Atmos. Sci.* 48, 923-945.
- Illingworth, A.J., Hogan, R.J., O'Connor, E.J., Bouniol, D., Brooks, M.E., Delanoë, J., Donovan, D.P., Eastment, J.D., Gaussiat, N., Goddard, J.W.F., et al., 2007. Cloudnet—Continuous evaluation of cloud profiles in seven operational models using ground-based observations. *Bull. Am. Meteorol. Soc.* 88, 883–898.
- Jacobson, M.Z., 2005. *Fundamentals of Atmospheric Modeling*. Cambridge University Press, Cambridge (813 pp.).
- Korolev, A. V. and Isaac, G. A., 2000. Drop growth due to high supersaturation caused by isobaric mixing. *J. Atmos. Sci.* 57, 1675–1685.
- Laakso, T., Baring-Gould, I., Durstewitz, M., Horbaty, R., Lacroix, A., Peltola, E., Ronsten, G. and Tallhaug, L., T., Wallenius, 2010. State-of-the-art of wind energy in cold climates, In : *Work. Pap.* 152, VTT Tech. Res. Cent. of Finl., Esbo, Finland.
- Laflamme, J., 1993. Spatial variation of extreme values in the case of freezing rain icing. In : *Proc 6th IWAIS, Budapest, Hongrie*, 19–23.
- Lamraoui, F., Fortin, G., Benoit, R., Perron, J., and Masson, C., 2013. Atmospheric icing severity: Quantification and mapping. *Atmos. Res.* 128, 57–75.
- Lamraoui, F., Fortin, G., Benoit, R., Perron, J., and Masson, C., 2014. Atmospheric icing impact on wind turbine production. *Cold Reg. Sci. Technol.* 100, 36–49.
- Lasher-Trapp, S., Anderson-Bereznicki, S., Shackelford, A., Twohy, C.H. and Hudson, J. G., 2008. An Investigation of the Influence of Droplet Number Concentration and Giant

Aerosol Particles upon Supercooled Large Drop Formation in Wintertime Stratiform Clouds. *J. Appl. Meteor. Climatol.* 47, 2659-2678.

Lau, K. M. and Wu, H. T., Warm rain processes over tropical oceans and climate implications. *Geophys. res. lett.*, 30, 2003, <http://dx.doi.org/10.1029/2003GL018567>.

Marwitz, J. D., Politovich, M., Bernstein, B., Ralph, F., Neiman, P., Ashenden, R. and Bresch, J., 1997. Meteorological conditions associated with the ATR72 aircraft accident near Roselawn, Indiana, on 31 October 1994. *Bull. Am. Meteorol. Soc.* 78, 41–52.

Milbrandt, J. and Yau, M. K., 2005, A multi-moment bulk microphysics parameterization, part I: Analysis of the role of the spectral shape parameter, *J. Atmos. Sci.* 62, 3051–3064.

Morrison, H., de Boer, G., Feingold, G., Harrington, J., Shupe, M.D. and Sulia, K., 2011. Resilience of persistent Arctic mixed-phase clouds. *Nat. Geosci.* 5, 11-17.

Murakami, M., Yamada, Y., Matsuo, T. Mizuno, H. and Morikawa, K., 1992. Microphysical structures of warm-frontal clouds. The 20 June 1987 case study. *J. Meteor. Soc. Japan.* 70, 877–895.

Pobanz, B.M., Marwitz, J.D. and Politovich, M., 1994. Conditions associated with large-drop regions. *J. Appl. Meteor. Climatol.* 33, 1366-1372

Politovich, M K., 1989 Aircraft Icing Caused by Large Supercooled Droplets, *J. Appl. Meteor. Climatol.* 28, 856-868.

Politovich, M.K.,1996. Response of a research aircraft to icing and evaluation of severity indices. *J. Aircraft.* 33, 291–297.

Prescornic, D., 2014. Modélisation méso-échelle d'événements de précipitation givrante pour un parc éolien. MSc Thesis . University of Quebec, École de Technologie Supérieure. pp 255

Pruppacher, H.R. and Klett, J.D. 2010. Microphysics of Clouds and Precipitation. Atmospheric and Oceanographic Sciences Library, Vol. 18. 2nd ed. (976 pp.).

Rasmussen, R. M., Bernstein, B. C., Murakami, M., Stossmeister, G., Reisner, J. and Stankov, B., 1995. The 1990 Valentine's Day Arctic outbreak. Part I: Mesoscale and microscale structure and evolution of a Colorado Front Range shallow upslope cloud. *J. Appl. Meteor.* 34, 1481–1511.

Rock, P.A., 2003. Chemical Thermodynamics, University Science Books, USA (548 pp.).

Sand, W. R., Cooper, W. A., Politovich, M. K. and Veal, D. L., 1984. Icing conditions encountered by a research aircraft. *J. Climate Appl. Meteor.* 23, 1427–1440.

- Schemenauer, R.S. and Cereceda, P., 1994. A Proposed Standard Fog Collector for Use in High-Elevation Regions. *J. Appl. Meteor. Climatol.* 33 (11), 1313-1322.
- Shin, J., Berkowitz, B., Chen, H. and Cebeci, T., 1991. Prediction of ice shapes and their effect on airfoil performance. *AIAA 29th Aerospace Sciences Meeting, Reno, NV, Paper AIAA-91-0264*, 21 pp.
- Shupe, M. D., 2011. Clouds at Arctic atmospheric observatories. Part II: Thermodynamic phase characteristics. *J. Appl. Meteor. Climatol.* 50, 645–661.
- Stuart, R.A. and Isaac, G.A., 1999. Freezing precipitation in Canada. *Atmosphere-Ocean* 37–1, 87–102.
- Turner, D.D., 2005. Arctic Mixed-Phase Cloud Properties from AERI Lidar Observations: Algorithm and Results from SHEBA. *J. Appl. Meteor. Climatol.* 44(4), 427-444.
- Yang, J., Jones, K. F., Yu, W. and Morris, R., 2012. Simulation of in-cloud icing events on Mount Washington with the GEM-LAM, *J. Geophys. Res.*, 117, D17204.

CHAPTER 3

ATMOSPHERIC ICING IMPACT ON WIND TURBINE PRODUCTION

*This Chapter is published in the form of an original scientific article
in the journal of
Cold Regions Science and Technology, 2014, vol 100, p. 36-49*

dx.doi.org/10.1016/j.coldregions.2013.12.008

Fayçal Lamraoui ^{1*}, Guy Fortin ², Jean Perron ¹, Robert Benoit ³, Christian Masson ³

¹ *The Anti-Icing Materials International Laboratory, University of Quebec at Chicoutimi*

² *Bombardier Aerospace*

³ *École de technologie supérieure, University of Quebec*

* Corresponding Author address:

Fayçal Lamraoui

*The Anti-Icing Materials International Laboratory, University of Quebec at Chicoutimi
555, boulevard de l'Université, Chicoutimi, QC, G7H 2B1 Canada*

Email: faycal.lamraoui@gmail.com

3. ATMOSPHERIC ICING IMPACT ON WIND TURBINE PRODUCTION

Abstract

Wind turbine performance depends mainly on the wind speed and aerodynamics of blades. The roughness generated from ice accretion can significantly reduce the aerodynamics and consequently the power production of the wind turbine. This study locates the glaze and rime ice on the blade, to detect the critical zones involved in significant power production loss. On the blade, the distribution of the elementary power production as well as the type and thickness of the accreted ice are inconsistent. Under icing conditions, the outer section of the blade starting from the radial position $r/R=0.8$ contribute significantly to the blades aerodynamics. The freezing fraction is unevenly distributed; since it initially forms rime ice near the root and then glaze toward the tip of the blade. The critical freezing fraction 0.88 associated with the double horn ice shape is spatially limited and occupies a restricted segment on the blade and gradually moves towards the tip with decreasing temperature. With the use of power degradation analogy with sub-scaled rotor blades of a helicopter under icing conditions, a power loss factor is introduced to quantify and locate power loss along the blades of wind turbines. The study is based on four values of liquid water content that delineate five classes of icing severity. Including power loss factor, the most significant power loss that corresponds to freezing fraction 0.88 is found to be located at $r/R \sim [0.93 \ 0.96]$ which corresponds to $T = -2.6 \text{ }^\circ\text{C}$, $-4.5 \text{ }^\circ\text{C}$, $-12 \text{ }^\circ\text{C}$, and $-20 \text{ }^\circ\text{C}$ and for liquid water content $\text{LWC}=0.04 \text{ g}\cdot\text{m}^{-3}$, $0.07 \text{ g}\cdot\text{m}^{-3}$, $0.2 \text{ g}\cdot\text{m}^{-3}$, and $0.36 \text{ g}\cdot\text{m}^{-3}$ respectively. The resulted power degradation can reach a maximum of 40%. Locally it is the shape rather than the thickness of ice that causes more power loss; meanwhile when considering the whole blade, power degradation is controlled mainly by ice thickness regardless of the type of ice. The results obtained can help the setup of a sensor that triggers the ice-protection system upon detection of critical freezing fraction.

.Keywords: Ice accretion, Wind turbine, Re-analysis, Atmospheric icing climatology

3.1 Introduction

Numerous cold climate countries already utilize and will progressively make more use of wind energy, because of their propitious high wind potential. Cold climate regions represent an unavoidable beneficial environment for wind energy. For this reason and in order to maintain maximum extraction of power production, wind turbine manufacturers including blade's airfoil designers are required to accommodate the hazardous conditions of atmospheric icing events. Cold regions with higher altitudes represent the best sites for wind farms; wind speed increases approximately by $0.1 \text{ m}\cdot\text{s}^{-1}$ each 100 m of altitude within the first 1000 m (Parent and Ilinca, 2011). Colder regions are characterized by a potential of wind power 10% higher than other regions, because of their higher air density. Since cold air is denser than warm air, it increases the kinetic energy of wind which leads to further power production of wind turbine (Fortin et al., 2005). Commonly wind turbine farms are located in coastal or mountainous areas; these regions are exposed frequently to icing events during the cold seasons (Tammelin and Säntti, 1998). Besides freezing precipitation, low-level stratus clouds at subzero temperatures and more specifically fog cause serious challenges to land, air and sea transportation, and greatly affect the wind turbine industry (Bendix et al., 2005). Ice accretion on the blade of a wind turbine reshapes the blade airfoil and affects negatively its aerodynamic properties. The damaging effect of atmospheric icing on wind turbine production is not limited to severe icing events and high amount of ice accretion; even small amounts of ice on the leading edge of the blade degrades drastically its aerodynamic characteristics and consequently the expected electric power (Jasinski et al., 1998; Marjaniemi and Peltola, 1998). Furthermore, icing events affect wind

assessment and the performance of wind farms by generating measurement errors, power losses, premature mechanical failures, electrical failure and safety hazards (Parent and Ilinca, 2011; Seifert et al., 2003). Besides load asymmetry, vibration and safety hazards, certain icing conditions may cause significant economic losses for the wind turbines industry.

The occurrences of severe icing events necessitate setting the wind turbine on non-operational mode in order to minimize ice accretion and its aerodynamic effects. In general, without the de-icing or the anti-icing procedures, ice accretion on the blades remains for a significantly longer period than duration the icing event itself (Laakso et al., 2010). Bose and Rong (1990) demonstrated that even a vestige of roughness generated from the smallest ice accretion on a wind turbine blade will weaken the expected wind energy by up to 20%. More precisely, wind energy that is weakened by ice accumulation and duration of icing events encounter power losses that range between 0.005% and 50% of the annual production (Botta et al., 1998; Laakso and Peltola, 2005; Tammelin and Säntti, 1996). An experimental study achieved by Antikainen and Peuranen (2000) on wind turbine blades showed that icing events that last at least a few hours, generate a mass and aerodynamic unbalance. Furthermore, in case this asymmetrical state persists for a long period (days or weeks), the power production and turbine lifetime drop considerably. A costly anti-icing strategy is used to minimize icing effects; however it is not a practical solution for icing concerns since this strategy can consume approximately 25% of the energy produced by the wind turbine (Makkonen and Autti, 1991). Previous studies have looked at wind turbine aerodynamics and performance degradations. The investigations and analysis involved the

different effects of rime and glaze (Hochart et al., 2008), by analyzing ice accretion effects on lift to drag ratio (Hochart et al., 2008; Jasinski et al., 1998) and power degradation (Dierer et al., 2009; Jasinski et al., 1998). Hochart et al. (2008) analyzed in-fog icing measurements from the Murdochville wind farm in the Gaspé Peninsula (Canada). The study revealed a significant torque reduction located on the outer third of the blades. In order to counterbalance the icing effect on the blade, the active heating system on the blade represents an effective solution (Parent and Ilinca, 2011) that needs further devoted research to lower its cost. Under icing conditions, Dierer et al. (2009) indicated that the anti-icing heating system reduces the loss of the annual power production 3.5 %, compared to 10 % of annual loss without a heating system. Also, under rime conditions, Jasinski et al. (1998) demonstrated that the performance loss of wind turbine can reach 20 %. In attempting to assess the long term severity of atmospheric icing for wind turbines,

Lamraoui et al. (2013) presented the climatology of icing severity for wind turbines, using 32 years (1979–2010) of meteorological data extracted from the North American Regional Reanalysis (NARR). In general, the severity assessment of icing event depends on the field of application and the targeted problem being considered. The icing severity index introduced by Lamraoui et al. (2013) represents the varying degrees of icing severity that combine different threat factors by weighting each according to a scale of seriousness.

In collaboration with Bell Helicopter, Fortin and Perron (2009) performed an experimental study based on a spinning rotor blade developed at the Anti-icing Materials International Laboratory.

The objective of that study is to investigate ice physics, low energy de-icing system and ice-phobic coatings for small helicopters. Compared to a clean blade, the power required to rotate an iced blade increases with decreasing air temperature until reaching its maximum at about 5200 W that corresponds to a critical freezing fraction of 0.88. This critical value is associated with the formation of a double horn ice shape. Beyond the maximum of 5200 W, the required power decreases with decreasing air temperature to reach its minimum at about 1200 W. This minimum power occurs when the blades are clean without ice accretion. The effect of air temperature on power is due to the ice shape change with the freezing fraction which in turn depends on air temperature and liquid water content. The partial freezing of water initiates a water runback that freezes afterward, causing an airfoil reshape and aerodynamic degradation. With the use of the results of Fortin and Perron (2009), the present study focuses on identifying crucial parameters that control the type of ice accretion on the blades of a wind turbine which causes high power loss such as: Freezing fraction, liquid water content, temperature, and the critical radial position on the blade. Typical values of icing events were extracted and calculated from NARR data during a time period of 32 years. The current paper also investigates and attempts to estimate the contribution of each localized zone along the blade of the wind turbine to power losses that occur under different icing conditions.

3.2 Methodology

The models used for the current study attempt to involve more relevant parameters, in order to improve the assessment of the severity of icing events, and more specifically the production loss of wind turbines caused by ice accretion. In addition to the liquid water content and the duration of icing events for different icing severity classes involved in the quantification and the assessment of the icing severity index (Lamraoui et al., 2013), the present study focuses on exploring the aerodynamic degradation distribution along the blade, under different meteorological conditions and geometries of the blades. In order to cover a typical range of liquid water contents and various severity classes (Fikke et al., 2006; Lamraoui et al., 2013), the values of LWC $0.04 \text{ g}\cdot\text{m}^{-3}$ (light), $0.07 \text{ g}\cdot\text{m}^{-3}$ (moderate), $0.2 \text{ g}\cdot\text{m}^{-3}$ (severe), $0.36 \text{ g}\cdot\text{m}^{-3}$ (extreme) were considered for ice calculation. Under icing conditions, the distribution of the electric energy production along an optimal blade design was calculated, in order to locate the critical position on the blade that causes the highest power loss during icing events. The use of ice accretion and power loss models with different values of meteorological and geometric parameters enables the exploration to help locate the aerodynamic and mechanical effects along the blade. Several studies (Hochart et al., 2008; Lamraoui et al., 2013) have associated the value of liquid water content $0.2 \text{ g}\cdot\text{m}^{-3}$ to representative occurrences of atmospheric icing over Murdochville, and to the average of maximum values during winter months over Mount Bélair (Canada). Therefore, a particular intention was given to production losses that are associated this typically assumed liquid water content. Unlike helicopters that require power to rotate, wind turbines rotate to provide power. Due to the lack of studies that investigate the impact of freezing fraction on

wind turbines production, the effect of freezing fraction on power requirements for helicopter is projected on wind turbine power production. To begin, this study identifies the critical location which corresponds to the most aerodynamically hazardous freezing fraction (Fortin and Perron, 2009) on the blade that holds the maximum power loss. Then, the corresponding temperatures for typical liquid water contents are determined, and finally power loss is evaluated (Fortin and Perron, 2009).

3.2.1 Generic wind turbine

The investigation was carried out on a generic horizontal axis wind turbine which is based on V80-1.8 MW Vestas characteristics. This type of wind turbine is commonly used in the province of Quebec (Canada). This wind turbine is characterized by a diameter of 80 m and a rated power of 1.8 MW that corresponds to a rated wind speed of $14 \text{ m}\cdot\text{s}^{-1}$. The minimum wind speed at which the wind turbine starts to be operational is $4 \text{ m}\cdot\text{s}^{-1}$. The blades have a variable pitch angle that corresponds to prevailing winds. The wind turbine rotates at approximately 16 rpm (Vestas).

3.2.2 Blade

The generic blades have a radius of 40 m and are designed to provide more power and to minimize mechanical strains and sound. Since the blade design with more efficiency is complex and costly, a simplified alternative that represents a linear variation of the chord along the span was suggested (Burton et al., 2001).

3.2.3 Chord

As shown in Figure 3.1, at 5m away from the hub and along the span, the chord starts with the longest value of 3.5 m and it decreases linearly along the span until reaching

its minimum value of 0.5 m at the tip of the blade. The length of the chord along the span was determined based on Eq. (1). x [m] is the position along the span that varies from 5 m to 40 m.

$$c = 3.5 + \left(\frac{3}{35}\right) \cdot (5 - x) \quad (1)$$

The first 5 m from the hub of the blade are not considered because of the cylindrical shape and its insignificant contribution to power production.

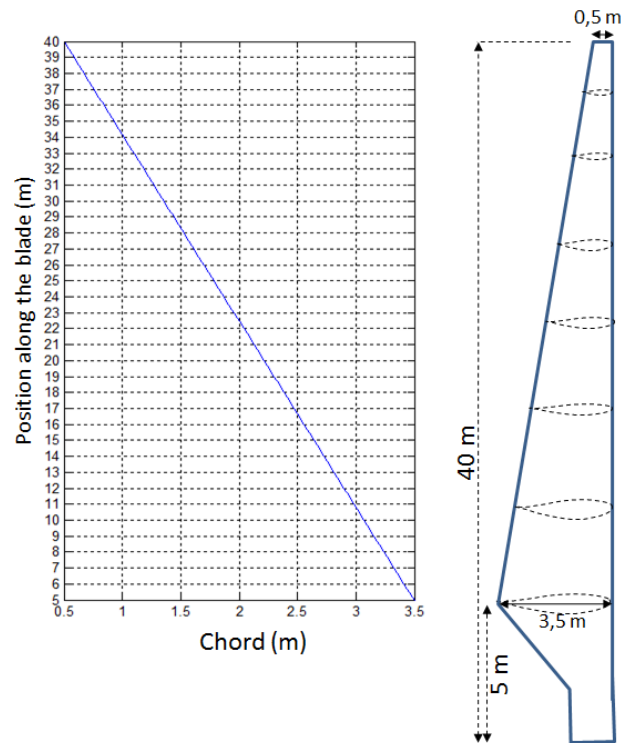


Figure 3.1. Chord variation along the span

3.2.4 Airfoil

In order to substitute NACA 44xx airfoil, Danish wind turbine designers started to use NACA 63(2)-xx airfoils that showed a reduced sensitivity to leading edge roughness.

According to Abbot and von Doenhoff (1959) and Hansen (2008), wind turbine blades are often designed with a profile having similar characteristics to NACA 63–415 airfoil due to its stall characteristics. The roughness that is caused by dirt and insect accumulation can decrease the power output up to 40% (Manwell et al., 2009). The leading edge is considered the zone on the blade that has the highest sensitivity to surface roughness (Jacobs, 1932; Jones and Williams, 1936). With regard to NACA 63–415 airfoil, Figure 2.2 illustrates a ratio of 0.024 that compares the diameter of a cylinder at the leading edge to the chord of the airfoil.

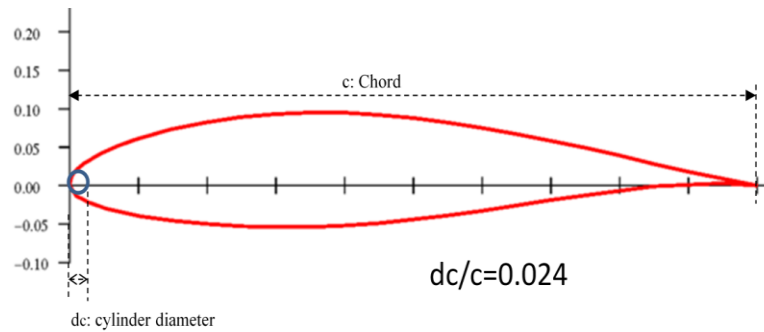


Figure 3.2. NACA 63-415 airfoil

3.2.5 Speed

The rotational motion of the blade's shaft at 16 rpm makes the blade's speed vary from its maximum at the tip decreasing to its minimum towards the center, as illustrated in Eq. (2). The speed U [$\text{m}\cdot\text{s}^{-1}$] depends on the position x [m] along the span that varies from 5 m to 40 m and the rotational speed Ω .

$$U = (5 + x) \cdot \Omega \cdot \frac{2\pi}{60} \quad (2)$$

3.3 Ice accretion model

The calculation of ice accretion was based on the collection of liquid water that freezes upon contact with a cylindrical object (Messinger, 1953). Eq. (3) represents the collected water mass rate of liquid water per unit surface on a cylinder.

$$\dot{M}'' = E \cdot LWC \cdot U \quad (2)$$

The collected water mass rate per unit surface \dot{M}'' [$\text{g} \cdot \text{m}^{-2} \cdot \text{s}^{-1}$] depends on the liquid water content LWC [$\text{g} \cdot \text{m}^{-3}$], the wind speed U [$\text{m} \cdot \text{s}^{-1}$] and collection efficiency E .

The total collection efficiency E is based on Eq. (4) (Walton and Woolcock, 1960).

$$E = \frac{St^2}{(St+0.7)^2} \quad (4)$$

St is the Stokes number (Eq. (5))

$$St = \frac{U \cdot MVD^2 \cdot \rho_w}{9 \cdot \mu_a \cdot d_c} \quad (5)$$

U [$\text{m} \cdot \text{s}^{-1}$] is the wind speed, MVD [μm] represents the cloud droplet medium volume diameter, ρ_w is the water density in [$\text{kg} \cdot \text{m}^{-3}$] while d_c represents the cylinder diameter and μ_a [$\text{Pa} \cdot \text{s}$] is the dynamic viscosity of air which is calculated using Clift's empirical correlation (Brodkey and Hershey, 1988). Since winter stratiform clouds near ground typically are characterized with a medium volume diameter between 15 μm and 20 μm (Cober et al., 1995; Isaac, 1991), therefore the medium volume diameter (MVD) used in this study is considered to be 18 μm (Lamraoui et al., 2013). From the Eq. (1), the ice thickness rate that indicates the accumulated ice on a cylinder is represented in Eq. (6).

$$\dot{e} = E \cdot SLWC \cdot U \cdot F / \rho_{ice} \quad (6)$$

SLWC [$\text{g}\cdot\text{m}^{-3}$] is the supercooled liquid water content, ρ_{ice} [$\text{kg}\cdot\text{m}^{-3}$] is the ice density which is implicated in quantifying ice thickness. It was calculated using Laforte ice density (Laforte and Allaire, 1992). F represents the freezing fraction, in regard to rime ice, all the supercooled water collected freezes at impact; but for glaze ice, only a fraction of supercooled water freezes at impact (Mazin et al., 2001; Messinger, 1953).

3.4 Power distribution model

In order to determine the power distribution along the span, a generic blade design was considered. The estimated elementary power coefficient is defined within an elementary span dr as shown in Figure 3.3 (Burton et al., 2001; Manwell et al., 2009).

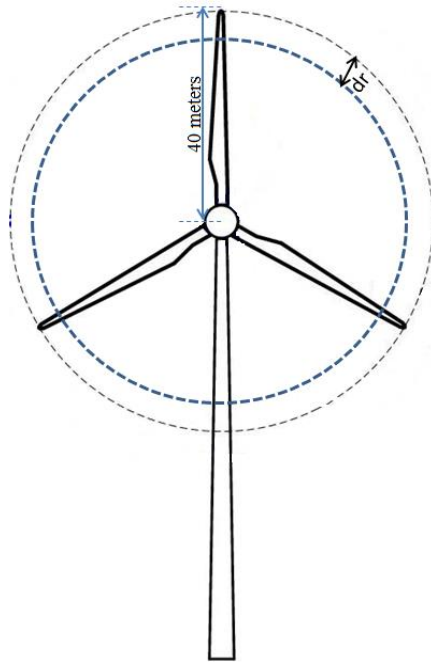


Figure 3.3. Elementary span of wind turbine

The rotor power coefficient is dependent to the tip speed ratio λ and the axial and tangential flow induction factors a and \acute{a} .

$$\lambda = \frac{\Omega R}{V_\infty} \quad (7)$$

After an analytical demonstration, the resulted Eq. (8) reveals a linear increasing behavior of C_p along the span which reaches the maximum at $r = R$.

$$\frac{dC_p}{dr/R} \approx m \left(\frac{r}{R} \right) \quad (8)$$

From Eq. (8), the elementary power coefficient ΔC_p can be written as illustrated in Eqs. (11) to (14).

$$C_p = \int_{r_a/R}^{r_b/R} dC_p \, dr/R \quad (9)$$

$$C_p = m \int_{r_a/R}^{r_b/R} dr/R \quad (10)$$

Consequently, the variation of the elementary power coefficient ΔC_p that corresponds to an elementary span $(r_b - r_a)/R$ which is located between r_b and r_a is concluded by Eq. (11).

$$C_p = \frac{mr}{R^2} \left(\frac{r_b + r_a}{2} \right) \quad (11)$$

Knowing that m represents the slope, the total Power coefficient is $C_p = m/2$.

Also $\frac{r_b + r_a}{2}$: represent the center of the elementary area on the span.

The elementary percentage of power coefficient in each elementary division dr along the blade is calculated using the Eq. (12).

$$C_p = \frac{2}{N_{elem}} \left(\frac{r}{R} \right)_{elem} \quad (12)$$

The present study investigates the effects of atmospheric icing on wind turbine blades through the quantification and the identification of ice types on the blades, therefore assessing the loss of energy along the blade.

3.5 Results

3.5.1 Power along the blade

The power production is proportional to wind speed which initiates the rotation of the blades. The uneven distribution of relative velocity along the blade generates inconstant elementary distribution of power. Using Eqs. (12) and (20), Figure 3.4 illustrates a linear increase of power coefficient starting from the root of the blade to the tip. The power generated from the first 20 % of the blade is almost neglected ($\sim 4\%$), on the other hand the last 20 % of the blade (36 %) generates the highest power. Furthermore, an approximate 85 % of the power is located in the last 60 % of the radial position of the blade. According to Burton et al. (2001), at the tip of the blade the lift force is almost normal to the rotor plane. The tangential component of the lift force is small and its contribution to the torque is insufficient. Consequently the power is reduced at the tip of the blades.

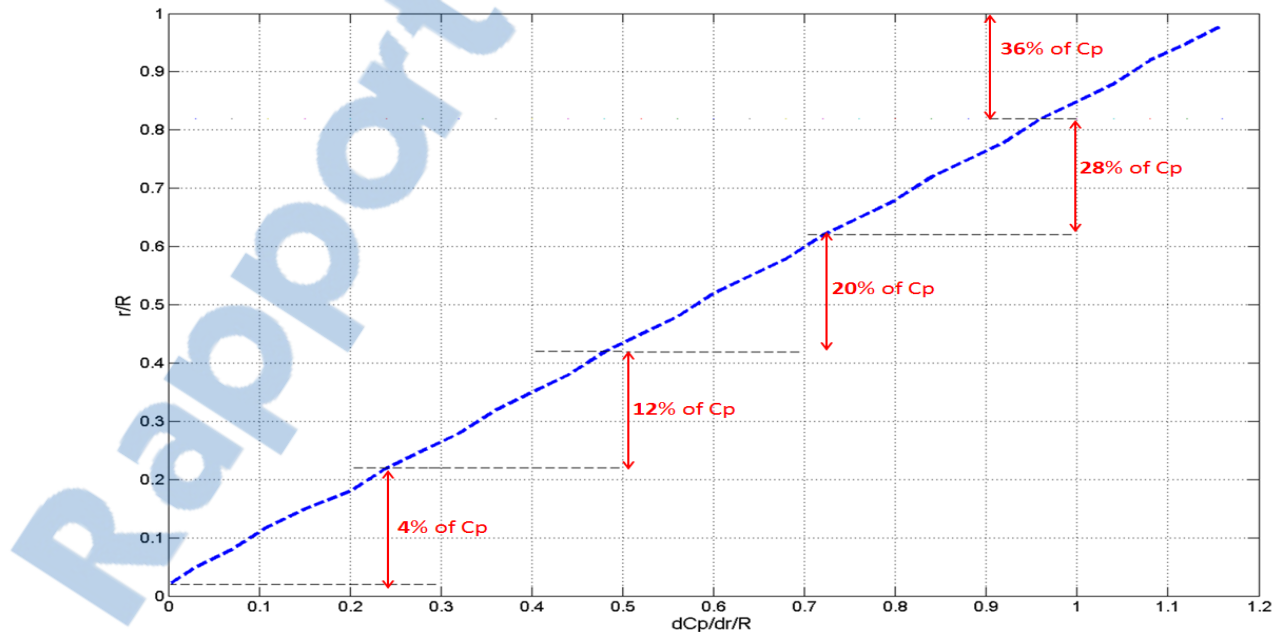


Figure 3.4. Elementary power coefficient along the span

3.5.2 Water collection efficiency

According to Eq. (3), collection efficiency is an important factor that contributes in controlling the amount of accreted ice. Therefore, within similar meteorological and geometric conditions, hydrometeors with different subfreezing water droplet diameters generate different collection efficiencies along the blade. Figure 3.5 shows three profiles of collection efficiency that correspond to supercooled stratus clouds (fog), supercooled drizzle and freezing rain with droplet diameters 20 μm , 200 μm and 2000 μm respectively. Due to the large size of rain drops, the water drops are all collected when at impact with the leading edge along the entire blade, as shown in Figure 3.5. Except for a slight decrease of collection efficiency near the root of the blade, the drizzle droplets maintain a high collection which is compared to that of rain droplets. Distinctively, supercooled fog droplets with a diameter of 20 μm are characterized with a collection efficiency that varies approximately from 0.09 near the root of the blade to more than 0.9 at the tip. Depending on the radial position, the rotational motion of wind turbine leads to a linear increase of relative velocity, starting from the root of the blade to the tip. The outer section of the blade has the smallest chord length and leading edge. Furthermore, Figure. 5 corroborates the fact (Eqs. (4)–(5)) that higher velocity, smaller water drops and cylinder diameter all increase the droplet collection efficiency.

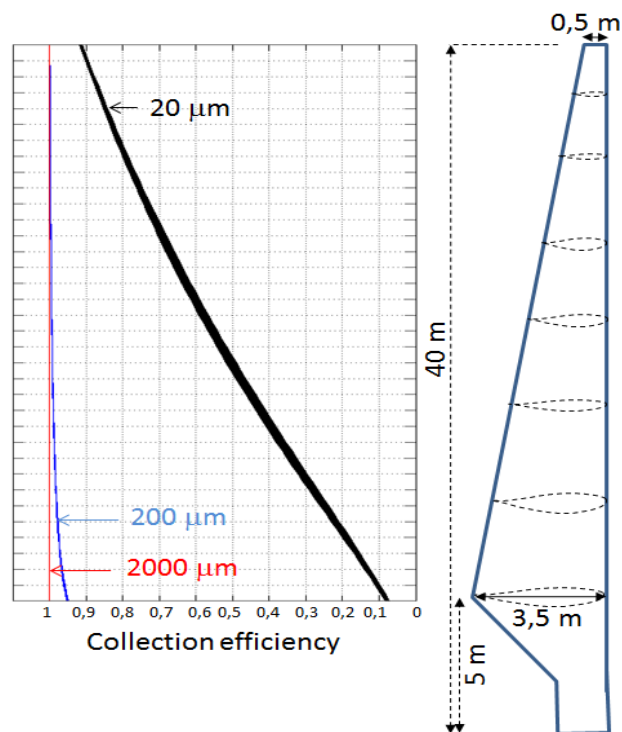


Figure 3.5. Collection efficiency along the blade for different droplet diameters (fog, drizzle, rain)

3.5.3 Ice mass rate

For the purpose of simplification, the evaporation and sublimation of liquid water masses are not considered for the calculation of the mass rate of ice accumulation. Rather, the mass rate M of icing accumulation along the blade is derived from Eq. (6) which is the calculated water mass multiplied by the freezing fraction. The water mass collected on a blade that corresponds to freezing fraction equal 1 is represented in Figure 3.6. It is noticeable from Figure 3.6 that ice accretion on the blade causes a very uneven mass accumulation along the blade which can lead to undesirable wind turbine vibration and fatigue. Figure 3.6 illustrates that the maximum mass rate of ice is located on the outer section of the blade, precisely at $r/R=0.7$. From this position until the tip, the maximum



mass rate shows a slight decrease. Toward the opposite direction the maximum mass rate decreases significantly to reach its minimum near the blade root zone. Higher liquid water content corresponds to higher accumulation mass rates and a more accentuated peak. The highest ice accumulation rate shown in Figure 6 corresponds to the highest value of liquid water content $0.36 \text{ g} \cdot \text{m}^{-3}$ followed by $0.2 \text{ g} \cdot \text{m}^{-3}$, $0.07 \text{ g} \cdot \text{m}^{-3}$ and $0.04 \text{ g} \cdot \text{m}^{-3}$ respectively.

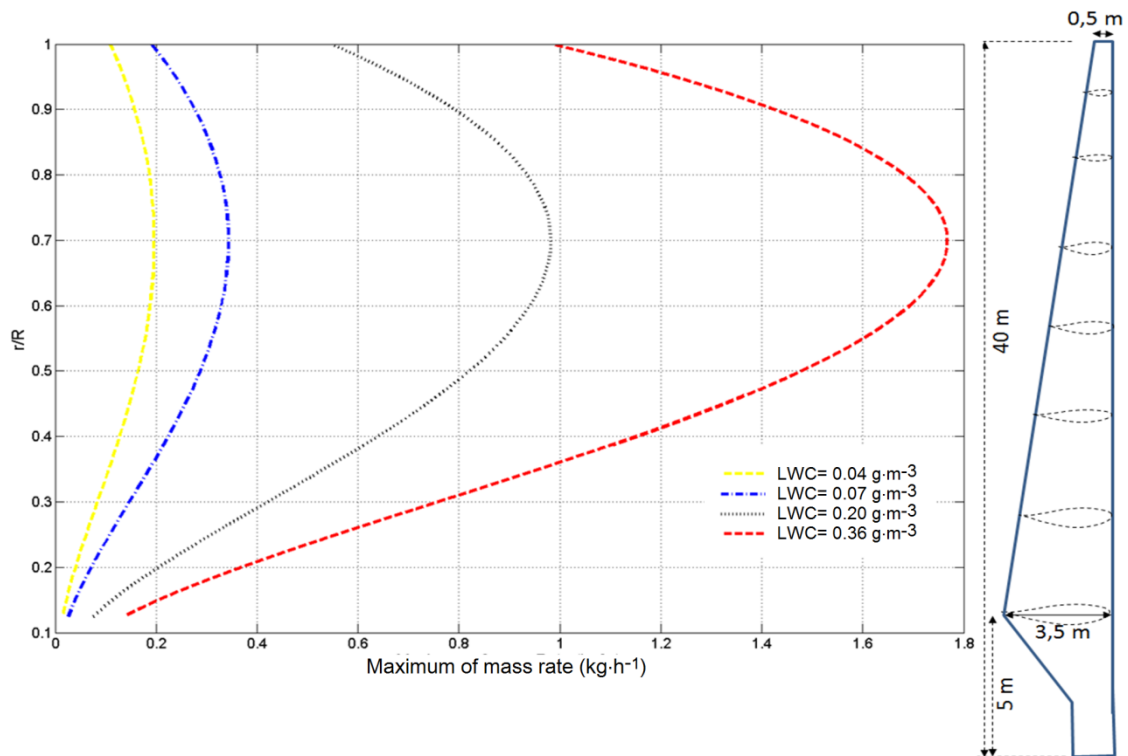


Figure 3.6. Ice mass rate along the span for different liquid water contents.

3.5.4 Aerodynamic effect

In order to investigate the aerodynamic effect of ice accumulation along the blade, a dimensionless thickness rate is introduced. This parameter h/c is represented by the ratio of thickness rate to chord length. The dimensionless thickness rate distribution on the blade

for four liquid water contents $0.04 \text{ g}\cdot\text{m}^{-3}$, $0.07 \text{ g}\cdot\text{m}^{-3}$, $0.2 \text{ g}\cdot\text{m}^{-3}$, $0.36 \text{ g}\cdot\text{m}^{-3}$ is illustrated in Figure 3.7. For different liquid water contents the thickness rate follows a similar tendency as the collection efficiency that increases towards the tip of the blade. However the gradient of thickness rate along the blade is less important for smaller values of liquid water content. The area on the blade that is most affected aerodynamically due to ice accumulation is located approximately on the last 20 % of the outer section of the blade.

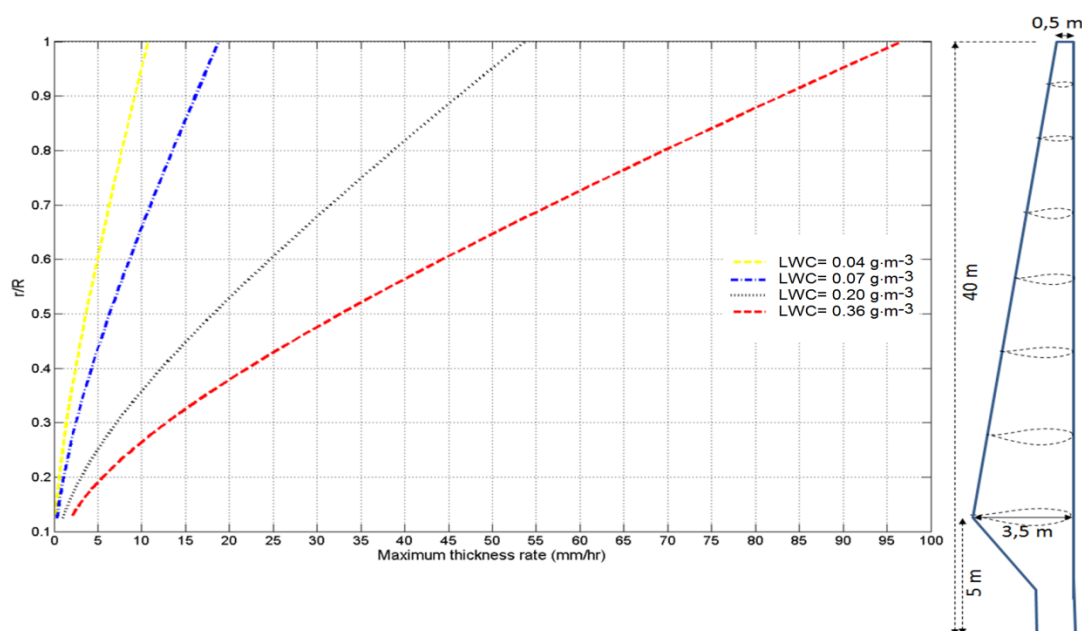


Figure 3.7. Maximum ice thickness rate along the span for different liquid water content

The behavior of the dimensionless thickness h/c is illustrated in Figure 3.8, for a liquid content of $0.2 \text{ g}\cdot\text{m}^{-3}$ at a wide range of subfreezing temperatures $[0 \text{ }^\circ\text{C} - 14 \text{ }^\circ\text{C}]$. When the temperature becomes colder than $-14 \text{ }^\circ\text{C}$, the dimensionless thickness reaches its maximum limit and remains unchangeable. The increase of elementary power production from the root to the tip of the blade illustrated in Figure 3.4 is corroborated by the same

tendency of the aerodynamic effect shown in Figure 3.8. In addition, within the same position on the blade, the variation of subfreezing temperatures has an accentuated aerodynamic impact towards the tip of the blade. Consequently, ice thickness appears most pronounced along the blade where the most power is generated. An apparent inconsistency regarding the effect of temperature along the blade is also featured in Figure 3.8. The aerodynamic effect is insignificant at all temperatures near the root of the blade. On the other hand, away from the root of the blade, colder temperatures manifest a larger aerodynamic response.

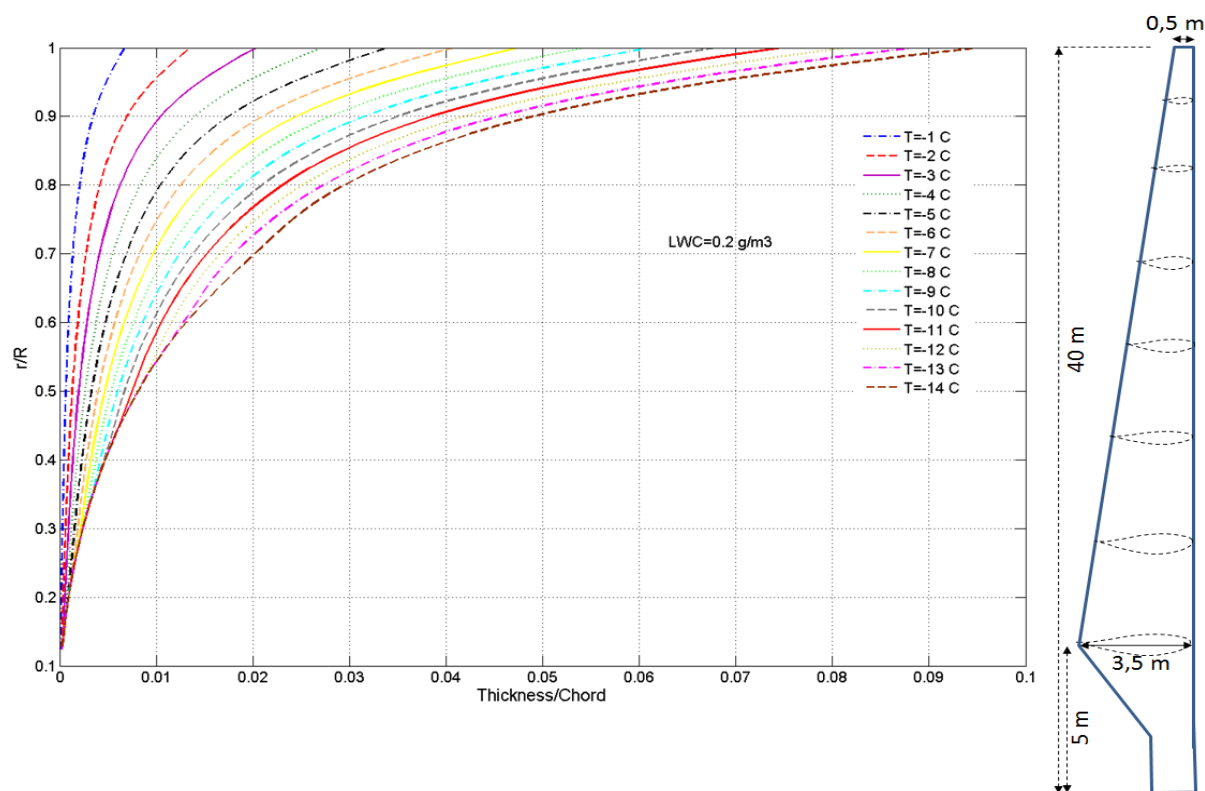


Figure 3.8. Aerodynamic effect along the blade for $LWC = 0.2 \text{ g} \cdot \text{m}^{-3}$.

3.5.5 Freezing fraction

In order to determine the boundary values that distinguish the wet icing processes (Glaze) from the dry icing processes (Rime), the Ludlam limit along the span for different temperatures and four liquid water contents is plotted in Figure 3.9. This limit represents the temperatures at which the liquid water becomes fully frozen and the freezing fraction is equal to 1. Therefore, larger amounts of collected supercooled liquid water located at the radial positions from $r/R = 0.8$ to the tip of the blade require the coldest temperature to reach a complete solidification. Furthermore, the radial positions from $r/R=0.8$ to the tip are characterized by a nearly similar freezing fraction. Under icing conditions with liquid water contents $0.36 \text{ m}\cdot\text{s}^{-1}$, $0.2 \text{ m}\cdot\text{s}^{-1}$, $0.07 \text{ m}\cdot\text{s}^{-1}$, and $0.04 \text{ m}\cdot\text{s}^{-1}$ and at air temperatures $-23 \text{ }^\circ\text{C}$, $-13.5 \text{ }^\circ\text{C}$, $-5 \text{ }^\circ\text{C}$, and $-3 \text{ }^\circ\text{C}$ respectively, all the collected water along the blade completely freezes and forms rime ice. On the other hand, at higher temperature both rime ice and glaze are formed on the blade, with rime ice near the root of the blade, followed by glaze on the outer section of the blade.

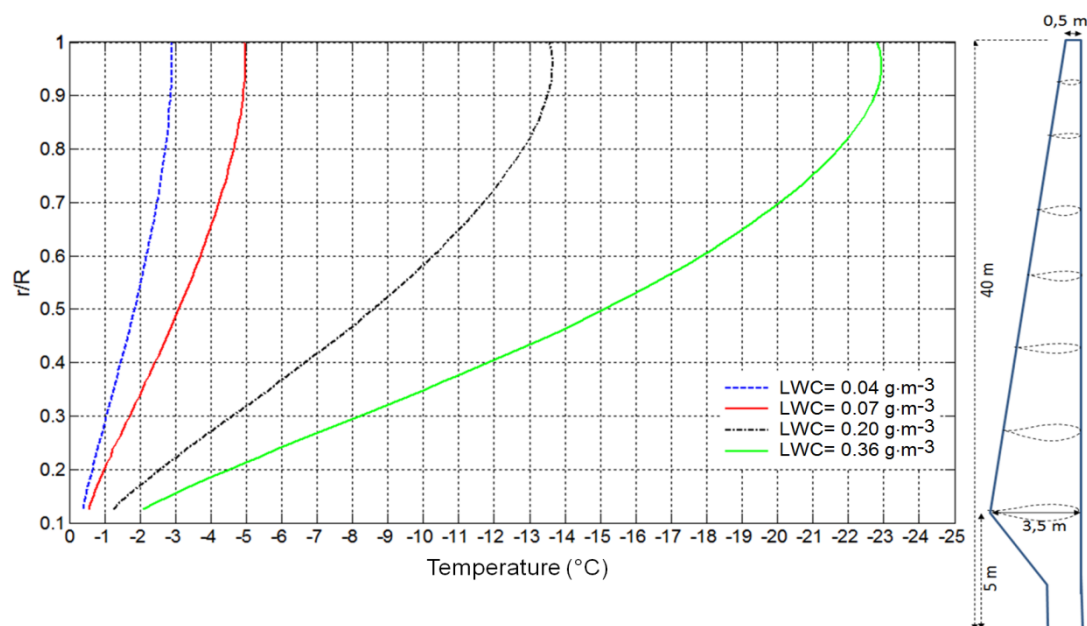


Figure 3.9. Ludlam limit for different liquid water content.

The radial position of the transition point between Rime and Glaze depends on air temperature. Freezing fractions at different temperatures are represented on Figure 3.10. The freezing fraction which is equal to 1 reflects a complete freezing of liquid water and therefore associated with rime ice. Within the subfreezing range, specifically at warmer temperatures, the collected supercooled liquid water turns into rime ice, initially near the root of the blade, while the other distant radial positions keep the supercooled liquid water partially frozen (glaze). As shown in Figure 3.10, further cooling leads to an increase of rime ice which will gradually cover the entire blade. In addition, the critical effect of air temperature on freezing fraction and consequently the type of ice are demonstrated in Figure 3.10. For a liquid water content of $0.2 \text{ g}\cdot\text{m}^{-3}$ and at air temperatures between $0 \text{ }^{\circ}\text{C}$ and $-2 \text{ }^{\circ}\text{C}$ the collected liquid water is partially frozen and forms only glaze all over the blade. With a temperature of supercooled liquid water at $-2 \text{ }^{\circ}\text{C}$ and cooler, rime ice begins

to appear first in the inner section near to the root of the blade and moves progressively with decreasing temperature towards the tip. Once the temperature reaches $-13.5\text{ }^{\circ}\text{C}$, all the collected water becomes frozen and forms rime ice all along the blade. Partial freezing of the collected supercooled liquid water generates a runback of the unfrozen liquid water which eventually will freeze and form uneven shapes of ice. The freezing fraction 0.88 represents a critical value that brings about the most aerodynamic hazardous double horn ice shape (Fortin and Perron, 2009). For a liquid water content of $0.2\text{ g}\cdot\text{m}^{-3}$ the temperature $-12\text{ }^{\circ}\text{C}$ represents the coldest temperature that maintains a freezing fraction of 0.88 located on the outer section of the blade $r/R \sim [0.93\ 0.96]$.

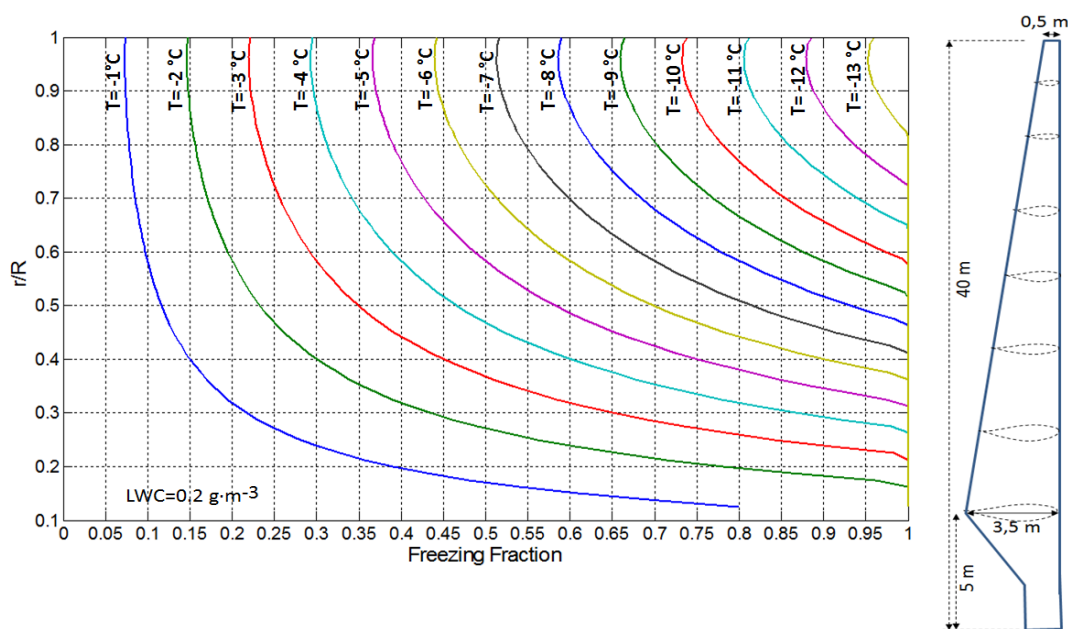


Figure 3.10. Freezing fraction along the span for different temperatures ($\text{LWC} = 0.2\text{ g}\cdot\text{m}^{-3}$).

3.5.6 Power loss

In the zone of interest on the blade which is located between the radial position $r/R=0.8$ and 1, the power production represents 38% of the total production of a wind turbine. The supercooled liquid water collected in this segment of the blade requires the coldest air temperature in order to form rime ice. Within this section, the accumulated glaze on the blade reshapes the airfoil resulting in higher aerodynamic degradation. Decreasing temperature as shown in Figs. 9 and 10 indicates that the radial position $r/R \sim [0.93 \ 0.96]$ is the last position where collected water becomes rime ice on the blade. In order to quantify production degradation, the power loss factor f is introduced. The values of the power loss factor f reflect the normalized variations of power requirements for rotor blade helicopters under icing conditions.

$$C_p' = \frac{C_p}{f} \quad (13)$$

C_p' represents power coefficient under icing effect and f is derived from the effect of ice on helicopter power requirements introduced by Fortin and Perron (2009). Contrary to helicopters that require power to rotate, wind turbines rotate to produce power. For rotating iced blade of helicopter it requires an increase of the provided power to maintain the rotation frequency. On the other hand, ice accumulation on wind turbines reduces the expected power production. Therefore the power coefficient for clean wind turbine blades is divided by the power loss factor f in order to obtain the power coefficient under icing conditions. The power loss factor f , as shown in Figure 3.11a and 3.11b, reflects the aerodynamic degradation and power loss which depends on the freezing fraction that

determines the ice shape. This factor intervenes only at subfreezing temperatures starting with a value 1 at 0 °C which corresponds to a clean blade. Beyond a value of 1, the power loss factor f follows a linear increase until it reaches its maximum value at 4.4. This peak value is associated with the freezing fraction 0.88 that corresponds to the double horn ice shape which is the most aerodynamically hazardous situation. Further cooling is associated with an increase in freezing fraction and a slight decrease of the power loss factor f until it reaches the minimum value of 3.3. At this minimum, the freezing fraction is equal to 1 and all the supercooled liquid water becomes fully frozen and forms rime ice. The power loss factor that indicates the maximum energy degradation at the radial position $r/R \sim [0.93:0.96]$ is accordingly applicable for all liquid water contents. Figure 3.11b illustrates power loss factor for liquid water contents of $0.04 \text{ g}\cdot\text{m}^{-3}$, $0.07 \text{ g}\cdot\text{m}^{-3}$, $0.2 \text{ g}\cdot\text{m}^{-3}$, and $0.36 \text{ g}\cdot\text{m}^{-3}$ that corresponds to the maximum aerodynamic degradation at temperatures $-2.6 \text{ }^\circ\text{C}$, $-4.5 \text{ }^\circ\text{C}$, $-12 \text{ }^\circ\text{C}$, and $-20 \text{ }^\circ\text{C}$ respectively, and forming rime ice at temperatures $-3 \text{ }^\circ\text{C}$, $-5 \text{ }^\circ\text{C}$, $-13.5 \text{ }^\circ\text{C}$, and $-23 \text{ }^\circ\text{C}$ respectively. According to the variation of power loss factor in Figure 3.11b, the higher liquid water contents are featured with larger ranges of temperatures where the power loss caused by glaze is significant. The radial position $r/R \sim [0.93:0.96]$ that belongs to the outer section of the blade brings about the largest power production.

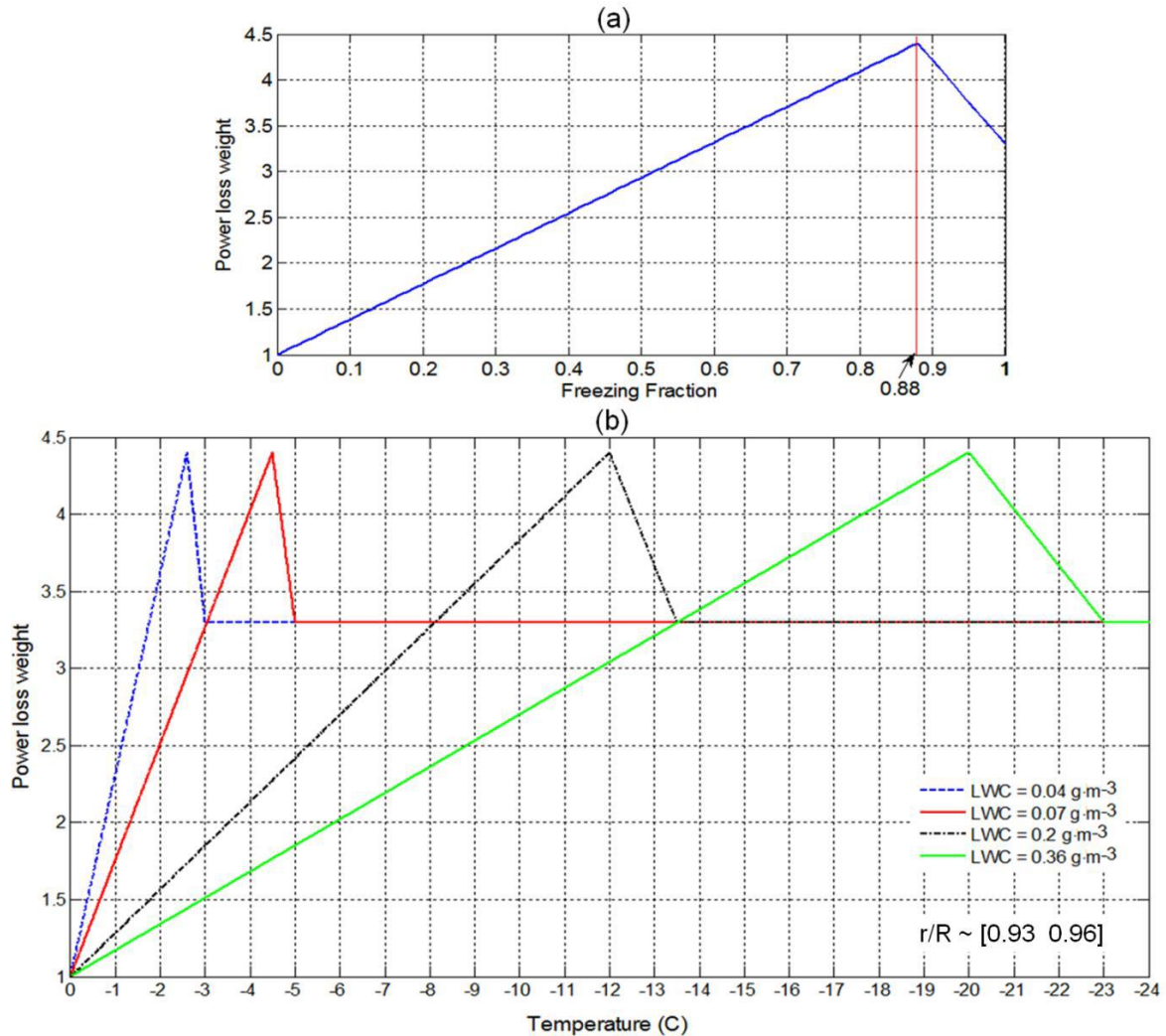


Figure 3.11. Aerodynamic reduction factor (a) Power loss vs freezing fraction (b) Power loss vs temperature for different liquid water contents.

Simultaneously, the freezing fraction 0.88 is associated with the double horn ice shape that imposes the highest aerodynamic degradation. For these reasons, Figure 3.12 shows how a particular focus on power production is achieved within these conditions. The degradation of elementary power coefficient C_p versus the temperature at the radial position $r/R \sim [0.93:0.96]$, for four values of liquid water contents; 0.04, 0.07, 0.2, and 0.36 g·m⁻³ is

shown in Figure 3.12. Power coefficient decreases with decreasing temperature until it reaches its lower limit that corresponds to the critical freezing fraction of 0.88, then it increases slightly to reach a constant value to form rime ice when the freezing fraction is equal to 1. With liquid water content $0.2 \text{ g}\cdot\text{m}^{-3}$, one notices that power production decreases until its minimum that corresponds to temperature $-12 \text{ }^\circ\text{C}$ and a freezing fraction 0.88. Colder than $-12 \text{ }^\circ\text{C}$, freezing fraction increases and it generates a slight increase in power until reaching a freezing fraction 1 when at which point the dry growth regime starts. The depletion of power coefficient in Figure 3.12 is reached only if enough ice is accumulated on the blade. Also, the behavior of power coefficient in Figure 3.12 pictures shows the response of wind turbine production loss to geometrical and meteorological icing conditions. For this calculation it is assumed that the icing event duration is long enough to generate the critical ice shape. The upper half of the blade is more affected by icing due to the partial freezing. With regard to liquid water content of $0.2 \text{ g}\cdot\text{m}^{-3}$ and a temperature of $-12 \text{ }^\circ\text{C}$, the power degradation appears under all icing types (rime and glaze). As shown in previous Figure 3.10, starting from a radial position near $r/R = 0.72$ that corresponds to the beginning of glaze, the magnitude of power degradation increases gradually and becomes more accentuated. At its lower level it is located approximately at $r/R \sim [0.93 \text{ } 0.96]$. The amount of accumulated ice depends on the duration of ice accretion.

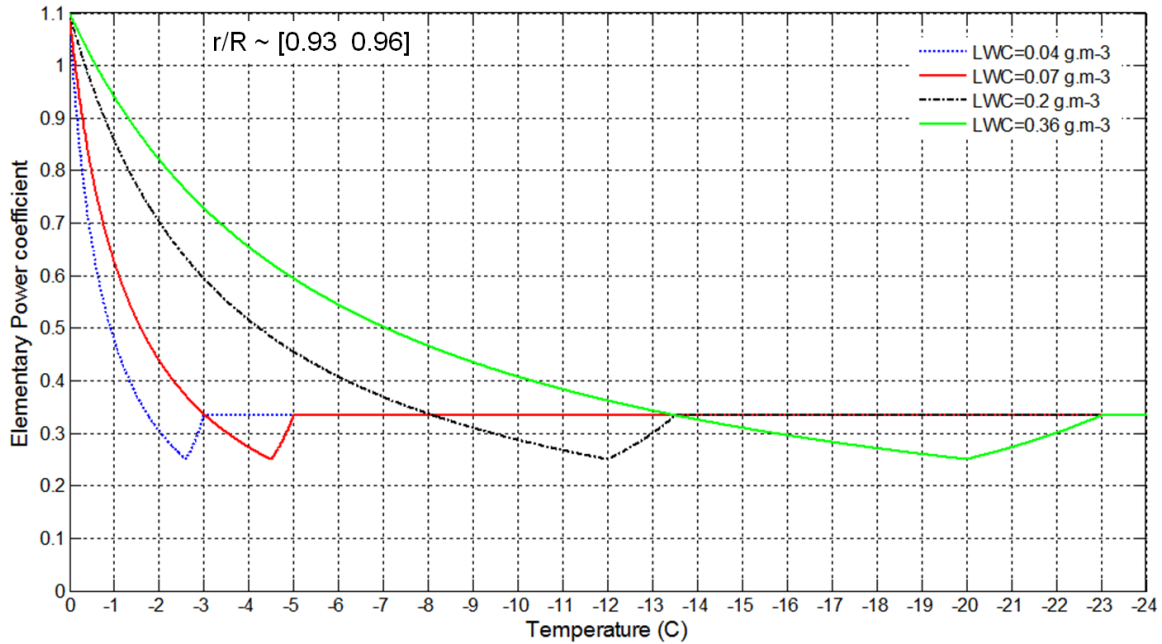


Figure 3.12. Power loss at $r/R \sim [0.93 \ 0.96]$ for different liquid water contents.

According to Fortin and Perron (2009), the highest power loss for the subscaled iced helicopter's blades was reached after 160 s of ice accretion, the relative speed of the blade at the radial position $r/R \sim [0.93 \ 0.96]$ was about $130 \text{ m}\cdot\text{s}^{-1}$ and a liquidwater content of $0.84 \text{ g}\cdot\text{m}^{-3}$. Accumulation parameter A presented in Eq. (14) (Anderson and Tsao, 2005) is utilized, in order to estimate the duration required for ice accretion on wind turbine blades to reach a similar ice shape (hazardous double horn).

$$A = \frac{E \cdot LWC \cdot U \cdot t}{C} \quad (14)$$

A : Accumulation parameter, E : total collection efficiency, U : relative speed, t : icing event duration, C : chord. The indexes wt , h refer to wind turbine and helicopter respectively. For the same freezing fractions, collection efficiencies and accumulation parameters (A_{wt} , A_h),

the duration required for ice accretion on the blade of a turbine is represented in Eq. (15) and Figure 3.13 that correspond to different liquid water contents:

$$t_{wt} = \frac{LWC_h \cdot U_h \cdot C_{wt} \cdot t_h}{LWC_{wt} \cdot U_{wt} \cdot C_h} \quad (15)$$

Higher liquid water contents correspond to shorter required icing duration to reach higher power loss. In reference to the subscaled helicopter's rotor blade (Fortin and Perron, 2009), Figure 3.13 illustrates the required duration for ice accretion on wind turbines to match the same or the highest power loss under icing conditions on the helicopter's blades (freezing fraction 0.88, $r/R = [0.93 \text{ } 0.96]$) for different liquid water contents. As illustrated in Figure 3.13, for liquid water contents $0.04 \text{ g}\cdot\text{m}^{-3}$, $0.07 \text{ g}\cdot\text{m}^{-3}$, $0.2 \text{ g}\cdot\text{m}^{-3}$, and $0.36 \text{ g}\cdot\text{m}^{-3}$ the durations needed to reach the hazardous double horn ice shapes are 13.2 h, 7.5 h, 2.6 h and 1.5 h respectively. In addition, icing events with liquid water contents smaller than $0.04 \text{ g}\cdot\text{m}^{-3}$ are excluded from forming double horn ice shapes with a freezing fraction of 0.88. In order to evaluate the required duration of icing events, the results from Figure 3.13 are compared to realistic icing events.

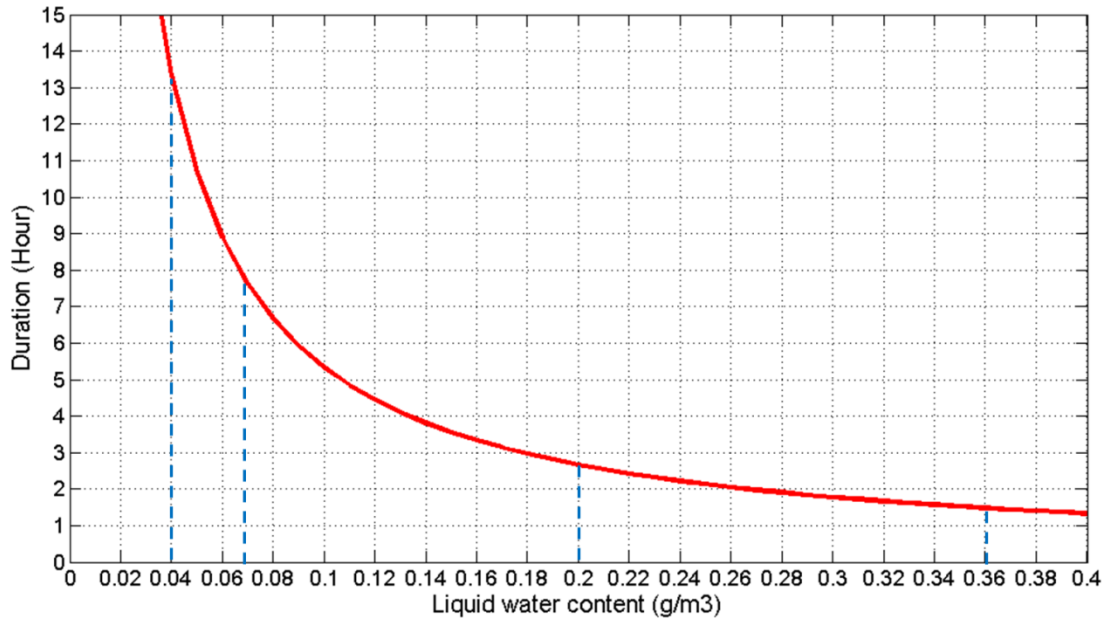


Figure 3.13. Required duration for ice accretion on wind turbines to match the same highest power loss under icing conditions on helicopter's blades (freezing fraction 0.88, $r/R = [0.93 \text{ } 0.96]$) for different liquid water contents.

The use of North American Regional Reanalysis (NARR) allowed a climate investigation of in-cloud icing near surface level, during a 32 year period from 1979 until 2010. As shown in Figure 3.14, from these reanalysis over the site of Mount-Bélair (Canada), the duration of icing events and the corresponding supercooled liquid water contents are estimated according to a previous study done by Lamraoui et al. (2013). The calculation of the 32-year average that corresponds to the occurrence of icing events enables finding the typical durations for each range of supercooled liquid water contents of $0.04 \pm 0.02 \text{ g}\cdot\text{m}^{-3}$, $0.07 \pm 0.02 \text{ g}\cdot\text{m}^{-3}$, $0.2 \pm 0.02 \text{ g}\cdot\text{m}^{-3}$, and $0.36 \pm 0.02 \text{ g}\cdot\text{m}^{-3}$. The longer durations of icing event are associated with a smaller supercooled liquid water contents.

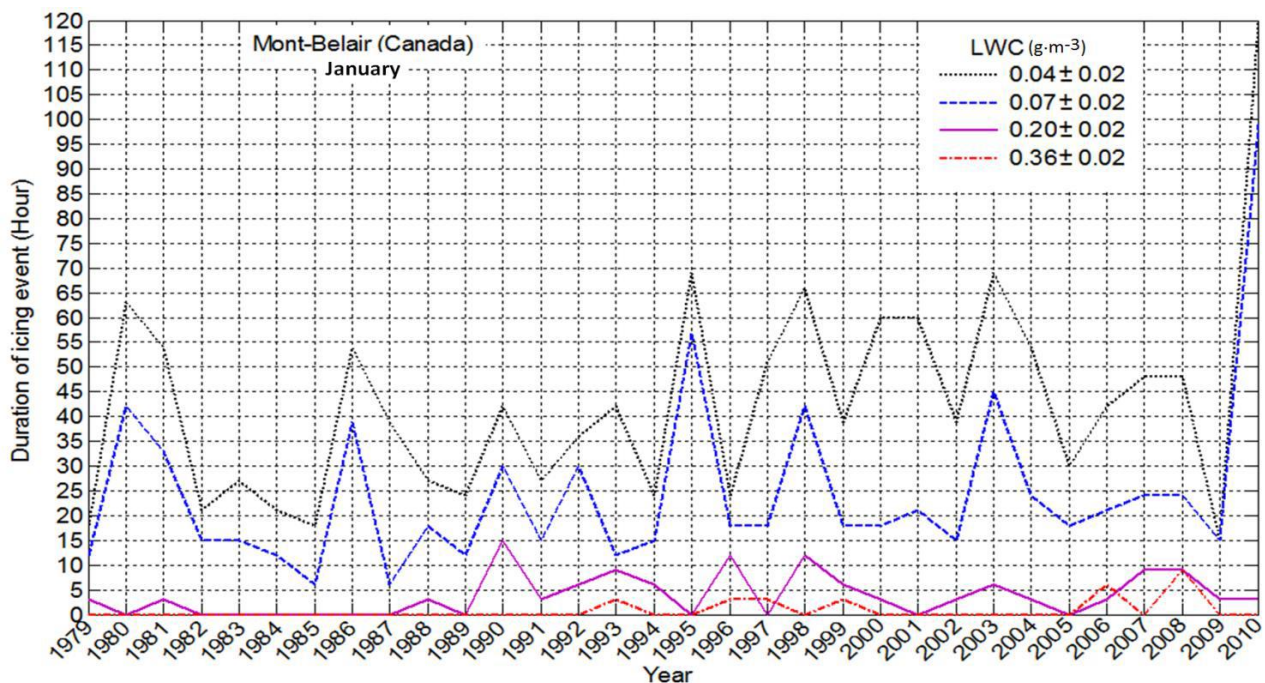


Figure 3.14. Monthly duration of icing events from reanalysis over Mount-Bélair site during January (from 1979 to 2010).

The 32-year averages of the duration of icing events are introduced in Table 3.1. The results demonstrated in Table 3.1 characterize the climatology of atmospheric icing of the Mount-Bélair site located near Quebec City (Canada).

Table 3.1 : Duration of icing events from reanalysis: 32-year icing climate

Supercooled liquid water content ($\text{g}\cdot\text{m}^{-3}$)	Average duration of icing event Period: 1979-2010 over Mount-Bélair
0.04 ± 0.02	~43 h
0.07 ± 0.02	~24 h
0.20 ± 0.02	~6 h
0.36 ± 0.02	~4 h

The values of liquid water contents in Figure 3.14 and Table 3.1 delineate five severity classes (Lamraoui et al., 2013). The comparison of icing event durations from Figure 3.13 and Table 3.1 shows that all icing severity ranges endure enough to fulfill the

requirement of forming the double horn hazardous ice shape. The freezing fraction of 0.88 corresponds to the largest aerodynamic degradation. Therefore, the starting temperature that coincides with the occurrence of ice accretion along the blade with freezing fraction only 0.88 and beyond corresponds to the maximum power loss. For a liquid water content $0.2 \text{ g} \cdot \text{m}^{-3}$, the maximum power loss happens at temperature $-12 \text{ }^\circ\text{C}$. Under these meteorological conditions, the radial position $r/R \sim [0.93 \text{ } 0.96]$ holds an ice with a freezing fraction of 0.88. Elsewhere on the blade the freezing fraction exceeds 0.88 and varies accordingly to reach 1.

The electrical power loss due to icing conditions is represented in Figure 3.15. The maximum electric power degradation that wind turbines can reach under icing effects is obtained by involving the modified power coefficient C_p' from Eq. (13). More specifically, Figure 3.15(b) represents the quantification of power loss for different wind speed when the liquid water content is $0.2 \text{ g} \cdot \text{m}^{-3}$ and air temperature equivalent to $-12 \text{ }^\circ\text{C}$. Under these geometrical and meteorological conditions, the maximum power production loss occurs when wind speed is approximately around $10.5 \text{ m} \cdot \text{s}^{-1}$. At the temperature of $-13.5 \text{ }^\circ\text{C}$, only rime ice is accreted all along the blade, showing power degradation. The temperature of $-12 \text{ }^\circ\text{C}$ engenders only rime ice on the radial positions from the root until $r/R \sim 0.72$. Beyond this position to the tip of the blade, only glaze is accreted with a different freezing fraction. From the result represented in Figure 3.15, one concludes that a slight change in temperature can provoke a change in power loss. Within a range of wind speed $\sim [7 \text{ m} \cdot \text{s}^{-1} \text{ } 17 \text{ m} \cdot \text{s}^{-1}]$, a small decrease in temperature ($\Delta T \sim 1.5 \text{ }^\circ\text{C}$) generates a significant reduction of power production that can reach its maximum of 0.8% with a wind speed of $10.5 \text{ m} \cdot \text{s}^{-1}$.

Under icing conditions, both temperatures $-12\text{ }^{\circ}\text{C}$ and $-13.5\text{ }^{\circ}\text{C}$ correspond to significant maximum power production degradation of approximately 40%.

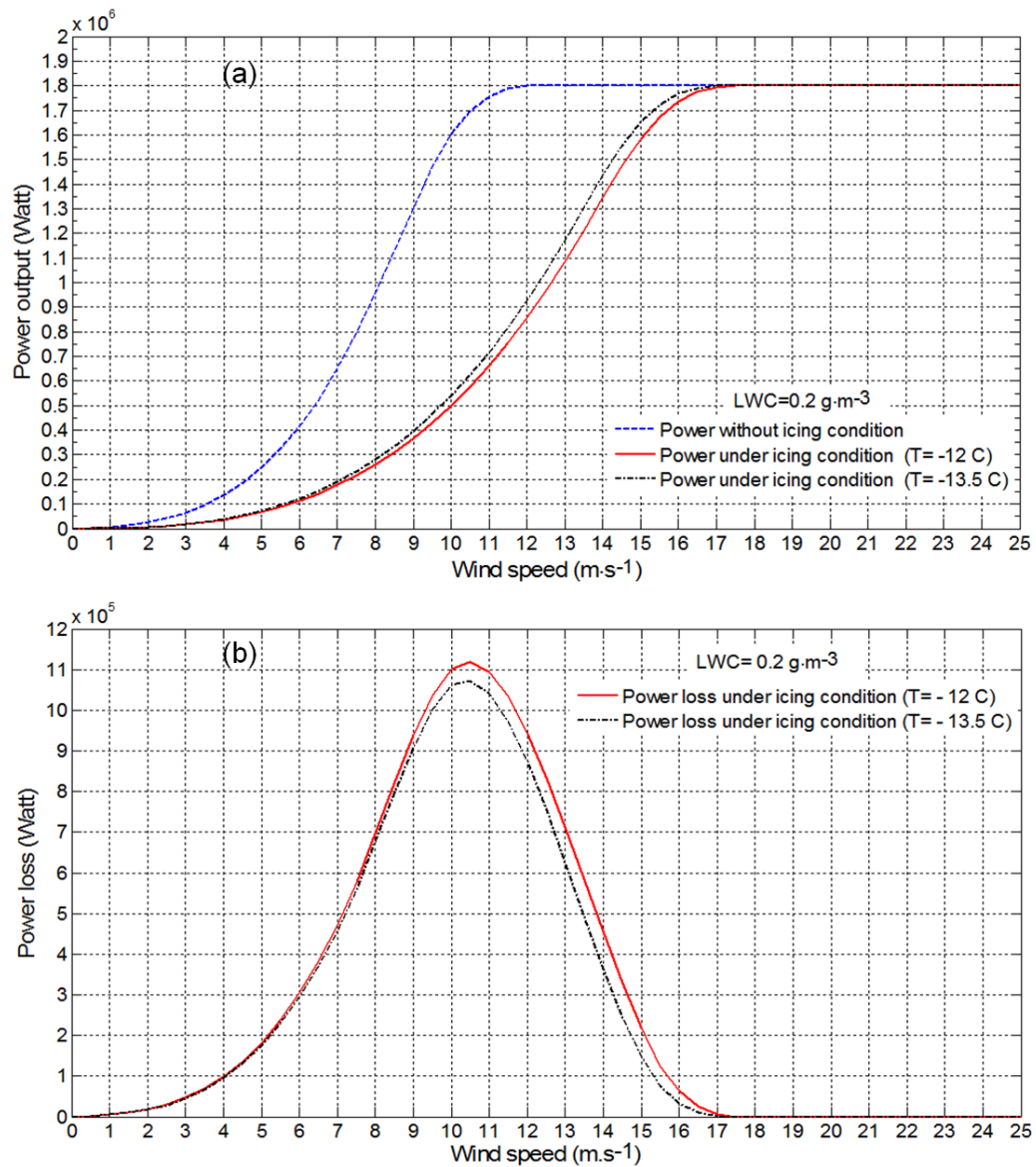


Figure 3.15. Power under icing effects for $\text{LWC} = 0.2\text{ g} \cdot \text{m}^{-3}$ at $T = -12\text{ }^{\circ}\text{C}$ and $T = -13.5\text{ }^{\circ}\text{C}$, (a) Power curve with and without icing (b) Electrical power loss.

3.6 Analysis

Since the rotational motion of the blade generates a varying relative velocity that increase from zero at the root of the blade to its maximum at the tip, consequently the elementary power is distributed unevenly along the blade. The power production extracted from the first quarter of the blade near the root is practically neglected. Except for the tip, the blade aerodynamic is greatly influenced by the outer section. The obtained result as shown in Figure 3.4, demonstrates that 85% of the produced power is originated from the outer 60% segment of the blade. From the simplified cylinder model used in this study, the collection efficiency involved in quantifying ice accretion varies mainly according cylinder diameter, and droplet diameter of supercooled hydrometeors. Considering all ranges of supercooled hydrometeors, with larger droplet diameters ($\geq 200 \mu\text{m}$) that are associated with freezing drizzle or rain, the collection efficiency is approximately consistent and not affected by the geometry variation along the blade. On the other hand, as illustrated in Figure 3.5 supercooled fog or supercooled cloud has a substantial variation of collection efficiency between both edges of the blade. The outer section of the blade that coincides with a higher aerodynamic is characterized with the highest collection efficiency that is comparable to freezing rain or drizzle.

The rate of ice thickness and the rate of the ratio of thickness to chord as show in Figures 3.7 and 3.8 respectively corroborate the fact that the outer section of the blade considerably influence the aerodynamics of the blade and is the least ice-phobic segment on the blade.

The freezing fraction is a very important parameter that substantially influences the type and the shape of accreted ice on the blade. As illustrated in Figure 3.9, the fact that higher liquid water contents associated with higher latent heat requires colder temperature to reach the complete solidification of collected supercooled liquid water. When temperature decreases as indicated in Figures 3.9 and 3.10, rime ice starts to appear first near the root then gradually continues to spread towards the tip of the blade.

Blade's airfoils are sensitively designed to allow a smooth flow of air over the top and bottom surfaces and when ice accumulation occurs it then alters the shape of airfoil. The geometry of a blade's airfoil is crucial to the aerodynamics of wind turbines and consequently for power production. Rime ice follows the shape of the airfoil; however the glaze shape can be very irregular depending upon the freezing fraction. When ice first accumulates it has no serious effect, but gradually it builds forward and along the top and bottom surfaces of airfoil and causes more hazard. When the blade of a wind turbine strikes supercooled water droplets, the leading edge becomes covered with a film of supercooled water that freezes from inside out. Clear ice (glaze) which forms rapidly can represent the most hazardous form of all icing conditions, whereas rime ice forms slowly. At the beginning, the ice build-up follows the blade's airfoil. Once it reaches the points of maximum camber, the shape of airfoil changes drastically. Consequently the air flow becomes disrupted which generates drag increase, and reduced lift. From an experimental study (Fortin and Perron, 2009) the freezing fraction of 0.88 is proven to generate the most aerodynamically hazardous ice shape (double horn). This freezing fraction and a normalized power variation from a helicopter's rotor blade were used to introduce a new

power loss factor to assess power degradation subjected to ice accretion. This power loss factor is introduced in Figures 3.11a and 3.11b. For each elementary radial position along the blade, the freezing fraction zero corresponds to no-ice condition. The collected supercooled liquid water starts to freeze with increasing freezing fraction and decreasing the temperature until reaching the peak of power loss that corresponds to the freezing fraction of 0.88. As shown in Figure 3.11b, the temperature required to reach the maximum loss varies according to the value of liquid water content. Once the maximum power loss is achieved, an additional cooling will generate lesser power loss. Radial position of $r/R \sim [0.93 \text{ } 0.96]$ corresponds to the most critical freezing fraction on the blade.

Under the same meteorological conditions, the critical zone on the blade is limited to a small section where potentially the double horn ice shape would form with a freezing fraction of 0.88. Therefore, Figure 3.12 demonstrates power degradation of the critical temperatures for 4 values of liquid water contents $0.04 \text{ g}\cdot\text{m}^{-3}$, $0.07 \text{ g}\cdot\text{m}^{-3}$, $0.2 \text{ g}\cdot\text{m}^{-3}$, and $0.36 \text{ g}\cdot\text{m}^{-3}$. By matching the accumulation parameters from a subscaled helicopter rotor blade with wind turbine blade helps determine the required duration of icing events that leads to the formation of the double horn ice shape. The variation of this recommended duration is presented in Figure 3.13. Within the range of liquid water content used for this study, the duration of icing events needed to form a double horn ice shape varies between 1.5 h and 13 h. As an attempt to verify whether these critical durations correspond to realistic icing events, the current study refers to a reliable set of historical meteorological database details from the North American Regional Reanalysis (NARR).

The analysis of data from North American Regional Reanalysis at a climate scale that spanned 32 years during January demonstrated that less intense icing events had smaller liquid water content and were associated with prolonged occurrences of icing events. During very intense icing events with a short period of occurrences, the optimum alternative for wind turbines is to stop turning, in order to minimize ice accumulation. The results obtained from reanalysis in Table 3.1 demonstrate that intense icing events last up to 6 h. On the other hand, light icing events that can exceed 2 days, this can present prolonged power degradation and serious hazardous conditions for the wind turbine industry. In addition, Figure 3.5 illustrates that smaller droplets target the most aerodynamically critical zone on the blade which is located in the outer section. Therefore, shorter occurrences of icing events that correspond to higher intensity with larger droplet diameters are less harmful.

The critical freezing fraction 0.88 that corresponds to the double horn ice shape occurs locally within a limited segment on the blade. Once freezing fractions along the blade reaches 0.88 or higher, the wind turbine indicates the maximum of power degradation. This scenario corresponds to glaze accumulation located on $r/R \sim [0.93 \ 0.96]$ and rime ice elsewhere on the blade. The power output shown in Fig. 15 which originated from clean and iced blades reveal that regardless of the type of ice, the power production degradation is still significant and can reach ~40 % of the expected power production. The critical glaze contributes slightly to power loss with an approximate amount of ~0.8 %, because of the limited area where the double horn ice shape forms in relation to the entire blade.

3.7 Conclusion

The present study determines power production loss, due to the accumulation of ice along the blades of wind turbines. The investigation is based on cylinder model and power loss model. The power degradation model is based on the results of a previous study that was done on a sub-scaled helicopter rotor blade. The approach depends on the assumption that a wind turbine remains continually operational, regardless the severity of icing events. Along the blade, the results show that both mass and thickness of accreted ice on the leading edge increase gradually with decreasing the chord size. The results show that 85% of power production is generated from the section on the blade that is located in the last 60% of the blade towards the tip. As well, the results enable the identification of the localized radial position that starts from $r/R=0.8$ to the tip of the blade and corresponds to the highest aerodynamic degradation and consequently power production loss. According to the size of the leading edge, the air temperature, the liquid water content and the freezing fraction vary along the blade resulting in different ice types and shapes. Regardless of the type of ice, power production loss under icing conditions can reach a maximum of 40 % at a specific wind speed. Locally and within the same radial position, it is the shape rather than the thickness of ice that causes more icing hazards. The double horn shaped ice propels the highest aerodynamic degradation. This ice geometry corresponds to the freezing fraction of 0.88. In addition, from power loss model, the peak of the local power loss is associated with freezing fraction of 0.88 which represents only a portion of wet growth regime. The coexistence of both wet and dry ice simultaneously on the blade, and the limited radial section that has a critical freezing fraction, minimize the effect of local

double horn shaped ice formation and of power production loss on the entire from the whole wind turbine. Therefore, there is only a slight difference of approximately 0.8% in total power production loss caused by the existence of a confined critical wet ice along the blade, when compared to only dry ice. Typical icing event durations at climate scale obtained from reanalysis confirm that all icing events with all intensities persist enough to reach the hazardous freezing fraction. Also, icing events with high intensities correspond to shorter durations of occurrence. On the other hand, less intense icing events had smaller liquid water content and were associated with prolonged occurrences of icing events; light intensities events are associated to long lasting icing events. Based on the obtained results of this study, it can be useful to set up a cost effective ice-protection system. Regarding this system, it is recommended to cover only 60% of the blade. This would optimize power production under icing conditions. Also, this system can be equipped with a sensor located at the radial position $r/R=0.4$ or higher toward the tip. This sensor can then trigger the ice-protection system upon detection of a critical freezing fraction at this radial position.

3.8 References

- Abbot, I., von Doenhoff, A., 1959. Theory of wing sections, *2nd edition*. Dover Publications, New York.
- Anderson, D.N., Tsao, J.C., January 6–9, 2003. Evaluation and validation of the messenger freezing fraction. AIAA–2003–1218 *41st Aerospace Sciences Meeting and Exhibit*. American Institute of Aeronautics and Astronautics, Reno, Nevada.
- Antikainen, P., Peuranen, S., 2000. Ice loads, case study. *BOREAS V, wind power production in cold climates. Proceedings of an International conference*, Levi, Finland. Finnish Meteorological Institute (CD-ROM).
- Bendix, J., Thies, B., Cermak, J., Nauß, T., 2005. Ground fog detection from space based on MODIS daytime data — a feasibility study. *Weather Forecast*. 20, 989–1005.
- Bose, N., Rong, J.Q., 1990. Power reduction from ice accretion on a horizontal axis wind turbine. *Proc. 12th British Wind Energy Association, Wind Energy Conference* Norwich, UK.
- Botta, G., Cavaliere, M., Holttinen, H., 1998. Ice accretion at Acqua Spruzza and its effects on wind turbine operation and loss of energy production. *BOREAS IVFMI, Hetta, Finland* 77–86.
- Brodkey, R.S., Hershey, H.C., 1988. Transport phenomena: a unified approach. McGrawInternational Edition, New York (847 pp).
- Burton, T., Sharpe, D., Jenkins, N., Bossanyi, E., 2001. Wind Energy Handbook. John Wiley & Sons LTD. ISBN: 0-471-48997-2.
- Cober, S.G., Isaac, G.A., Strapp, J.W., 1995. Aircraft icing measurements in east coast winter storms. *J. Appl. Meteorol.* 34, 88–100.
- Modelling the risk of icing. In: Dierer, S., Cattin, R., Muller, S., Nygaard, B., Steiner, P., Calpini, B. (Eds.), International workshop on Atmospheric Icing of Structures (IWAIS XIII), Andermatt, September 8–11, 2009 (*COST Action 727*).
- Fikke, S., Ronsten, G., Heimo, A., Kunz, S., Ostrozlik, M., Persson, P.E., Sabata, J., Wareing, B., Wichura, B., Chun, J., Laakso, T., Santti, K., Makkonen, L., 2006. 2006: COST-727: atmospheric icing on structures measurements and data collection on icing: state of the art. *MeteoSwiss*, Switzerland.
- Fortin, G., Perron, J., 2009. Spinning Rotor Blade Tests in Icing Wind Tunnel. Paper AIAA 2009–4260 *1st AIAA Atmospheric and Space Environments Conference*, San Antonio, TX.

- Fortin, G., Perron, J., Ilinca, A., October 2005. A study of icing events at Murdochville: conclusions for the wind power industry. *International Symposium "Wind Energy in Remote Regions", Magdalen's Island.*
- Hansen, M.O.L., 2008. Aerodynamics of wind turbines, *Earthscan*, London (UK) and Sterling (USA) 2nd edition. 181.
- Hochart, C., Fortin, G., Perron, J., Ilinca, A., 2008. Wind turbine performance under icing conditions. *Wind Energy* 11, 319–333.
- Isaac, G.A., 1991. Microphysical characteristics of Canadian Atlantic storms. *Atmos. Res.* 26, 339–360.
- Jacobs, E.N., 1932. Airfoil section characteristics as affected by protuberances. *NACA Report No. 446.*
- Jasinski, W.J., Noe, S.C., Selig, M.S., Bragg, M.B., 1998. Wind turbine performance under icing conditions. *J. Sol. Energy Eng.* 120, 60–65.
- Jones, R., Williams, D.H., 1936. The effect of surface roughness of the characteristics of the aerofoils NACA 0012 and RAF 34. *British ARC, R&M No. 1708.*
- Laakso, T., Peltola, E., 2005. Review on blade heating technology and future prospects. 2005 *BOREAS VII Conference, 7–8th March 2005, Saarislkä, Finland.*
- Laakso, T., Baring-Gould, I., Durstewitz, M., Horbaty, R., Lacroix, A., Peltola, E., Ronsten, G., Tallhaug, L., Wallenius, T., 2010. State-of-the-art of wind energy in cold climates. VTT Working Papers 152. *VTT Technical Research Centre of Finland (71 pp.).*
- Laforte, J.-L., Allaire, M.A., 1992. Évaluation du Givromètre d'Hydro-Québec à Différentes Intensités de Givrage Sec et Humide. *Rapport HQ-92-02.*
- Lamraoui, F., Fortin, G., Benoit, R., Perron, J., Masson, C., 2013. Atmospheric icing severity: quantification and mapping. *Atmos. Res.* 128, 57–75.
- Makkonen, L., Autti, M., 1991. The effects of icing on wind turbines. *EWEC, Amsterdam, Netherlands.* 575–580.
- Manwell, J.F., McGowan, J.G., Rogers, A.L., 2009. Wind energy explained: theory, design and application. *John Wiley & Sons* 424.
- Marjaniemi, M., Peltola, E., 1998. Blade Heating Element Design and Practical Experiences. *BOREAS IVFMI, Hetta, Finland* 197–209.

- Mazin, I.P., Korolev, A.V., Heymsfield, A., Isaac, G.A., Cober, S.G., 2001. Thermodynamics of icing cylinder for measurements of liquid water content in supercooled clouds. *J. Atmos. Ocean. Technol.* 18, 543–558.
- Messinger, B.L., 1953. Equilibrium temperature of an unheated icing surface as a function of air speed. *J. Aerosol Sci.* 29–42 (vol. Jan).
- Parent, O., Ilinca, A., 2011. Anti-icing and de-icing techniques for wind turbines. *Crit. Rev. Cold Reg. Sci. Technol.* 65, 88–96.
- Seifert, H., Westerhellweg, A., Kröning, J., 2003. Risk analysis of ice thrown from wind turbines. *BOREAS VI conference*, April 2003, Pyhä, Finland.
- Tammelin, B., Säntti, K., 1996. Estimation of Rime Accretion at High Altitudes — Preliminary Results. *BOREAS III/FMI, Saariselkä, Finland* 194–210.
- Tammelin, B., Säntti, K., 1998. Icing in Europe. *BOREAS IV/FMI, Hetta, Finland* 125–132.
- Vestas, 2006. Wind turbine product descriptions V80-1.8 MW. *Vestas Americas Inc.* vestas.com.
- Walton, W.H., Woolcock, A., 1960. The suppression of airborne dust by water spray. *Int. J. Air Pollut.* 3, 129–153.

GENERAL CONCLUSION

The present thesis brings together the important results and the acquired scientific knowledge during my doctorate studies that yielded three original research articles.

There is the need for an anticipated knowledge of icing occurrences in a given area prior implanting ice-sensitive structures. The uncertainty with respect to the occurrence of icing events motivated many experimental and modeling studies including the current thesis to investigate the historical and real-time characteristics of icing events.

The assessment of the icing severity in this thesis has two stages that accommodate the topographic irregularity and the calculation cost involved. The first stage focuses on using coarse resolution data spanning a long time period, in order to preliminary identify large regions with high icing severity. The second stage focuses on identifying icing events over complex terrains with mountainous and localized irregular topography, which involves numerical simulations with the use of the mesoscale weather model «GEM-LAM» (Global Environmental Multiscale - Limited Area Model), equipped with the sophisticated microphysics scheme Milbrandt and Yau.

Based on cylinder model for ice accretion, the climatology of atmospheric icing is introduced using an unprecedented long representation of icing events spanning a 32-year dataset of meteorological variables from North American Regional Reanalysis. The proposed icing severity index that assesses the severity of icing events consists of three weighting factors that reflect the severity classes, the duration of icing events and the liquid water content. Subsequently, an updated version of in-cloud icing climatology at high

resolution is achieved using double-nested GEM-LAM simulations driven by NARR. Due to the time consuming numerical calculations, a hybrid approach is used to combine numerical model icing calculations during significant icing days from GEM-LAM and icing calculations during non-significant icing days obtained from NARR. In addition, through an investigation of high resolution output, the interrelationships between meteorological icing key parameters were revealed and 3D near-surface icing climatology is identified. The end product of the studies in chapter 1 and chapter 2 represents the climatology of icing severity over a 15-year period at high resolution. The proof-of-concept of the hybrid methodology presented for the Quebec region could be easily adapted to other cold areas (or cold season months) of the world to obtain their icing severity index maps.

With regards to the impact of atmospheric icing on wind turbines, this Thesis investigated the effect of the phase and the size of cloud droplets on collection efficiency and freezing fraction. In addition typical values of the duration of icing events were introduced for different liquid water contents. The results obtained can help the setup of a sensor that triggers the ice-protection system upon detection of the critical freezing fraction.

The methodology used in this dissertation permitted the achievement of the objectives that were initially planned with regard to the climatology of in-cloud icing events using reanalysis and an optimal high resolution hybrid approach of mesoscale modeling. In addition to the advantage of high resolution mesoscale modeling compared to the coarse resolution of NARR, GEM-LAM showed the ability of identifying the vertical profile of the characteristics of icing events at different altitudes above ground level.

Finally, with the use of the power loss factor indicated in chapter three and key meteorological parameters for icing events originated from NARR, GEM-LAM or other sources will enable the evaluation of wind turbine power degradation.

Rapport-Gratuit.com